Characterization of the Dynamic Formation of Nano-Tendril Surface Morphology on Tungsten while Exposed to Helium Plasma

by

Kevin Benjamin Woller

B.S. Engineering Physics (2009)
Tarleton State University

Submitted to the Department of Nuclear Science and Engineering
in partial fulfillment of the requirements for the degree of

Doctor of Science in Nuclear Science and Engineering

at the

MASSACHUSETTS INSTITUTE OF TECHNOLOGY

June 2017

Author……
Department of Nuclear Science and Engineering
March 17, 2017

Certified by……
Dennis G. Whyte
Professor, Nuclear Science and Engineering
Head, Nuclear Science and Engineering
Director, Plasma Science and Fusion Center
Thesis Supervisor

Certified by……
Ronald G. Ballinger
Professor, Nuclear Science and Engineering, and Materials Science and Engineering
Thesis Reader

Accepted by……...
Ju Li
Professor, Nuclear Science and Engineering
Chair, Department Committee on Graduate Students

Characterization of the Dynamic Formation of Nano-Tendril Surface Morphology on Tungsten while Exposed to Helium Plasma

by

Kevin Benjamin Woller

Submitted to the Department of Nuclear Science and Engineering
on March 7, 2017, in partial fulfillment of the
requirements for the degree of
Doctor of Science

Abstract

Tungsten undergoes surface morphology changes on the nanometer scale when subjected to low energy helium ion bombardment. This is due in part to the ion bombardment causing tungsten atoms to move on the surface, but also because of helium implantation and bubble development in the near surface at a depth < 30 nm. At high enough surface temperatures, $T/T_M \gtrsim 0.2$, where T_M is the melting temperature, nanoscale tendrils form on the surface and grow longer with additional bombardment by helium, but will decompose at the same temperature without helium bombardment. A tungsten surface that develops a densely packed layer of nano-tendrils over macroscopic areas greater than the grain size is referred to as tungsten fuzz, and is under intense study in fusion energy research, both for better understanding of how tungsten fuzz forms and of how tungsten fuzz affects the performance of plasma-facing components. The necessity of helium irradiation of the surface to induce nano-tendril growth motivates investigation into the dynamic process of helium implantation and accumulation in the surface. In this thesis, *in situ* elastic recoil detection is developed and used to measure the dynamic concentration of helium within a tungsten surface during the active growth of tungsten fuzz.

During the development of *in situ* elastic recoil detection analysis, a variant of tungsten nano-tendril growth was discovered featuring drastically isolated bundles of nano-tendrils that grow at a higher rate than tungsten fuzz. The variation in nano-tendril morphology is correlated with incident helium ion energy modulation. The dependence on ion energy modulation and isolated nature of the nano-tendril bundles reveals clearly that nano-tendril growth is sensitive to surface kinetic effects. In this thesis, the structure and parameter space of the newly discovered nano-tendril bundle growth is analyzed with a suite of electron-based surface science techniques.

Thesis Supervisor: Dennis G. Whyte
Professor, Nuclear Science and Engineering
Head, Nuclear Science and Engineering
Director, Plasma Science and Fusion Center

Thesis Reader: Ronald G. Ballinger
Professor, Nuclear Science and Engineering, and Materials Science and Engineering

Acknowledgements

What great fortune I have for the family I am blessed with. Thank You, for my loving wife, Crystal, and her commitment to me and unwavering support during my graduate studies. If it wasn't for her, I may not have even applied to MIT. Thank You, for my happy babies, Liam, Cora, Myla, and baby #4. They make life fun (and loud). Thank You, always, for my parents and siblings; their fundamental contribution to my development is the core to who I am.

I have immeasurable gratitude for my thesis supervisor, Prof. Dennis Whyte, who graciously led me with a long leash with which I had the freedom to explore the direction ahead of us. I am also grateful to Dr. Graham Wright for his immediate advice and guidance in the lab. The DIONISOS plasma chamber was the result of Dr. Wright's thesis work; without it, the research in this thesis would not be possible. My research relied on a diverse scientific background which was overseen by my thesis committee. Prof. Ron Ballinger and Prof. Bruce Lipschultz contributed to this oversight over the years, and I greatly respect their contribution to my thesis committee.

The work of Dr. Harold Barnard and Pete Stahle to re-commission the Tandetron accelerator at MIT was necessary for this research. I've learned many things from the different iterations of the accelerator team. I appreciate the opportunity to develop the skills needed to carry out this research which each.

I am in gratitude to the chief electrical engineer of the Alcator project, Dave Terry, along with the other electrical and RF engineering staff of the Plasma Science and Fusion Center for their assistance in bringing the Tandetron accelerator power supply fully operational, enabling my research to move forward. The technicians of the PSFC machine shop were also very kind with their time and encouragement to teach me the various tools as I needed to use them.

Contents

List of Figures

List of Tables

1 Introduction

Tungsten (W) is a refractory metal with the highest melting point of all metals (T_M = 3695 K). Due to its superior thermal properties, W is used in many high-temperature applications, from incandescent light-bulb filaments to first wall armor for thermonuclear fusion energy devices. In addition to its high melting point, W is attractive for plasma-facing components (PFC) in fusion energy devices because of its low sputtering yield and favorable behavior under neutron irradiation [1–3]. For fusion energy research, the study of the effect of the main fusion product, helium (He), on the W armor has led to the observation that He ion bombardment leads to nano-tendril growth on metals [4,5]. Here, a nano-tendril is defined as a protrusion of metal with a typical width of approximately 10 to 50 nm and an aspect ratio of length to width greater than one. Tungsten "fuzz" is a quasi-uniform arrangement of nano-tendrils such that the entire original surface is covered by tendrils and the macroscopic surface becomes optically black (or non-reflective). Tungsten fuzz has been under intense investigation since it was first reported on over a decade ago by Takamura *et al.* [4]. Research has focused on an assessment of the impact the surface morphology has on the viability of W as the plasma-facing material of choice in fusion devices both in terms of immediate effects and long-term stability. Tungsten fuzz has potentially deleterious effects on the use of W in fusion energy devices because He, which is the fusion ash product, is omnipresent in the boundary plasma of fusion devices. The nano-tendrils of W fuzz generally change the response of the W surface to the plasma [2]. The nano-tendrils could be a source of dust and shortened component lifetime due to enhanced material removal. Evidence of the growth of nano-tendrils in the high-power density tokamak experiment Alcator C-MOD further motivates the study of nano-tendril growth [5].

The spontaneous development of topologically complex surface structures under seemingly benign low-energy He plasma bombardment is of general scientific interest in material and plasma-material interaction science for other applications outside of fusion energy. The modified surface layer dramatically changes the material properties of the surface, such as the emissivity and thermal diffusivity [6]. The highly porous surface becomes optically black, making the surface an almost ideal blackbody absorber that might be advantageous for thermo-photovoltaic collectors or as a beam dump in laser applications. Also, the highly porous structure has been used in photo-catalytic experiments to assess the performance of porous tungsten oxide for solar water-splitting [7].

Researchers are driven to understand why and how fuzz forms in general, as fuzz growth has been observed on various metals [8–10], but it is not fundamentally understood well enough for prediction outside of a simplified parameter space of surface temperature and ion energy. Nano-tendril formation occurs on W in the temperature range 900-2000 K ($0.24 \lesssim T/T_M \lesssim$

0.54). At surface temperature $T_s \lesssim 900$ K, or below the brittle-to-ductile transition temperature, nanometer-sized pits and micrometer-sized blisters form as He bubbles develop below the surface. For $T_s \gtrsim 2000$ K, or above the recrystallization temperature, the surface features have larger characteristic sizes and He no longer forms stable clusters with defects in the material. With surface temperatures between the brittle-to-ductile transition and recyrstallization temperatures of W, nano-tendrils grow from the surface under He ion irradiation. In fusion power plants, elevated ambient temperatures likely exceed 800 K in order to access high global thermal efficiency for electricity production. Therefore, W surfaces will almost certainly operate in the fuzz-growth temperature range because they are used to conduct surface heat flux to cooling channels (e.g. a heat flux of 1 MW/m^2 leads to a 10 K/mm gradient in the W) while simultaneously the designer must avoid broaching recrystallization temperatures.

In the appropriate temperature range, the incident He ion energy has to be above a threshold value for W fuzz to form. To penetrate the W surface, He ions have to have high enough energy to overcome the surface energy barrier. The surface energy barrier for W is approximately 5 eV [11]. Pores and bubbles are observed to form when W is exposed to He ions just above 5 eV, but nano-tendrils are not observed to form until the incident He ion energy is greater than 12-37 eV, depending on the other exposure conditions [4,12–14]. The energy threshold for W fuzz growth can be compared to other known phenomena that are linked to the incident ion energy. The minimum energy at which W atoms are liberated from the surface by the incident He ions, a process called sputtering, is in the range of 100-110 eV [15]. Release of W atoms by bombardment of ions with energy below the threshold for sputtering has been reported to occur at 1470 K when the incident ions are deuterium, [16]. At low temperature, for energies below the threshold for sputtering, W atoms can still be liberated from the surface layer, but remain loosely bound on top of that surface layer. These loosely bound atoms on the surface are called adatoms (adsorbed atoms). These adatoms are believed to be the source of sub-threshold energy sputtering at elevated temperatures [17]. The energy necessary for the formation of adatoms is intuitively less than the threshold energy for sputtering because the atoms do not need to completely escape the surface energy potential, and is hypothesized to be a factor of 0.3 to 0.6 of the threshold energy for sputtering [18,19], or 33 to 66 eV. The threshold energy to observe nano-tendril growth roughly coincides with the threshold energy for adatom generation. For incident ion energies above the threshold for sputtering, W fuzz still forms, but the growth rate of the W fuzz layer thickness is lower [20–22]. For fusion energy research, incident ion energies above the threshold for sputtering are typically avoided to maximize PFC lifetimes.

Even when the surface temperature is above 900 K and the incident ion energy is above ~37 eV, a certain amount of He ion exposure, called an incubation fluence or incubation time [22–24], is needed before the nano-tendril morphology starts to manifest itself on the surface. Pinholes and corrugations form on the surface during the incubation period, prior to nano-tendril growth. Figure 1-1 shows the change in surface morphology of a polished W sample bombarded with He ions through the incubation period. The sample was exposed to He plasma in the plasma exposure chamber of the Dynamics of ION Implantation and Sputtering Of Surfaces (DIONISOS) at the Massachusetts Institute of Technology [25]. After the

incubation period, the thickness of the W fuzz layer increases with the square root of the plasma exposure time, or, for a constant ion flux density, the square root of the He fluence to the surface. This growth dependence is consistent with Fickian diffusion [26] and has been the basis for testing physical models developed to describe W fuzz growth. Figure 1-2 shows the cross-sectional view of W fuzz growth at different exposure times on samples exposed in the linear plasma device PISCES of the University of California in San Diego [27].

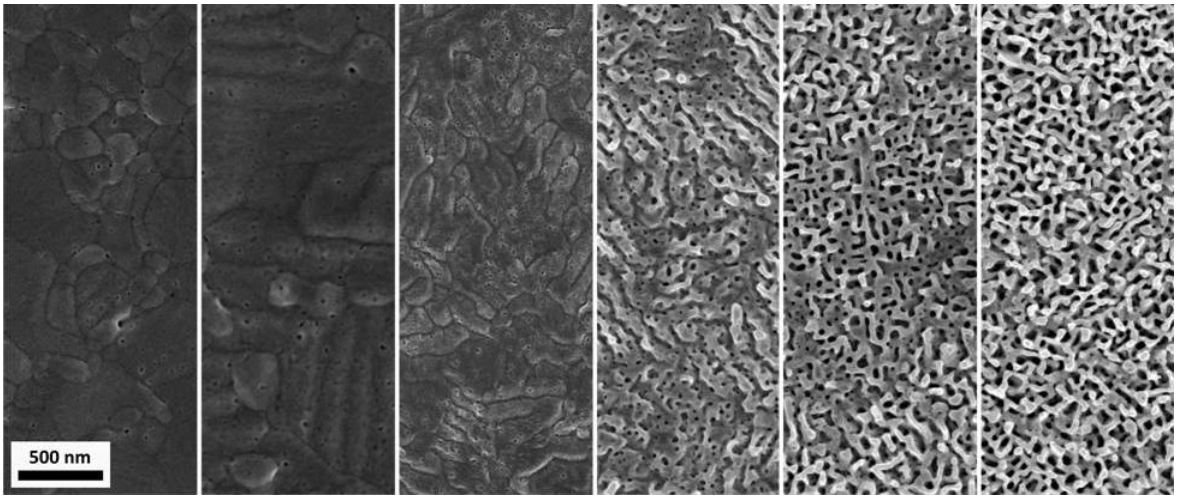

Figure 1-1 | View of tungsten normal to the surface during the incubation period of helium plasma exposure.
Set of images showing the change in surface morphology with increasing He fluence from left to right. The set of images is composed of scanning electron micrographs at different areas on a single sample of W with a He flux density increasing from the left image to the right image. The surface temperature was 1103 K and the He ion flux density for the right-most image was 4 x 10^{21} $m^{-2}{\cdot}s^{-1}$. The exposure time was 870 s. The flux density/fluence on the left-most image is estimated to be 2 orders of magnitude lower than for the right-most image.

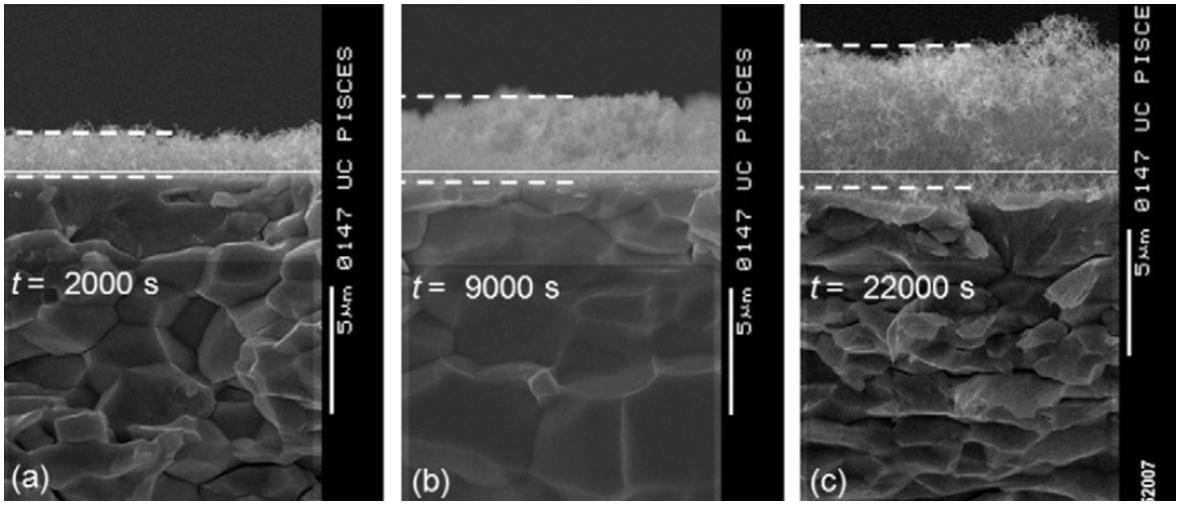

Figure 1-2 | Cross-sectional view of tungsten fuzz growth.
Samples of W exposed to pure He plasma for exposure times of (a) 2.0 x 10^3 s, (b) 9.0 x 10^3 s, and (c) 2.2 x 10^4 s with a He flux density of 5 x 10^{22} $m^{-2}{\cdot}s^{-1}$ and the W surface at 1120 K. The dashed lines depict the boundaries of the W fuzz layer. The solid line, drawn across the set of images, is a representation of where the original polished surface would have been located. Reprinted with permission from [28].

The necessity of He interaction and the presence of voids within the nano-tendrils differentiate these nanostructures from other nano-whiskers or nanowires. The solubility of He in metals is very low [29]. Helium is usually only held in metals at trapping sites like defects in the lattice. The defects can be grain boundaries or even single vacancies [30–32]. Once a He atom is trapped, another He atom diffusing through the metal lattice can bind to the trapped He atom, stabilizing the trap. Bubbles can form from the trapped He by plastic deformation of the lattice. All the physical models of W fuzz growth identify near-surface He bubbles as a first step for the fuzz growth. However, the models use different mechanisms for nano-tendril growth after the incubation period. In some models, the He bubbles are suggested to reach pressures that exceed the yield strength of W, which would induce dislocation loop-punching in the bulk or cause bubbles near the surface to rupture, leaving thin pieces of the bubble shell behind as nucleation sites for the process to continue [33–36]. In another model, He bubbles with pressures marginally below that needed to overcome the yield strength of W could lower the viscosity of the W on the surface and allow viscoelastic flow along the surface to deformities and nano-tendril tips [37]. Finally, another model holds that the He bubbles are a source of tensile stress in the surface, which lowers the chemical potential over the surface of bubbles, causing a net flux of adatoms generated by the He ion bombardment towards the bubble apexes, where the adatoms may become trapped and form the tendrils [19,38]. The principal goal of this thesis is to provide experimental evidence that tests theoretical models of W nano-tendril nucleation and growth.

With wide speculation that the interaction of implanted He, namely the coalescing of He into bubbles in the near surface region, drives fuzz growth [39], the first focus of this thesis is to quantify the He concentration in W fuzz at various stages of development. The ion beam analysis technique termed elastic recoil detection (ERD) can be used to measure the He concentration depth profile in heavy substrates directly, with good accuracy and depth resolution. In **Chapter 2** of this thesis, the first non-destructive measurements of He concentration in a variety of fuzzy and non-fuzzy W surfaces using ERD are presented for the investigation of how the He concentration changes with He fluence and surface temperature. First, ERD is explained, and then the results from the initial measurement of the He concentration depth profiles are presented. The first measurements were performed on samples from the PISCES device that is located at the University of California at San Diego (UCSD) and the PILOT-PSI device that is operated by the Dutch Institute For Fundamental Energy Research (DIFFER). The He concentration depth profile measured using ERD in post-exposure samples exhibited a very uniform average concentration throughout the measureable depth of the W fuzz layer [40], which was approximately 1 μm of W fuzz. The average He concentration, however, is lower by an order of magnitude than what might be expected as necessary for pressure-driven loop-punching to deform the W. These measurements establish, for the first time, the minimum He concentration that might be present during plasma exposure.

In order to test the discrepancy between theory and post-exposure measurements, the focus of this thesis shifts to measure the He concentration depth profile dynamically, during the modification of the surface into W fuzz. **Chapter 3** provides details of the technical aspects of developing *in situ* ERD analysis within the target chamber of the Dynamics of ION

Implantation and Sputtering Of Surfaces (DIONISOS) experiment. The results show the He concentration measured during plasma exposure, even during W fuzz growth, is much less than what is thought necessary for bubble bursting models. The He pressure is too low to represent He bubbles that overcome the strength of the W and the surface does not have a high enough He concentration to effectively lower the surface energy of W. One of the main achievements of this thesis is the development of *in situ* ERD and subsequent measurement on samples grown under various conditions within the growth parameter space for W fuzz.

Given the extreme environment that results in W fuzz growth, there are other possible mechanisms that could lead to nano-tendril growth. During the development of *in situ* ERD, W fuzz was found to be suppressed for an unknown reason in the helicon mode plasma discharge in DIONISOS. Single nano-tendrils and nano-tendril bundles (NTBs), shown in Fig. 1-3 and 1-4, respectively, were discovered with the absence of uniform (optically black) W fuzz growth. The lower-than-expected He concentration coupled with the discovery of single nano-tendrils and NTBs led to the investigation into the possibility that W fuzz growth is correlated to the presence of the sheath electric field, which has been present in all instances of widespread W fuzz growth. In **Chapter 4**, a method of shielding the surface from the sheath electric field is presented. The results of growing W fuzz with the surface shielded from direct exposure to the plasma show that the sheath electric field is not necessary for W fuzz growth, nor does it control fuzz growth.

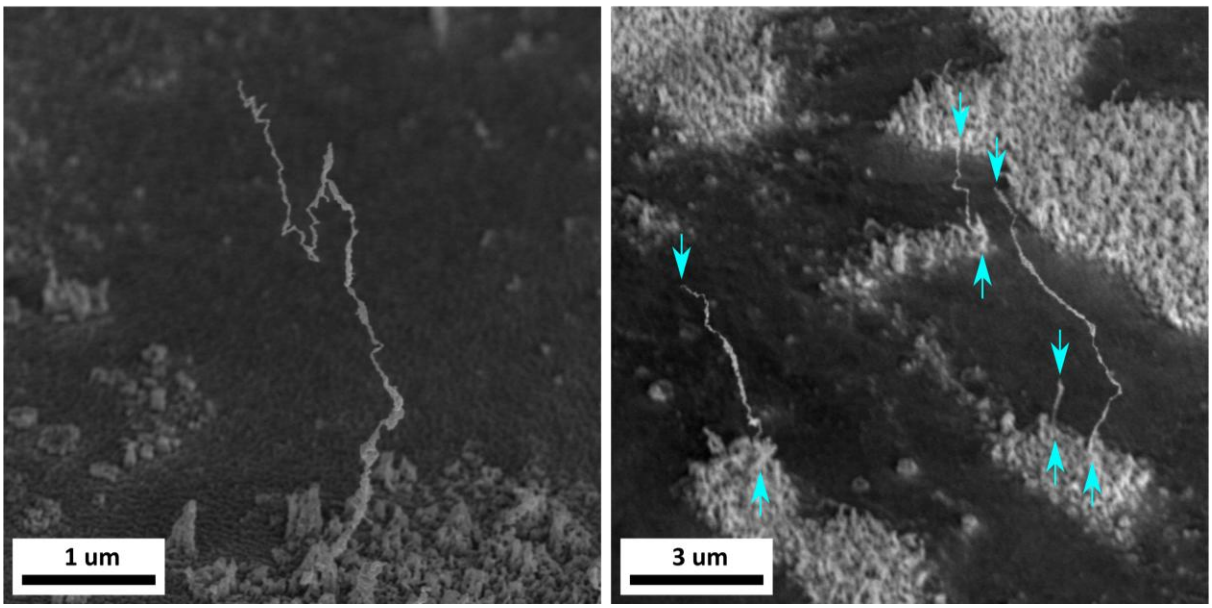

Figure 1-3 | Single tungsten nano-tendrils that formed during helium plasma irradiation using the helicon plasma source of DIONISOS at MIT.
The images are acquired from a scanning electron microscope looking at the samples after the exposure has ceased and the samples have cooled. The normal direction of the tungsten samples are tilted 52° from the electron beam axis. The blue arrows indicate the base and tip of the nano-tendril.

The apparatus developed to test the plasma sheath electric field hypothesis is a grid-collector retarding field. The grid-collector was used as a retarding field energy analyzer to measure the energy distribution of the plasma ions, which led to the discovery that the ion energy incident on the samples exposed to the helicon mode of the plasma source of DIONISOS is not constant. In **Chapter 5**, the characterization of the ion energy distribution function under various discharge conditions in DIONISOS is presented.

For surface diffusion models, the growth environment with high flux densities and high surface temperatures make it difficult to directly observe adatoms migrating to form complex nanostructures. Indirect evidence that surface diffusion might be responsible for surface morphology changes under He plasma irradiation is in the corrugation patterns that are observed before nano-tendril growth during the incubation period. Corrugations developed under ion bombardment are a common feature in epitaxial growth and sputter patterning, which have strong theoretical roots in surface diffusion [41]. The discovery of the ion energy modulation under certain conditions in DIOINISOS and its correlation to the growth of single nano-tendrils and NTBs, structures that strongly support theories based on surface diffusion, led to the deeper investigation of ion energy modulation effects on W nano-tendril growth.

All of the models mentioned above are based on the common observation that W fuzz grows as a surface-averaged layer. The new and diverse set of nanostructure types observed in this research breaks this paradigm. In **Chapter 6**, the different structures, namely, corrugations, isolated nano-tendrils, NTBs, and fuzz (Fig. 1-4) are analyzed to investigate the nature of the surface morphology changes under He ion bombardment. Since such isolated structures cannot develop from volumetric or surface-averaged growth mechanisms, growth can either progress by surface migration mechanisms or vapor redeposition of W removed from the surface. The former mechanism already has proponents in current modeling of W fuzz growth, and the latter should be negligible since the ionization mean-free-path under the typical plasma irradiation conditions in DIONISOS is several orders of magnitude larger than the Debye length, so any W that is liberated from the surface should be considered lost from the plasma-surface interaction zone. Nano-tendril bundle and solitary nano-tendril growth offer clues, if not direct proof, that adatom surface diffusion is the principal mechanism controlling nano-tendril growth, and W fuzz growth, in general. Taken all together, these experimental observations strongly support the suggestion that the combination of He ion bombardment and bubble agglomeration that results in adatom diffusion and surface roughening are the basis for the development of nano-tendrils.

In DIONISOS, sample mass loss was found to accompany NTB growth. In **Chapter 7**, the exposure parameters are varied and the changes to NTB/fuzz growth are presented, including mass loss measurements, in order to assess the implication of W nano-tendril mitigation strategies in future fusion energy devices, given that the lack of fuzz could be a sign of erosion and the unstable NTB structure could be a source of mass loss. Tokamaks use RF wave injection for current drive and heating. The RF waves in the plasma affect the plasma–surface interactions either through sheath rectification [42] or, if the conditions are such that the ions can respond on the RF time scale, by time-modulating the ion energy [43,44]. Thus,

like W fuzz, the circumstances that lead to the growth of NTBs, ion energy modulation, may be present in future fusion energy devices, as well. As the dawn of fusion energy approaches, detailed study of plasma-surface interactions continue to be needed. **Chapter 8** concludes this thesis with a summary of the main results from the research carried out for this thesis along with considerations for future work that might continue on from this work.

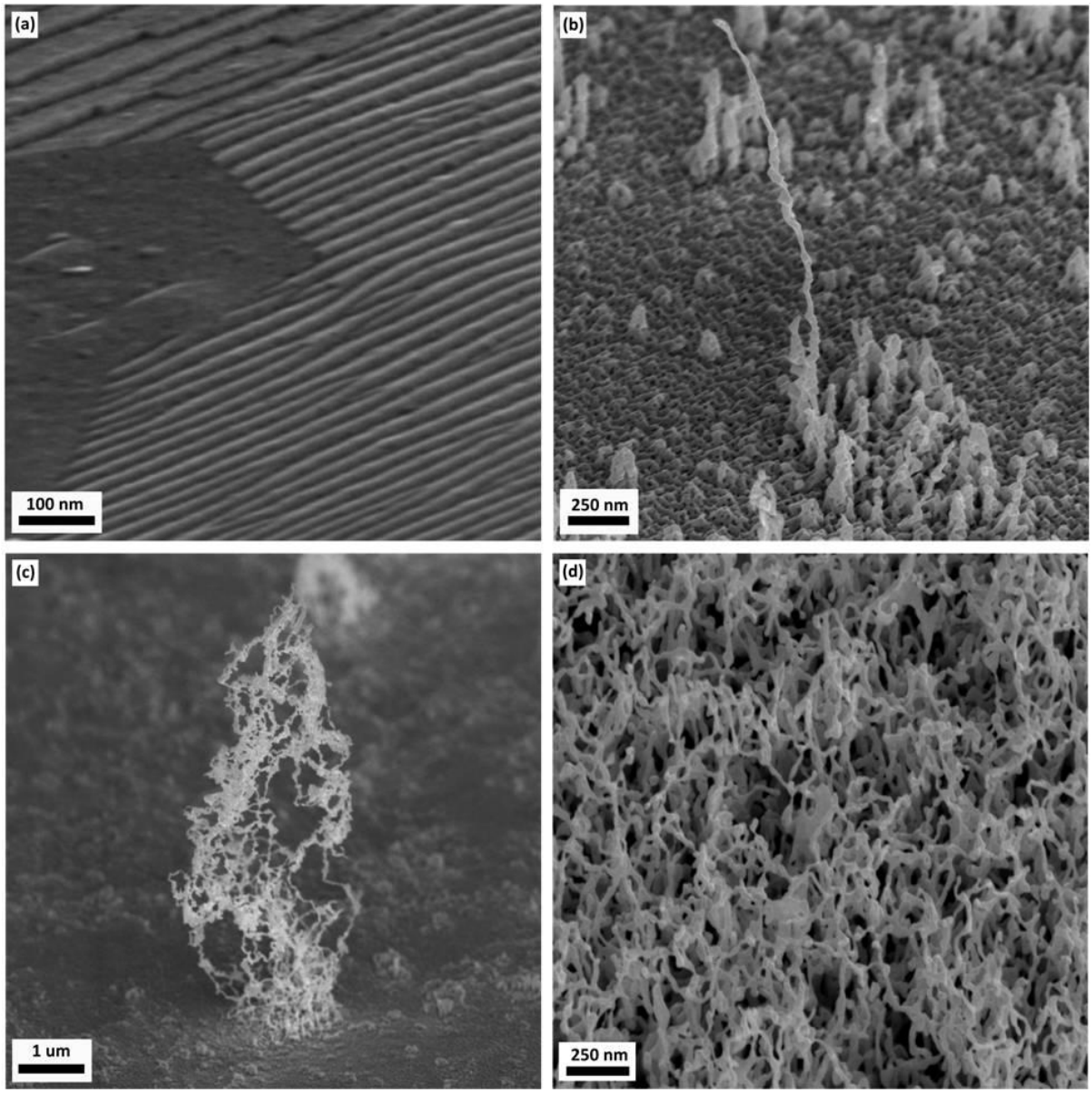

Figure 1-4 | Variety of nanostructures induced by helium bombardment on polycrystalline tungsten. Scanning electron micrographs of (a) corrugations due to ion bombardment, (b) a single nano-tendril, (c) a single nano-tendril bundle, and (d) fuzz. The viewing angle for each micrograph is 52° from the direction normal to the surface of the W sample.

2 Measuring the concentration of helium in tungsten fuzz using Elastic Recoil Detection

To investigate the role helium (He) might play in the growth of tungsten (W) nano-tendrils and fuzz, He concentration depth profiles in W fuzz were measured using Elastic Recoil Detection (ERD). Prior to the availability of the DIONISOS plasma chamber at MIT, fuzzy and non-fuzzy W samples produced in the PISCES and Pilot-PSI linear plasma devices were analyzed. The analysis of these samples provided initial observations of the He concentration in W fuzz, but also demonstrated that the *in situ* ERD measurements were needed for robust conclusions about the role of He in the growth of W fuzz. This chapter provides the details of implementing ERD commonly found in ion beam analysis (IBA) labs, providing a basis to compare to the implementation of *in situ* ERD in the DIONISOS plasma exposure chamber, which is detailed in Chapter 3. Also, the samples produced by these other devices provide higher temperatures and flux densities than are achievable with the DIONISOS experiment, thus expanding what is known about the correlation of the He concentration with these parameters.

The results from using ERD to measure He concentrations in W fuzz was presented at the 52nd Annual Meeting of the APS Division of Plasma Physics and the 20th International Conference on Plasma Surface Interactions in Controlled Fusion Devices and published in the Journal of Nuclear Materials [40,45].

2.1 Elastic Recoil Detection

Figure 2-1 shows a schematic of an ERD setup as implemented in an IBA lab for compositional analysis of materials. For ERD, a high-energy (E_0 ~ 1 MeV/amu), heavy ion ($M_1 \geq 4$) beam arrives on a target at a grazing angle. Elements which are lighter than the beam ions are scattered in the forward direction, or recoiled. These forward-scattered particles are dubbed "recoils." Some of the recoils escape the sample with finite kinetic energy. The energy of the recoils is set by the incident beam energy, the mass of the recoil, the scattering angle, and the depth from which the recoil was born. The mass of the recoil is known through the kinematics of the collision. The recoil kinematic factor in the laboratory frame [46],

$$K_r = \frac{4M_1M_2}{(M_1+M_2)^2}\cos^2\theta_r, \tag{2.1}$$

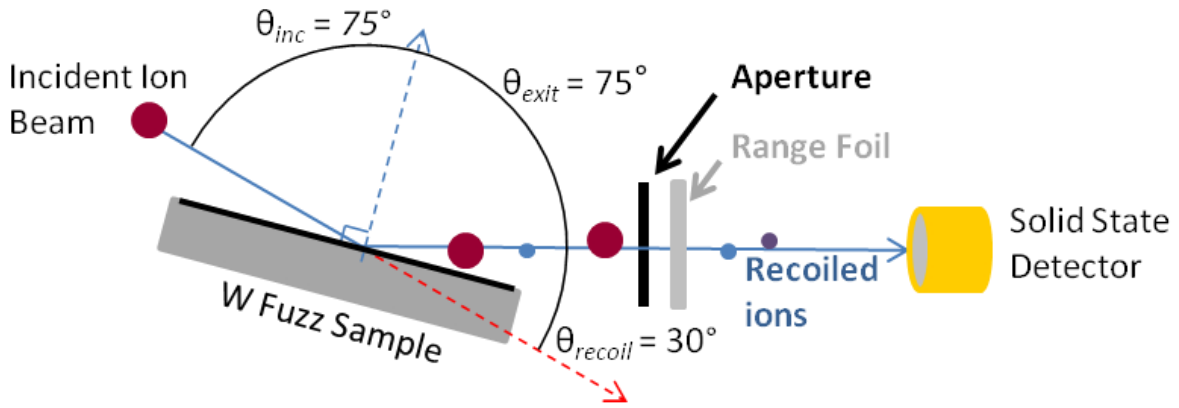

Figure 2-1 | Schematic of a typical Elastic Recoil Detection setup using a range foil.
A high energy, large mass ion beam is set incident on a target, W fuzz in this case, and the energies of the lighter elements recoiled from the surface are recorded using a solid state particle detector.

is dependent on M_1 and M_2, the mass of the incident ion and recoil, respectively, and the recoil angle, θ_r. The mass of the ion beam is known, as is the recoil angle, which is determined by the angle between the incident ion beam path and the line from the interaction site on the sample to the detector. The kinematic factor is the ratio between the energy of the incident ion to the energy of the recoil *at the point of collision when the recoil is born*. Therefore, the highest energy of any recoil at some recoil angle is generated at the very surface of the sample,

$$E_{2,max} = K_r E_0. \tag{2.2}$$

As the incident ion and recoil travel through the sample, they lose energy according to the electronic and nuclear stopping power of the material, $S = -dE/dx$. For thin layers, S is approximately constant through the layer. Since both the incident ion and the recoil lose energy if the collision takes place deeper in the material than the surface, the energy of the recoil that originates from inside the sample holds information about at what depth the collision took place.

The ion used for this thesis was oxygen-16 (^{16}O) with energies in the range of 4-7 MeV. The ERD cross section for ^{16}O ions of this energy colliding with He and H follows the Rutherford differential cross section for recoils of Coulomb collisions [46,47],

$$\sigma_R^{ERD}[mb/sr] = 2.0731 \times 10^7 \frac{[Z_1 Z_2 (M_1 + M_2)]^2}{(2M_2 E_1[keV])^2 \cos^3 \theta_r}. \tag{2.3}$$

Here, E_1 is the energy of the incident ion at the point of collision, and Z_1 and Z_2 are the atomic numbers of the incident ion and the recoil, respectively. The number of recoils detected at a specific energy, which corresponds to the depth in the sample, is used to

determine the areal density of the of the recoil species, $(N\tau)_2$, in atoms per unit area, at that depth,

$$(N\tau)_2 = \frac{Y_2 \cos\theta_i}{Q_1 \Omega_\mathrm{d} \sigma_R^{ERD}}, \tag{2.4}$$

where Y_2 is the integrated counts in the spectral peak of the recoils from the detector, θ_i is the angle of the incident ion beam with respect to the normal direction of the sample, Q_1 is the number of incident ions, and Ω_d is the solid angle of the detector.

A typical unit for areal density in IBA is 10^{15} cm^{-2}, because this number corresponds closely to the thickness of 1 monolayer (ML) of atoms of a solid. For W, 1 ML is a_0=0.316 nm thick and the number density of solid W is N_W=6.4 x 10^{28} m^{-3}. The areal density of 1 ML of W is then equal to $N_W a_0$= (0.316 x 10^{-9} m)·(6.4 x 10^{28} m^{-3}) = 2.0 x 10^{15} cm^{-2}. If the volumetric density is known, then the areal density from ERD measurements can be converted to concentration depth profiles. The porosity of W fuzz is typically 90%, so the volumetric density of W in the W fuzz layer is 10% that of solid W. Later, for *in situ* ERD analysis, the surface morphology and porosity of the surface being measured changes with time from one measurement to the next, so the depth profile is no longer easily converted to a linear dimension. Regardless, the interpretation of ERD for He concentration is independent of the bulk material density making ERD an excellent tool for this study.

Since the detector for ERD is placed in the forward direction from the ion beam, there is also the probability that the incident ions scatter into the solid angle of the detector. The scattering cross section is much larger than the recoil cross section and, the scattered ions can have higher energy. If there is no means to differentiate between the scattered ions and the recoils, then the measurement would not be useful. The strategy used in ERD and this thesis takes advantage of the stopping power dependence on the atomic number of the particle. The heavier scattered ions lose energy more efficiently than the lighter recoils passing through the same material when they are at the same kinetic energy. So, a thin foil, called a stopping or a range foil, is placed in front of the detector in order to stop the scattered ions from reaching the detector. The foil thickness is chosen such that the maximum-energy scattered ions are stopped completely thus guaranteeing that the measured ions at the detector are only recoils. The recoils also lose some energy through the foil, but this energy loss is calculable and acceptably small with proper thickness choice of the range foil. With this setup, meaningful probing depths of approximately 8 x 10^{17} cm^{-2} are achieved, which corresponds to 125 nm in solid W or 1.25 μm in W fuzz with 90% porosity.

2.2 Practical ERD analysis

2.2.1 Ion beam species and energy

IBA techniques are desirable for compositional analysis because of sensitivity to impurities in materials, as long as the various parameters of the measurement (i.e. geometry, ion beam species and energy, etc.) are well characterized. The Cambridge Laboratory for Accelerator Studies of Surfaces (CLASS) [48] uses a 1.7 MV Tandetron tandem ion accelerator for IBA for general purposes and for *in situ* IBA in the plasma exposure chamber of DIONISOS. A schematic of CLASS is shown in fig. 2-2. The accelerator is equipped with a RF charge exchange negative ion source for ions of gaseous origin manufactured by the National Electrostatics Corporation (NEC) and a cesium sputter source that produces ion beams from almost any element in solid form built by General IONex. Ion sources do not produce only one ion species at a time. There are multiple isotopes ionized at once, with varying charge states. For the tandem accelerator design, negative ions are produced in the ion sources and the negative ions are injected into the accelerator with an injector magnet. The predominant charge state for the ions for any species of beam produced from the ion sources is q = -1. The cross section for q = -2 charge state is at least 100 times lower than for the q = -1 charge state. All of the negative ions produced from the ion source have the same energy. The trajectory of a singly charged ion traversing the injector magnet follows a circular arc with a radius, R_{inj}, according to the Lorentz force,

$$R_{inj} = \frac{1}{B_{inj}}\sqrt{\frac{2M_1V_{ext}}{\mathrm{e}}}. \tag{2.5}$$

Here, B_{inj} is the magnetic field strength set by the injector magnet and V_{ext} is the extraction potential of the ion source. For specific R_{inj}, B_{inj}, and V_{ext}, and negative ion of mass M_1 is injected into the accelerator.

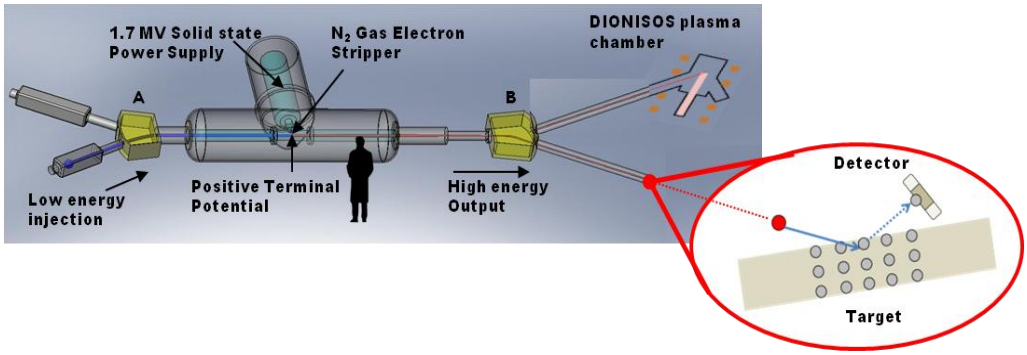

Figure 2-2 | Schematic of the CLASS accelerator facility.
The CLASS facility utilizes the 1.7 MV Tandetron tandem ion accelerator formerly of the Cambridge Accelerator for Materials Science (CAMS) at Harvard University. The major components are the low energy negative ion sources, the injector sector magnet (labeled A), the high voltage power supply for the terminal, the gas electron stripping canal, the high energy positive ion selection sector magnet (labeled B), and the two beam line end stations, the Helicon plasma chamber and the general IBA target chamber.

Once the beam species is chosen by appropriately setting the injector magnetic field, the negative ions are accelerated to the positive high voltage terminal, V_{term}. The Tandetron accelerator is designed with a solid state voltage multiplier that has voltage stability of +/- 5 kV at 1.7 MV. The vacuum component of the high voltage terminal that the beam travels through is a long tube into which is bled a small amount of nitrogen gas. The nitrogen pressure is of an adjustable level to strip (or ionize) the ~MeV beam ions of some of their electrons. The result of stripping the electrons from the partially accelerated negative ion beam is a plural beam of multiple positive charge states, according to the electron stripping cross section. The positive plural beam is accelerated from the positive high voltage terminal to ground potential at the high energy side of the tandem accelerator. The various beams now have different energies according to the distribution of charge states.

The charge state, and respective energy, of the beam is selected for IBA by sector magnet at the high energy side of the accelerator. For the selector magnet, as for the injector magnet,

$$R_{sel} = \frac{1}{B_{sel}} \sqrt{\frac{2M_1}{\mathrm{e}} \frac{[V_{ext} + (\mathrm{q_i} + 1)V_{term}]}{\mathrm{q_i^2}}}. \tag{2.6}$$

For specific R_{sel}, B_{sel}, V_{ext}, and V_{term}, a beam with ions of mass, M_1, and charge state, $\mathrm{q_i}$, are selected for IBA. The energy distribution in the final beam for IBA is Gaussian with a variance of ~5 keV. The injection and selection magnetic fields are calibrated with a Gauss meter and the radii are set by the geometry of the vacuum vessel. Collimating apertures are placed in the beam line to force the envelope of the beam to be within a diameter of 10 mm at the low energy side of the accelerator and 2 mm at the start of the beam lines for IBA, which are ~5.5 m apart. The beam line represents another 1.5 m for the beam to travel from the collimating aperture to the final aperture of 1 mm in the general IBA chamber. The final beam current at the IBA sample ranges from 5 nA to 50 nA on the sample. The current is kept low so that the heat flux from the beam does not perturb the measurement and for reasonable count rates on the detectors. For high temperature experiments in the plasma chamber, the ion beam contributes a small portion of the overall heat flux to the target, so high currents are used to improve time resolution

2.2.2 Detection energy calibration

Solid state detectors are used to measure the energy of the particles recoiled from a sample that is being bombarded by the ion beam. The detector is constructed as a diode that is triggered by particles that strike the active area of the surface. An energetic particle creates electron-hole pairs as it slows down in the detector. The number of electron-pairs is proportional to the energy and dependent on the mass of the slowing particle. A bias is kept on the detector so that the electrons and holes are swept to the opposite poles of the detector, generating a charge pulse. The charge pulse is amplified and shaped into a Gaussian voltage signal by a shaping amplifier. The gain of the amplifier is linear to the height of the charge pulse, so that the voltage pulse is still linearly proportional to the detected energy. The height of the voltage pulses is binned according to some voltage scale, usually 0 – 5 V or 10 V, in a

multichannel analyzer (MCA). The pulse height spectrum represents the histogram of particle energies that were collected at the detector.

There are two main sources for the energy spread in the detection hardware. The first is the energy resolution of the detector itself. The detectors are shipped with a certificate of performance conducted by the manufacturer. For the solid state detectors used in this thesis, the energy resolution is ~15 keV out of the box. The overall energy resolution declines through damage from ion bombardment and contamination from the environment. Heavier particles create more displacement damage, so detector lifetimes are degraded for heavy ion experiments. Also, the surface of the detector must be kept clean so that the full energy of the particle is deposited in the active area of the detector. During experiments, the energy resolution can also be degraded if the temperature of the detector increases. This is due to the leakage current of the detector with a bias applied to it. The leakage current doubles for every 5 °C increase in temperature of the detector. For IBA with low current ion beams, there is no danger of the detector heating up from scattered ions. However, for the *in situ* IBA measurements in close proximity to plasma and heated samples, the temperature of the detector must be accounted for. This will be discussed further in Chapter 3.

Since there are multiple steps in the signal processing from the particle depositing energy to binning the voltage pulse, the electronic components will contribute the other source for energy spread in the detection setup, which amounts to a finite voltage resolution. To measure the voltage resolution of the detection electronics, a train of sharp voltage tail pulses with a stable amplitude is passed through the electronics. The width of the peak in the MCA spectrum that results from the multiple voltage pulses being processed by the detection electronics is a measure of the voltage resolution of the detection setup. The voltage resolution through the detection hardware on the full voltage scale of the MCA is 0.001. After the voltage scale of the MCA is calibrated for ERD, this voltage resolution amounts to ~ 5 keV in energy spreading. Thus, the best resolution for the detection setup for ERD is approximately 20 keV.

The voltage scale of the detection system is calibrated using radioactive sources that emit alpha particles with precise energy. For ERD, the energy scales for the different recoil species have to be calibrated separately because the response of the detector varies slightly with particle mass. This can be accomplished by generating He and H ion beams from the accelerator and using backscattering geometries. For backscattering geometries, the high energy edges, described by the kinematic factor for scattering [46],

$$K_s = \left[\frac{(M_2^2 - M_1^2 \sin^2\theta_s)^{1/2} + M_1 \cos\theta_s}{M_1 + M_2}\right]^2, \tag{2.7}$$

where θ_s is the angle that the scattered ion makes with the incident ion beam path, can be used to calibrate the energy scale. The large angle backscattering kinematic factor is much less sensitive to the scattering angle than the recoil kinematic factor is to the recoil angle.

Calibrating the energy scale with RBS of a sample with a known composition and different beam energies is a common practice in IBA.

2.2.3 Range foil thickness and roughness

With the energy scale calibrated using RBS, the thickness and the roughness of the range foils to be used in ERD can be measured. Range foils come from a number of different manufacturers that produce thin foils with various techniques. The foils are shipped with a nominal thickness for a given batch, but the thickness can vary by as much as 10 % in one batch. The variation in thickness represents the roughness of the foil and affects the ultimate depth resolution of the ERD measurements. For this work, RBS with a He ion beam to characterize the foils was used.

The foils used in this thesis were aluminum (Al) thin foils from Goodfellow Corporation and diamond-like carbon (DLC) foils from Micromatter. The thickness of the aluminum foils was measured by placing the aluminum foil flat over a piece of graphite. Since the aluminum has a higher mass than the carbon, the complete RBS spectrum from the aluminum foil is not mixed with the carbon substrate spectrum. The DLC foil was placed over a through hole of the sample holder such that the backside of the DLC was open to vacuum. The RBS spectra from the Al and DLC foils are imported into SimNRA [47] where the thickness (or total stopping power) and roughness of the foils is matched through simulating the spectra.

2.2.4 ERD detector geometry and solid angle

IBA techniques are employed to measure the composition and the depth scale for thin films on materials. The main parameters of the ERD setup that affect the concentration depth profile measurements are shown in Eqns. (2.1)-(2.4). The orientation of the ion beam with the sample and the detector both affect the calculation of the areal density of the recoils. The ion beam and target were aligned using a laser that was already aligned with the ion beam. Thus, the incident angle on the target was nominally set to 75° from the normal direction.

With the thickness and roughness of the foils measured by RBS and the energy scale well calibrated, the recoil angle can be measured using the recoil spectrum. For known energy scale, recoil mass, range foil, and ion beam, the angle of the collected recoil can be precisely measured by measuring the high energy edge of the recoil spectrum. Also, for a sample with a known concentration of H, the solid angle of the detector aperture can be measured, if the beam dose to the sample is known. To perform this calibration of the geometry to the already measured or verified parameters of the detection set up, the ERD setup was tested on a sample of polyimide film, which has the chemical formula $C_{22}H_{10}N_2O_5$. The film has a uniform thickness distribution and a smooth surface. The spectrum of the H recoils from the polyimide film was collected. The beam current was monitored so that an accurate measure of the beam dose was known and could be correlated to the H yield in the spectrum. This provides the nominal solid angle of the detector aperture.

2.3 Surface Roughness and Porosity

Elastic Recoil Detection is typically performed on smooth samples with minimal variation in the surface topology due to the uncertainties that can arise when interpreting the spectrum of the recoils. Different roughness scenarios have been investigated by others for ERD [49,50] to measure the effects the surface roughness has on the concentration depth profiles. Large errors in interpretation arise when the thickness of the layer of interest is of comparable size to the surface roughness. It was shown by Behrisch *et al.* [50] that although the shape of the spectrum can be vastly changed by the roughness of the substrate, the total content derived by integrating all of the counts contained in the spectral peak of the recoils is still the same for smooth and rough surfaces.

The samples that W fuzz is grown on are first polished to a mirror finish before exposure to He plasma. The typical roughness from mechanical polishing is on the order of 50 nm. For most of the W fuzz layers measured here, the layer thickness is several hundred nanometers thick while the nano-tendrils and voids between them are only a few tens of nanometers. Tungsten fuzz develops a porous layer of ~10% W by volume with the rest being empty space between the nano-tendrils and He bubbles within the nano-tendrils. Tungsten fuzz morphology is essentially columnar, which has been investigated by Stoquert and Szörényi [51] for the evaluation of size and morphology characteristics surfaces through the energy spread in IBA energy spectra. Their results show that spherical and columnar inclusion morphologies affect the energy spread at the high and low energy edges of the recoil spectrum. Due to the broadening at the edges of the spectra, the values of He concentration of W fuzz samples presented in this chapter are averages evaluated away from the edge of the fuzzy surface. Although their method was not applied to evaluate the He bubble and nano-tendril sizes and distributions, their method appears to be applicable to W fuzz and may be a route for future *in situ* analysis of the dynamic formation of nano-tendrils.

In non-fuzzy samples with He bubbles and blisters in a thin layer in the surface, the surface develops pockets of He distributed laterally and to a shallow depth with a typical void fraction of 20% [52]. Pores of empty space similar in size to the depth of the bubbles are present in samples where the surface temperature is above the upper temperature threshold for W fuzz growth [14]. The randomly distributed pores and He bubbles serve to reduce the stopping power of the W, and thus affect any calculated depths of the measurements. The pores do not have an effect on calculated He content of the thin layer as long as the entire spectral peak is integrated as mentioned above.

In general the porous nature of the fuzz can have minor effects on the ERD spectrum, but it will not significantly alter the interpreted atomistic He concentration in the fuzz, which is the main pursuit here.

2.4 Tungsten fuzz samples from PISCES and Pilot-PSI

Tungsten fuzz samples from two separate linear plasma devices were analyzed. Samples grown in the PISCES device [27] were cut from a sheet of rolled PLANSEE 99.9999 weight % tungsten. These samples were polished to a mirror finish of average surface roughness

below 50 nm and then exposed to pure He plasma. PISCES produces a plasma column with uniform ion flux density typically around 5 x 10^{22} $m^{-2} \cdot s^{-1}$ and also keeps the sample at a uniform temperature. Seven samples from PISCES were analyzed with 4 of the samples having only He bubbles and blisters in the near surface (<50 nm) and no nano-tendril development.

Samples grown in the Pilot-PSI device [53] were annealed polycrystalline W disks polished to a mirror finish with an unknown surface roughness and exposed to pure He plasma. Pilot-PSI is a high-flux density ($\Gamma_{He} \sim 10^{23}$ m^{-2} s^{-1}) linear plasma generator that operates in an axial magnetic field of B = 0.4 – 1.6 T. The W fuzz samples from this device have variation in both the surface temperature and ion flux density that peaks at the center and decreases radially outwards. The surface temperature and ion flux density at different radial locations was inferred from the center value and the known profile shapes. Eight samples from Pilot-PSI were analyzed at various radial locations for a total of 38 measurements. Seven of the 38 areas sampled from Pilot-PSI were non-fuzzy areas.

These samples were analyzed with various ion beam energies and corresponding stopping foil thicknesses depending on the highest terminal potential that was available from the Tandetron Tandem ion accelerator in the MIT laboratory. Some specific measurement details were as follows. An oxygen-16 (^{16}O) ion beam was directed at an angle of 75 degrees normal to the surface of the samples. Due to the finite size of the ion beam and the large incident angle, the final beam spot on the samples was an oval with a 1 mm minor diameter and a major diameter of 4.5 mm. A 2 mm wide curved-slit aperture followed the nominal scattering angle of 30 degrees from the incident beam path. An aluminum (Al) stopping foil with a thickness large enough to stop the highest energy scattered ^{16}O ions from the sample was placed after the aperture. A Passivated Implanted Planar Silicon (PIPS) detector was positioned behind the stopping foil to measure the final energy of the recoiled He, H and D from the sample. The aperture and active area of the detector defined the detection solid angle of 2.418 msr. The resolution of the detection electronics was measured using a polonium-210 alpha emitter and has a value of 22 keV FWHM for 5.3 MeV alpha particles. The energy scale was calibrated using the alpha emitter and various stopping foil thicknesses in front of the detector with an uncertainty of 100 keV. Secondary electrons emitted during the measurement were suppressed by a grid surrounding the sample holder biased to -500 V with respect to the vacuum vessel ground. The number of incident ions, called the beam dose, was measured directly as the collected charge on the samples.

The simulation software SimNRA [47] was used to determine the He atomic concentration from measured ERD spectra. The process involves an initial prediction of the simplified W fuzz layer composition. The samples were also expected to have hydrogen (H) content from water vapor adsorbed on the surface of the samples due to exposure to atmosphere. The ratio of the kinematic factor, Eqn. (2.1), of He to H shows that the highest energy recoil of H has an energy 0.29 times less than that of He. Thus, He recoils will have more energy than H, but the He also slows down more through the range foil given the same energy. In this situation, since the range foil is just thick enough to stop the scattered ^{16}O from reaching the detector, the He recoils still reach the detector with a higher energy than H which is desirable to

unambiguously identify the He contributions to the spectra. For SimNRA, the simplified W fuzz surface layer is defined as a three element layer that is homogeneous with some atomic ratio of He and H to W. The rest of the sample is modeled as a pure layer of W. The concentration parameters are adjusted and iterated until the simulated spectrum matches the experimental one. SimNRA evaluates the physics of the elastic collision of the beam ions with a predicted layer model along with the broadening effects due to physical geometry and energy straggling during the slowing down of incident ions and recoils in the sample and the range foil.

2.5 Results and Discussion

Figure 2-3 shows the cross section of one fuzzy sample that portrays the sizes of roughness and tendrils. Also in Fig. 2-3 is a plot containing the ERD spectrum from a similar fuzzy sample with background counts removed. The He concentration was estimated from the experimental data assuming a Rutherford cross section for recoils and using stopping power data from SRIM 2010 [54]. The estimated composition of the W fuzz layer was used as input to SimNRA [47] and then SimNRA was used to fit the composition to the experimental data. The result of the fitted simulation is plotted as the solid line in Fig. 2-3. The data fit was performed without roughness taken into account. A depth of 1500 nm was calculated as the viewable depth of He in the W fuzz layer. This mechanical depth was calculated taking the density of the W within this W fuzz layer to be one tenth the density of bulk W [14].

Figure 2-4 shows an exhibition of one sample from PILOT-PSI subjected to peak 7.5×10^{26} m^{-2} with the surface temperature peaked at 1470 K. The sample had both fuzzy and non-fuzzy sections. Figure 2-4a shows the He concentration depth profiles measured at three different spots on the sample pictured in Fig. 2-4c. The depth is shown in customary Ion Beam Analysis units of areal density. On the figures left-hand side, the non-fuzz profile is plotted at the top, an area right on the edge of the W fuzz area is plotted in the middle, and the profile of the W fuzz area is plotted on the bottom. The He concentrations in the three areas are similar, reaching up to approximately 1 at. %, despite the surface temperature and He fluence varying significantly across the sample, which are plotted in Fig. 4-2b. From the figures it is clear that only the depth of the ~1% He "zone" is changing. Also, the bottom plot shows that the He concentration profile of W fuzz is roughly uniform through the measurable depth. It can be seen from this sample that the surface temperature and He fluence had no signficant effect on the He concentration. It is also notable that the distinctive W fuzz surface morphology occurs when the surface temperature is >1000 K.

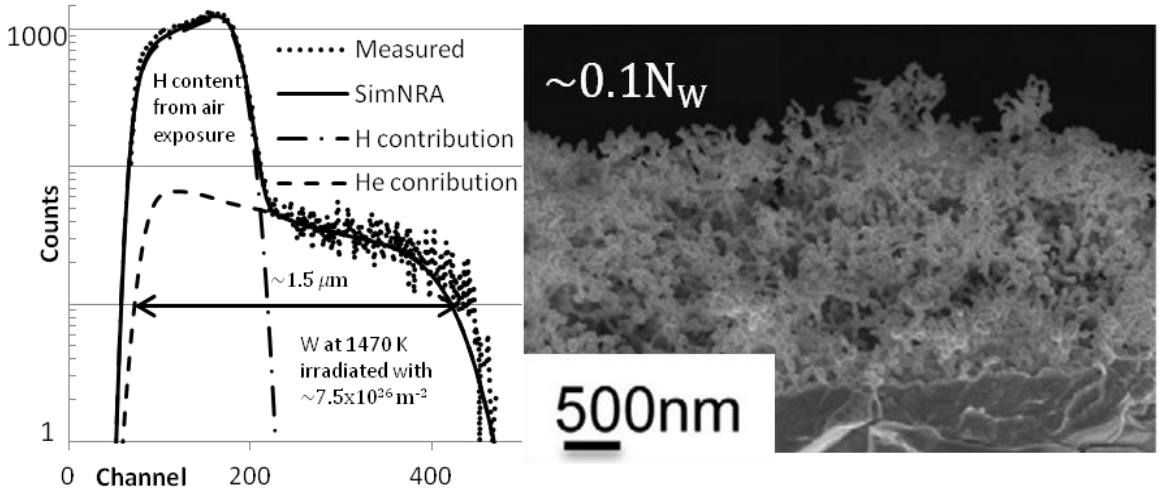

Figure 2-3 | Analysis of Elastic Recoil Detection Spectrum of tungsten fuzz from PISCES.
Plot of ERD spectrum (dot) and SimNRA simulation (solid) with the H (dash-dot) and He (dash) contributions to the simulated spectrum plotted separately. The experimental spectrum was measured from a W fuzz sample grown with a He fluence of 7.5 x 10^{26} m^{-2} and a central surface temperature of 1470 K. An SEM cross section of a similar sample of W fuzz is shown next to the plot to show the characteristic size of the tendrils and surface roughness of W fuzz grown in this regime. The viewable depth seen in this measurement is 1.5 μm. The density of the W fuzz layer is determined by mass loss measurements and was approximately 10% that of bulk W.

Figure 2-5 shows a summary of the ex situ He concentrations measured from 45 unique areas of fuzzy and non-fuzzy W. The surface temperature variation across all of these areas was 470 K < T_s < 2595 K while the He fluence varied in the range 3 x 10^{24} m^{-2} < Φ_{He} < 1.3 x 10^{27} m^{-2}. The summary shows that the He concentration remains within 1-2 at. % for non-fuzzy and 1-4 at. % for fuzzy W. There are differences in sample production such as plasma generation, sample heating, or even time from when the sample was produced to when it was analyzed that may account for the spread and clustering in the average He concentration. However, the range of 1-4 at. % is seen on single samples from PILOT-PSI but from different radial positions (growth conditions) of the samples. Notwithstanding this issue, the He concentrations are very high compared to the natural solubility of He in metals [29]. This amount of He in the fuzzy and non-fuzzy samples confirms the presence of high pressure He within the voids observed in the surface of He irradiated W and the nano-tendrils themselves observed by Kajita *et al.* [52]. However, the He concentration measured is inconsistent with current speculation of void creation mechanisms [55]. However, the actual He concentration during the production of W fuzz, i.e. during plasma bombardment, may be quite different from that measured here due to the archaeological nature of this study. As samples cool down, He diffusion out of the sample is greatest at higher temperatures. Thus, the rate of cooling after exposure to He plasma has ceased affects the final He concentration of the sample. Also, He will escape from the sample over time, and the pressure of the bubbles will influence the rate at which it escapes. All of these points motivate the next chapter in this thesis where the priority is measuring the He concentration during the plasma exposure.

2.6 Summary

To summarize this chapter, ERD was used to measure, non-destructively, the He concentration in W that has developed the characteristic nano-tendril morphology called W fuzz. In particular, the He concentrations of various samples from PILOT-PSI and PISCES were measured to be in the range of 1-4 at. % despite a surface temperature variation of ΔT_s = 2000 K among the samples and various He fluences across three orders of magnitude. This is a high value when compared to solubility of He in W, but does not represent the necessary concentration to support void creation and fuzz development due to deformation from over pressurized bubbles. The individual He concentration depth profiles of fully developed W fuzz show the He concentration to be uniform through the measurable depth. By monitoring He depth profiles, ERD is an indirect method to follow W fuzz development.

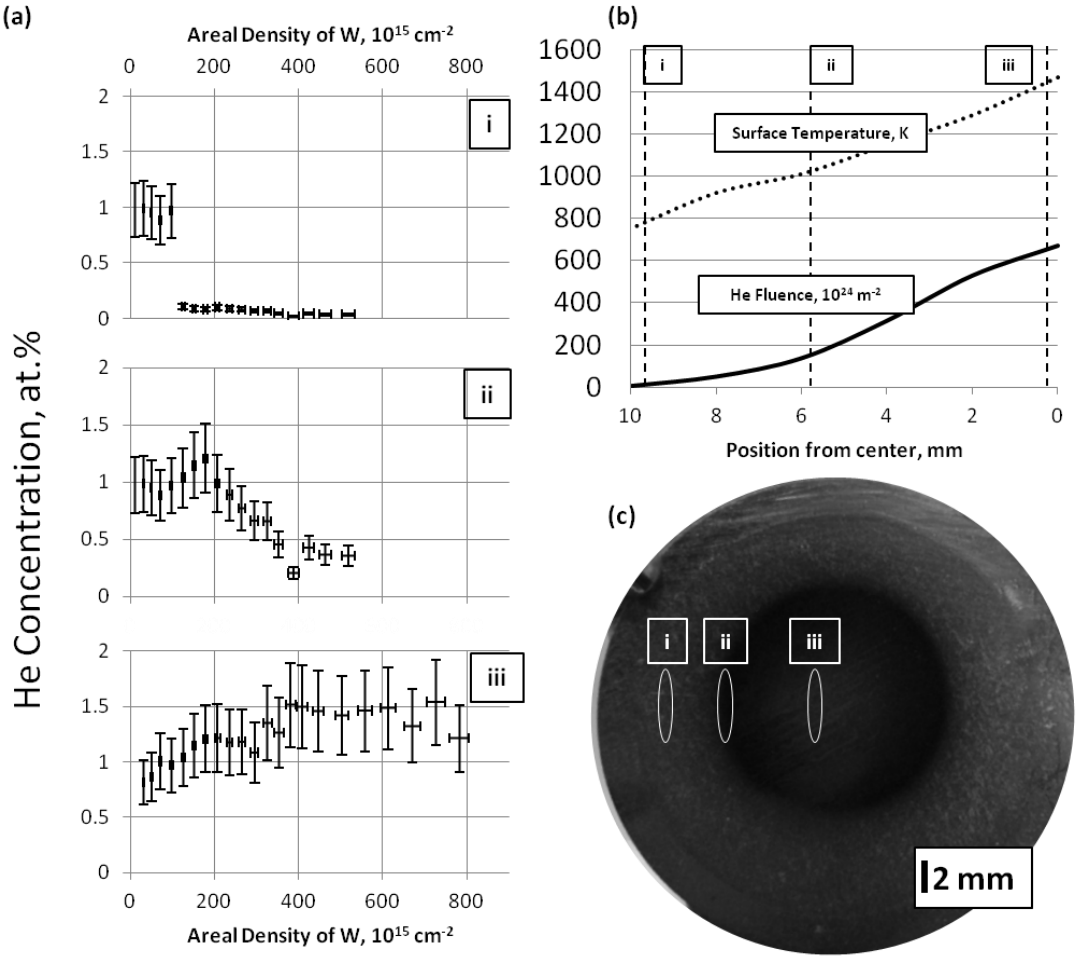

Figure 2-4 | Helium concentration depth profiles of sample from PILOT-PSI.
a) He concentration profile of W irradiated with He at different stages in W fuzz development i) He bubbles/blisters in the near surface, ii) W nano-tendrils beginning to form with W fuzz layer thickness increasing, and iii) full W fuzz layer grown, to a depth at the limit of detection of ERD . b) Surface temperature (dot) and He fluence (solid) profiles of the sample analyzed at different radial locations shown approximately by the dashed lines. c) Photograph of the sample with the white ovals portraying the ERD probing beam spot size and position for the three stages of W fuzz development.

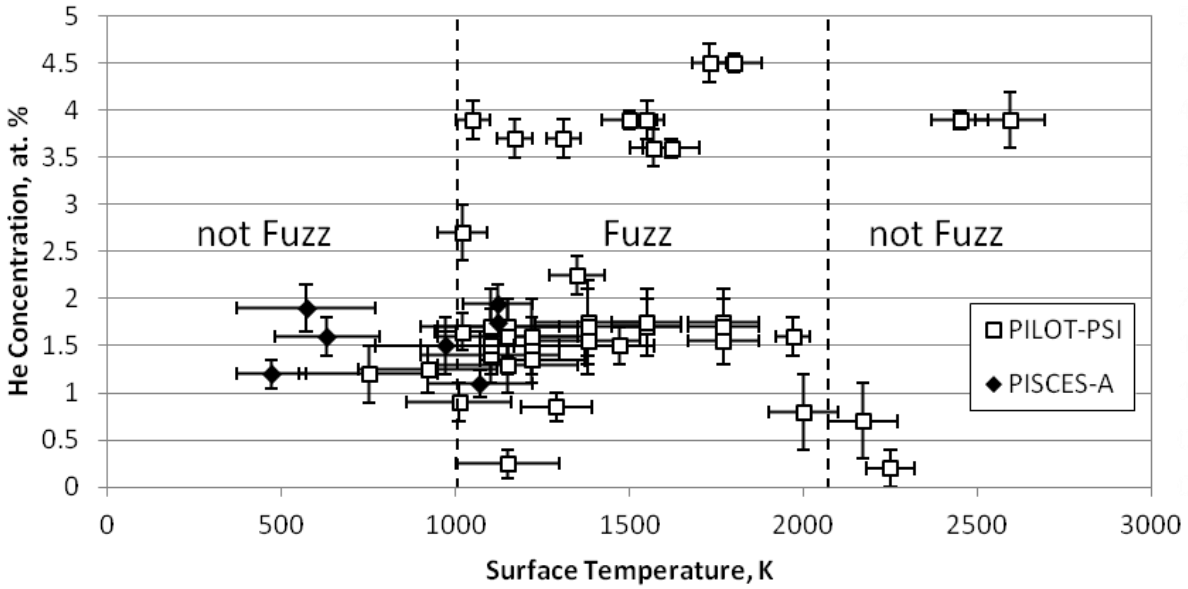

Figure 2-5 | Accumulative results of the helium concentration measured in various tungsten samples exposed to helium plasma in PISCES and PILOT-PSI.

Average (W fuzz) and peak (non-W fuzz) He concentrations of samples from both PILOT-PSI (open square) and PISCES (solid diamond) of various surface temperatures exposed to various He fluences. W fuzz formation occurs in the temperature range between the dashed lines. Below this range, He is found in bubbles just in the surface. Above this range, pores are also present with the He bubbles.

3 Measuring the dynamic helium concentration in evolving tungsten surfaces during plasma exposure

In this chapter, tungsten (W) surfaces are subjected to helium (He) plasma simulating a tokamak divertor environment in the Dynamics of ION Implantation and Sputtering Of Surfaces (DIONISOS) experiment. Surfaces are analyzed in real-time during irradiation with *in situ* elastic recoil detection (*in situ* ERD) to gain insights into dynamic He concentration depth profiles. The extreme environment of the divertor simulator requires specific considerations to be implemented to retain the integrity of Ion Beam Analysis (IBA) techniques for surface analysis. The development of the *in situ* elastic recoil detection measurement technique and the implications of the results regarding the modeling of W surface modification due to He plasma irradiation will be discussed.

The details of implementing ERD during He plasma irradiation to measure the dynamic He concentration was presented at the 26th IEEE International Symposium on Fusion Engineering and is published in the conference proceedings [56]. The presentation was awarded the IEEE Fusion Technology Best Student Paper award by the IEEE Nuclear and Plasma Sciences Society. The measurements made by *in situ* ERD of the dynamic He concentration in W fuzz during plasma irradiation was presented at the 21st International Conference on Plasma Surface Interactions in Controlled Fusion Devices and published in the peer-reviewed special issue from this conference in the Journal of Nuclear Materials [57].

3.1 Helicon plasma exposure chamber

The high ionization efficiency helicon plasma source of DIONISOS is powered using a type III Nagoya antenna with a 0.1 m half-wavelength powered by an APEX 13.56 MHz RF power supply that is rated for up to 3 kW output power. The plasma column is magnetically confined by four water-cooled copper coils that convert up to 300 A to a uniform axial maximum magnetic field of 0.1 T across the diameter of the target chamber. The gas species of choice is bled into the vacuum chamber through a 50 ccm mass flow controller and the background neutral gas pressure is monitored with a capacitance manometer. Background neutral pressures of up to 10 Pa (0.075 torr) are tolerable during accelerator operation due to differential pumping in the beamline leading up to the exposure chamber. The pressure upstream of the DIONISOS exposure chamber is maintained at 10^{-4} Pa (10^{-6} torr) to ensure adequate beam quality for IBA and to prevent the acceleration column from arcing.

Helicon plasma sources are well suited for the study of plasma material interactions relevant to tokamak divertor environments due to the ability to operate in a large range of particle flux density, typically 10^{20} - 10^{23} He·m^{-2}·s^{-1}. The moderate flux density is maintained at a relatively low electron temperature of a 3-6 eV which allows for control of the incident ion

energy on the sample. The ion energy to the surface of the target is controlled by a 300 V DC power supply, or a dual polarity 100 V power supply that is modulated by a Stanford DS340 15 kHz function generator.

Target temperature is controlled by thermocouple or IR camera feedback while the target is mounted on either a water-cooled or ceramic heater target holder. The ceramic heater can bring the target temperature up to 1400 K while the water-cooled target holder can keep the target near 300 K by removing the heat from the target due to the heat flux from plasma exposure. The feedback system allows for variable and highly controlled exposure temperatures which are only affected in a minor way by the plasma exposure itself.

3.2 Elastic Recoil Detection Analysis

Several details of the usual ERD set up that was detailed in Chapter 2 are shown again in this chapter to illustrate the specific challenges and resolutions taken to implement *in situ* ERD. Figure 3-1 shows the concept of ERD as implemented in an IBA laboratory for material composition characterization. For ERD, a high-energy, heavy ion beam is set incident on a target at a grazing angle. Elements that are lighter than the beam ions are forward scattered, some of which escape the target with some characteristic energy. A solid state charged particle detector is situated at a certain recoil angle from the interaction region to record the energy of the recoiled ions. The mass of the recoiled ion is known due to the kinematics of the collision and the depth from which the recoiled ion originates is estimated through the stopping power of the target. The cross section for the interaction is modeled very well by the Rutherford cross section, thus the yield of recoiled ions from the target is directly related to the average concentration of the recoiled species within the target.

High vacuum is usually maintained in the measurement chamber to minimize radical production in the residual gas that can degrade beam quality and contaminate the target. Electromagnetic and thermal noise in the target chamber is minimized to optimize the detector signal in both resolution and stability. Also, the geometry of the measurement is flexible to allow optimization of the beam-target interaction and to improve the measurement depth, resolution, and/or sensitivity.

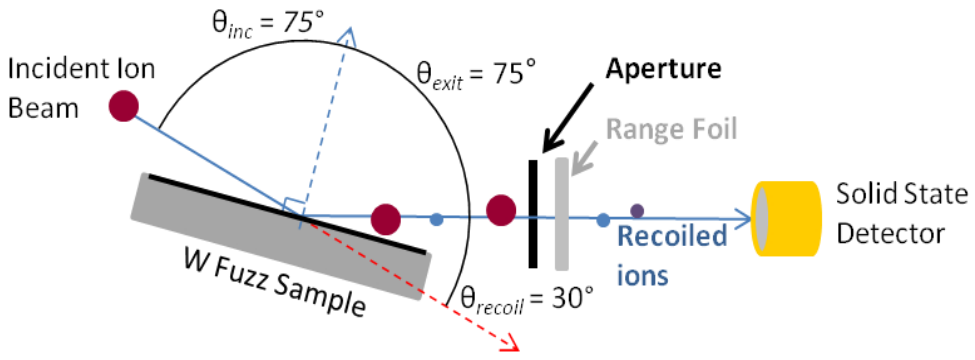

Figure 3-1 |Schematic of general elastic recoil detection experimental setup.
A high energy, large mass ion beam is set incident on a target, W fuzz in this case, and the energies of lighter elements recoiled from the surface are recorded using a solid state charged particle detector.

3.3 *In situ* Elastic Recoil Detection

3.3.1 *In situ* Elastic Recoil Detection Considerations

Many challenges that contradict the usual ERD environment are introduced by the DIONISOS plasma exposure chamber. These challenges are listed below and the resolution to each challenge is then described in the design of the detector holder and analysis of the *in situ* ERD data.

1. The RF plasma generates electromagnetic noise that permeates the exposure chamber. The ground of the detection circuit is sensitive to this noise and cannot tolerate ground loops linked through the plasma.

2. Thermal radiation from the target and heat flux from the plasma easily reach the detector location and thus must be prevented from raising the temperature of the detector to minimize leakage current through the detector. The leakage current through a solid state detector can double for every 0.5 °C increase in the detector temperature.

3. The magnetic field of DIONISOS bends both the incoming ion beam and outgoing recoiled ion trajectories. Also, the magnetic field limits the choice of materials for fabrication of components to be located in the exposure chamber.

4. The background neutral gas introduces some beam degradation near the interaction region and also generates an additional signal in the ERD spectra.

3.3.2 *In situ* Elastic Recoil Detector Holder Design

Figure 3-2 shows an exploded view of a solid model of the *in situ* ERD detector holder. The solid state charged particle detector is surrounded by G10 and PTFE insulation inside of the aluminum detector holder body. A range foil chamber between the detector and incoming recoiled ions is closed by an aluminum plate with a 1 mm slit aperture. The detector body is mounted to a water-cooled copper arm extending from a 40KF flange at the bottom of the exposure chamber. The detector holder assembly is fully rotatable about the vertical axis of the beam-plasma-surface intersection. The signal from the detector is taken out of the chamber by a triaxial cable with the inner conductor connected to the active area of the detector, the middle conductor connected to the grounding shell of the detector, and the outer conductor connected to the body of the detector holder. The cable is brought out of the exposure chamber by a BNC feedthrough isolated from the chamber wall with the outer conductor of the cable flared out and touching the wall.

The issue with electromagnetic interference (EMI) is mitigated by the triple conductor system for the detector circuit inside the exposure chamber. The detector is a biased diode that generates a charge pulse when impacted by a charged particle. A stable ground for the body of the detector is necessary to relate the charge pulse to the energy of the charged particle. The detector was isolated from the ground of the exposure chamber to prevent the

EMI from reaching the detection ground reference. The EMI is essentially shorted to the grounded exposure chamber wall before it is picked up by the detection circuit ground. An indicator of noise being picked up by the detector is when there is a signal being put out by the detector with no beam on the target. After implementing the triple conductor system, the detector signal dropped to zero during plasma exposures without the diagnostic beam on target.

The nominal leakage current was never more than doubled for the detector at room temperature, indicating the water-cooled detector holder arm and insulation are adequate for taking away the heat flux from the detector holder. During plasma exposures with the target heater up to 1400K, the energy resolution of the detection circuit increased from 20 to 40 eV, but this resolution is tolerable for our dynamic measurements. The degraded resolution affects the errors in the depth scale of the concentration profile, but has a negligible effect on the magnitude of the concentration.

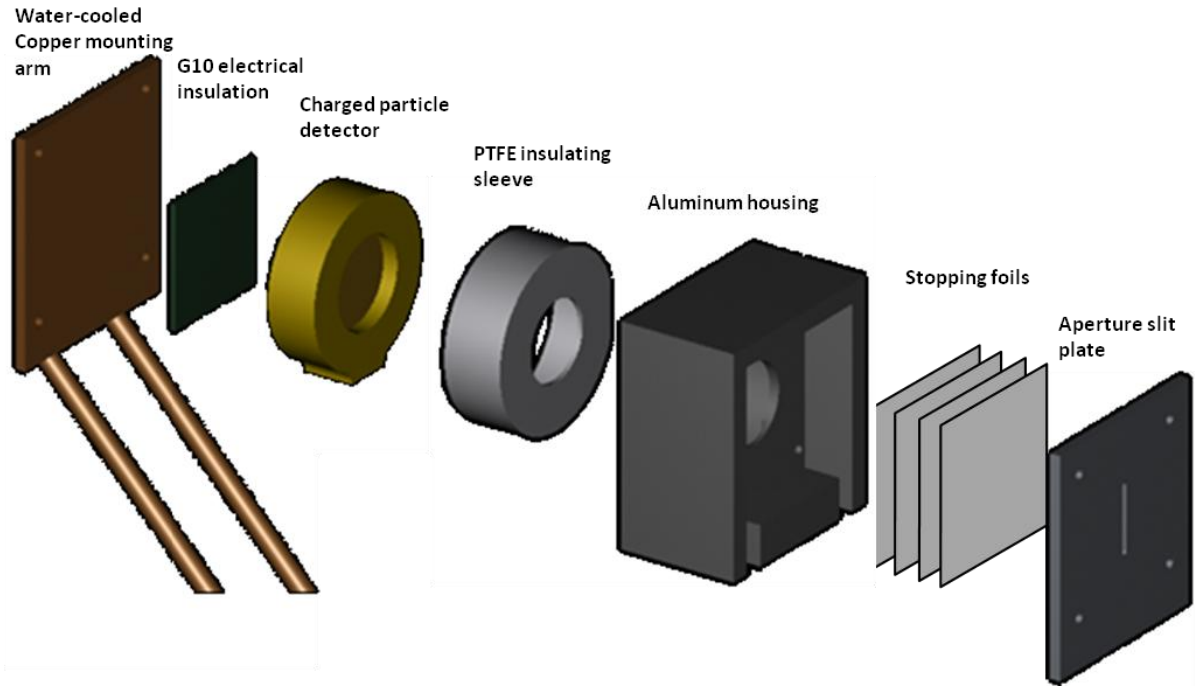

Figure 3-2 | Solid model of the *in situ* ERD detector holder.
Insulation was used to mitigate the effects of electromagnetic interference and heat flux on the solid state detector implemented in the DIONISOS exposure chamber.

3.3.3 Simultaneous ERD and RBS setup

Figure 3-3 shows a top-down schematic of the measurement set up in the plasma chamber of DIONISOS. Essentially, DIONISOS has the capabilities of ordinary Ion Beam Analysis (IBA) techniques with the added capability to irradiate the sample with plasma at the same time. This section provides the details of the measurement set up.

A 7 MeV oxygen-16 (^{16}O) ion beam was directed at an angle of 75 degrees normal to the surface of the samples. A 1 mm wide slit aperture in front of the detector defined the nominal scattering angle of 30 degrees from the incident beam path. The solid angle subtended by the detector aperture was measured by performing ERD on a polyimide target while monitoring the beam current periodically with a faraday cup as detailed in Chapter 2. The yield of the hydrogen (H) from the polyimide was simulated using SimNRA [47]. The solid angle determined in this manner was 3.22 +/- 0.1 x 10^{-3} sr. The thickness and roughness of Diamond-like Carbon (DLC) foils acquired from MICROMATTER^{TM} measured using Rutherford Backscattering Spectroscopy (RBS) were 5012 x 10^{15} cm^{-2} and 989 x 10^{15} cm^{-2}, respectively, using SimNRA to fit the foil spectrum. To overcome the bane of scattered ion beam leakage through stopper foil pinholes, a stack of 9 of these DLC foils was placed after the aperture to stop the O scattered off of W from reaching the detector. An Ortec ULTRA charged particle detector was positioned behind the stopping foil stack to measure the final energy of the recoiled He. The recoiled energy scale of the detection set up was calibrated using separate proton and alpha ion beams of various known energies scattered off of a quartz target at a scattering angle of 45 degrees. The overall depth resolution of the detection set up during irradiation was determined from this calibration and by an electronic pulser signal supplied to the detector preamplifier. The depth resolution was approximately 6 nm for He at the surface of W with a bulk density, or 40 x 10^{15} $W \cdot cm^{-2}$.

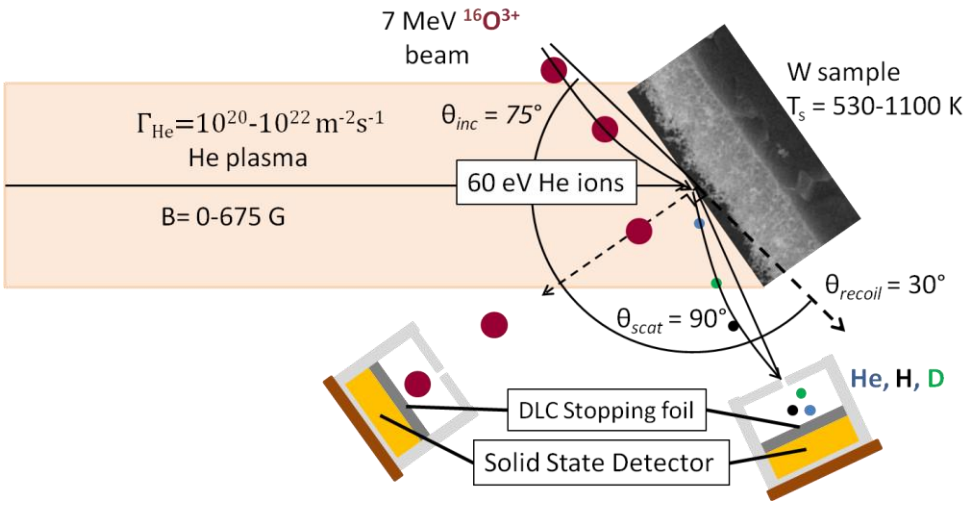

Figure 3-3 | Schematic looking down on the ion beam analysis set up within the DIONISOS irradiation chamber.
The probing ion beam species was ^{16}O accelerated to 7 MeV by a tandem electrostatic accelerator. The sample was tilted 30° with respect to the magnetic field and 75° from the probing beam. A detector at 30° from the incident probing beam path collected recoiled species from the surface of the irradiated samples. A detector at a scattering angle of 90° collected scattered O from the surface as a measure of the beam dose.

The probing beam current, at approximately 1 μA, could not be measured directly during irradiation due to the several hundred mA of ion saturation current supplied to the sample by the plasma. Thus, the beam dose was measured using the RBS yield of O particles scattered from W at an angle of 90 degrees from the incident beam path with a second detector acquiring simultaneously with the ERD detector. A single DLC foil carefully selected to minimize any pinholes was used in front of this detector to make it light-tight during plasma operation. The solid angle of the aperture in front of this detector was calibrated prior to irradiation experiments by measuring the beam current to a W sample that had secondary electrons suppressed. As before, the yield from this RBS signal was fit using SimNRA and the solid angle was measured to be 9.6 +/- 0.1 x 10^{-6} sr.

3.3.4 *In situ* Elastic Recoil Detection Data Analysis

The effects of the magnetic field on the trajectories of the ions involved and the background neutral gas filling the exposure chamber are unavoidable. The modification to the collision geometry, which is important in evaluating the depth scale, can be calculated from the radius of curvature of a charged particle in a uniform magnetic field. The trajectory is the arc of the incident beam that begins at the entrance into the magnetic field region and ends at the target location, which is known due to imaging of the beam on a quartz target prior to the measurement. The incident beam is monoenergetic so this method gives the true angle of incidence constrained by this geometry. The arc of the recoil ions is pinned at the beam-target intersection and the location of the detector aperture. Since there is a range of recoiled ion energies, there is a corresponding range of recoil angles picked up by the detector. However, the ions of interest are recoiled in the range of 1 to 3 MeV, so the overall variation ranges from 0.5 to 1.5 degrees. The He concentration depth profile evaluated from data taken with the magnetic field off and on shows a slight shift in the energy axis, corresponding to an effective recoil angle of 1 degree lower than the nominal recoil angle set by the detector aperture position. The difference in the Rutherford cross section due to this difference in recoil angle is less than 1%. In evaluating the ERD spectra data, the change in the recoil angle is included to duplicate this energy shift.

The background neutral gas was at a low enough pressure for the final short segment of the beam path near the exposure chamber that the majority of the beam profile remained intact, ensuring confidence in the location and area of the beam-target intersection. One additional component to the ERD spectra was generated due to the presence of the background neutral gas near the interaction region. Due to the incident beam forward recoiling He gas atoms into the detector, a signal proportional to the neutral He gas pressure in the chamber is incorporated in the ERD spectra. The background neutral gas signal shows up at higher recoil energy due to the lower recoil angle of the interaction (the He atoms are in front of the target). The signal caused by background neutral gas does not contribute to the signal corresponding to the He retained in the surface of the target, as can be seen in the background ERD spectrum of Fig. 3-4, taken while the magnetic field and gas feed are turned on, but without plasma excitation. This is because these contributions are of a small magnitude and reside at higher measured particle energies.

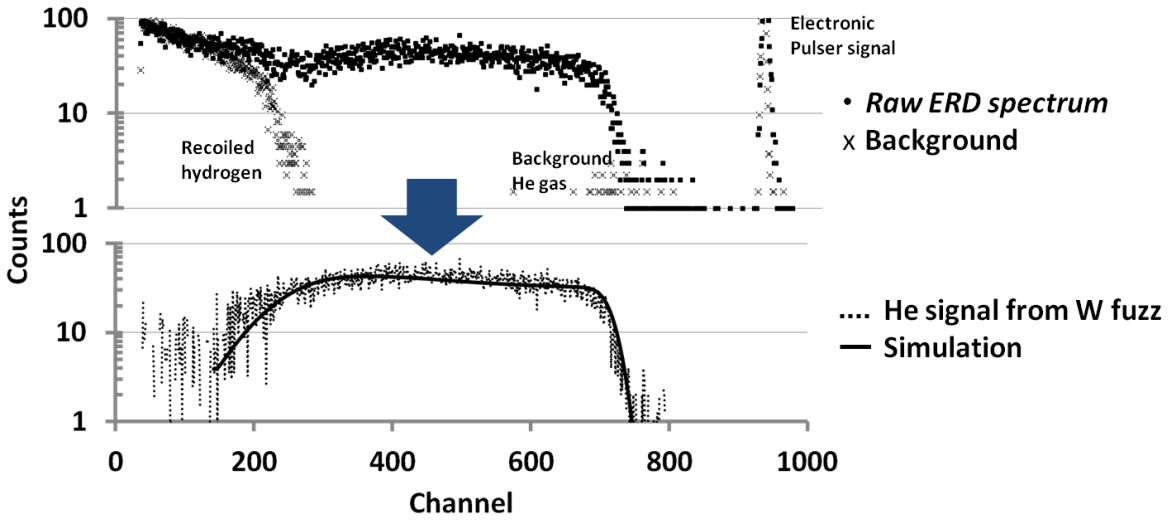

Figure 3-4 | Example of the analysis of an ERD spectrum.
First, a background spectrum is taken with the magnetic field and neutral gas feed on, but with no plasma excitation. Then, during the plasma exposure, ERD spectra are acquired that contain the persistent background signal. During data analysis, the background spectrum is subtracted from each dynamic ERD spectrum, leaving only the He signal to be simulated.

Due to the resiliency of the background signal taken before plasma exposure, a background spectrum can be subtracted from each *in situ* ERD spectrum, leaving the He spectrum for each acquisition time. The concentration depth profile of the true He spectrum is then fit with a simulation using SimNRA [47]. The He concentration depth profile was consistently found to uniform throughout the probing depth of the measurement, making it possible to simulate the He containing layer in the surface of the target as a single He/W layer. An example of this is shown in Fig. 3-4 where excellent fit quality is obtained with a single layer. The He concentration depth profile fit to simulation of each spectrum taken every 30 seconds during the plasma exposure are compiled to form the dynamic He concentration measurements. These constitute the first-ever in *situ* He surface concentrations in the presence of a high flux density plasma.

3.4 Results and Discussion

Table 3-1 summarizes the various growth conditions explored using the *in situ* ERD set up. Once the exposures were completed, the surface morphologies were imaged using the Helios NanoFab SEM of the MIT CMSE Shared Experimental Facility. Images of the final surface morphologies are shown in Fig. 3-5. Sample C was exposed to two plasma discharges with different discharge parameters in sequence during its exposure. At first, sample C was exposed to a flux density similar to sample E, but with a higher surface temperature of 1087 K in hopes of reaching a W fuzz growth regime. However, after some time, sample C was showing He saturation in a thin layer at the surface of the W. So, the He flux density was increased and then sample C showed signs of morphology changes through the active ERD spectra. This is illustrated in Fig. 3-6 through the evolution of the W areal density and He content, respectively, in the He-rich layer of sample C with the open and closed diamond symbols. W areal density is used as a measure of the "thickness" of the He-containing layer

because the porosity of this layer is changing during exposure. The W areal density is independent of the porosity. Thus, comparison of the evolution of the W areal density within the developing He layer between separate irradiation experiments may be done despite the surface morphological evolution. With the first flux density on sample C, the thickness approaches a value near 200 x 10^{15} W·cm^{-2}, similar to samples E, F, and G, which did not produce W fuzz. In bulk W, this corresponds to ~30 nm. This thickness for a He bubble containing layer in W is on the order of what others have seen for W that did not produce fuzz [58] near this surface temperature and incident ion energy. Each sample was exposed to He ions of the same energy and that might be why samples E, F, and G equilibrate to the same depth. After increasing the He flux density, the thickness increases at a rate similar to samples A, B, and D, which grew W fuzz.

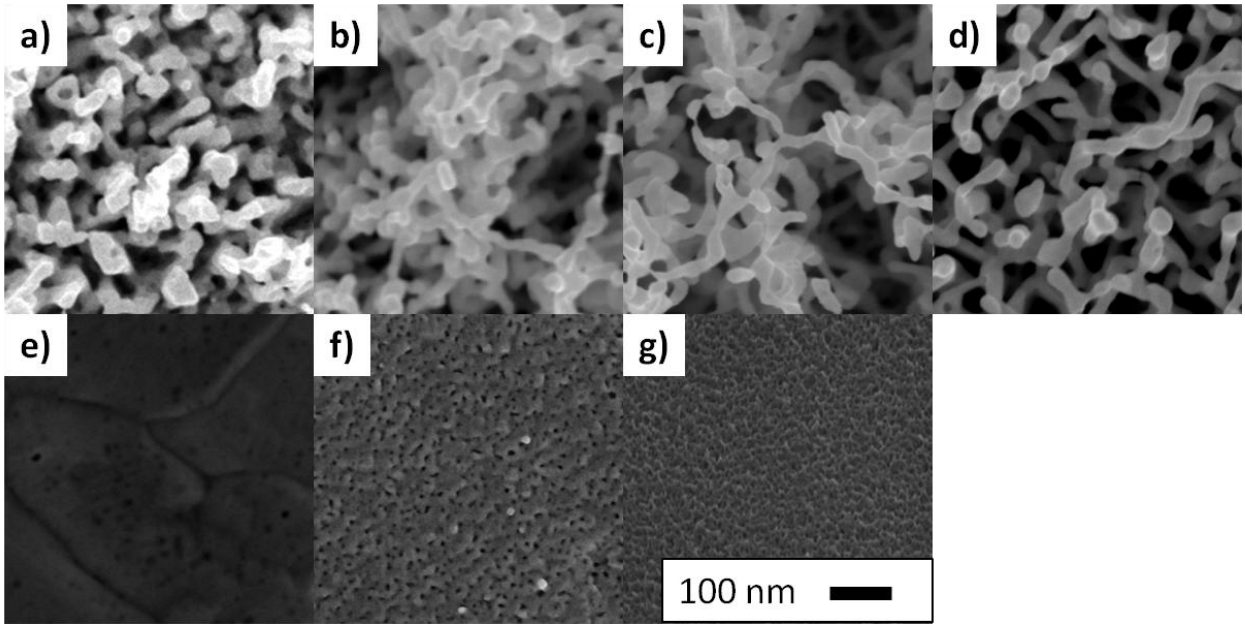

Figure 3-5 | SEM micrographs of the final surface morphologies grown under various surface temperatures, He flux densities, and He fluences in DIONISOS as indicated in Table 3-1.

Table 3-1| Sample growth conditions. E_{He}=60 eV.

Sample	T_s, *K*	Γ_{He}, 10^{20} $m^{-2}s^{-1}$	Φ_{He}, 10^{23} m^{-2}
a	1050	160	803
b	1043	100	629
High flux c	1107	100	415
d	1103	56	49
Low flux c	1087	2.5	--
e	1057	2.5	2.6
f	874	44	40
g	527	56	60

There is also a remarkable difference between the outcomes of samples D and E. These samples were exposed with the same temperature, but with flux densities that differ by a factor of 20. Also, the surface modifications are vastly different where in sample D fuzz developed readily and sample E was quite bare. This may indicate a flux density threshold that factors into the growth parameter space of W fuzz. However, there is also a factor of 10 difference between the final He fluence to the samples, with sample E supplied with less fluence than sample D. This difference in exposure may also account for the stark differences in surface morphology.

The top of Fig. 3-6 shows the He concentration evolution for each of the samples. The He concentration in these plots is the average He concentration that best fit each spectrum. During the first 400 s, the He concentration increases. This is during the incubation period before fuzz growth, so bulk number density of W would be used to interpret the layer depth during this period and the depth of the layer is < 30 nm. Then, the average He concentration in the near surface reaches a saturation level. For samples A, B, and D, at the same time as saturation, the surface reflectivity appeared to decrease, as observed by eye, suggesting W fuzz had begun to grow. For sample D, this corresponds to a He fluence of 2.24×10^{24} m^{-2}, which is comparable to what others have shown as the incubation fluence in this temperature range [22,59]. The porosity of the W fuzz layer would have to be taken into account at this point. Assuming that the porosity is constant in time, and since the W areal density is increasing, the W fuzz layer depth increasing with constant average He concentration through the W fuzz layer.

3.4.1 Dynamic Helium Concentration Evolution

The average He concentration evaluated from each ERD spectrum can be plotted against the square root of the exposure fluence to reveal the evolution of the He concentration in the W surface while W fuzz is developing. Figure 3-7 shows results of the dynamic He concentration for three samples exposed at the same surface temperature, but with slightly different He flux densities. In this case, both the time to saturation and saturation level increase with He flux density. At this He ion energy, the He ions have a range of only a few nm in the W, but He bubbles have been shown to develop to depths of 20 to 120 nm in [6] as a consequence of He and He bubble diffusion activated by elevated temperatures of the target. An incubation time or fluence threshold, as suggested in [23] and [60] may be thought of as a necessary amount of He accumulation to fully populate the surface of the W with He bubbles before the mechanism that gives rise to W fuzz takes over. This leads to the concept of a fluence threshold for W fuzz growth. In this experiment, a larger flux density of He to the W surface requires a longer time until the He concentration saturates. Thus, the fluence threshold increases with flux density for fluxes up to 10^{22} $He \cdot m^{-2} \cdot s^{-1}$. Other studies that have looked at the fuzz layer thickness and how it varies with fluence [13,14,23,60] have shown a fluence threshold of $\sim 10^{24}$ $He \cdot m^{-2}$, which is comparable to the fluences reached in this dynamic study. *In situ* ERD thus provides a direct observation of the advent of W fuzz growth by observing the dynamic He concentration evolution.

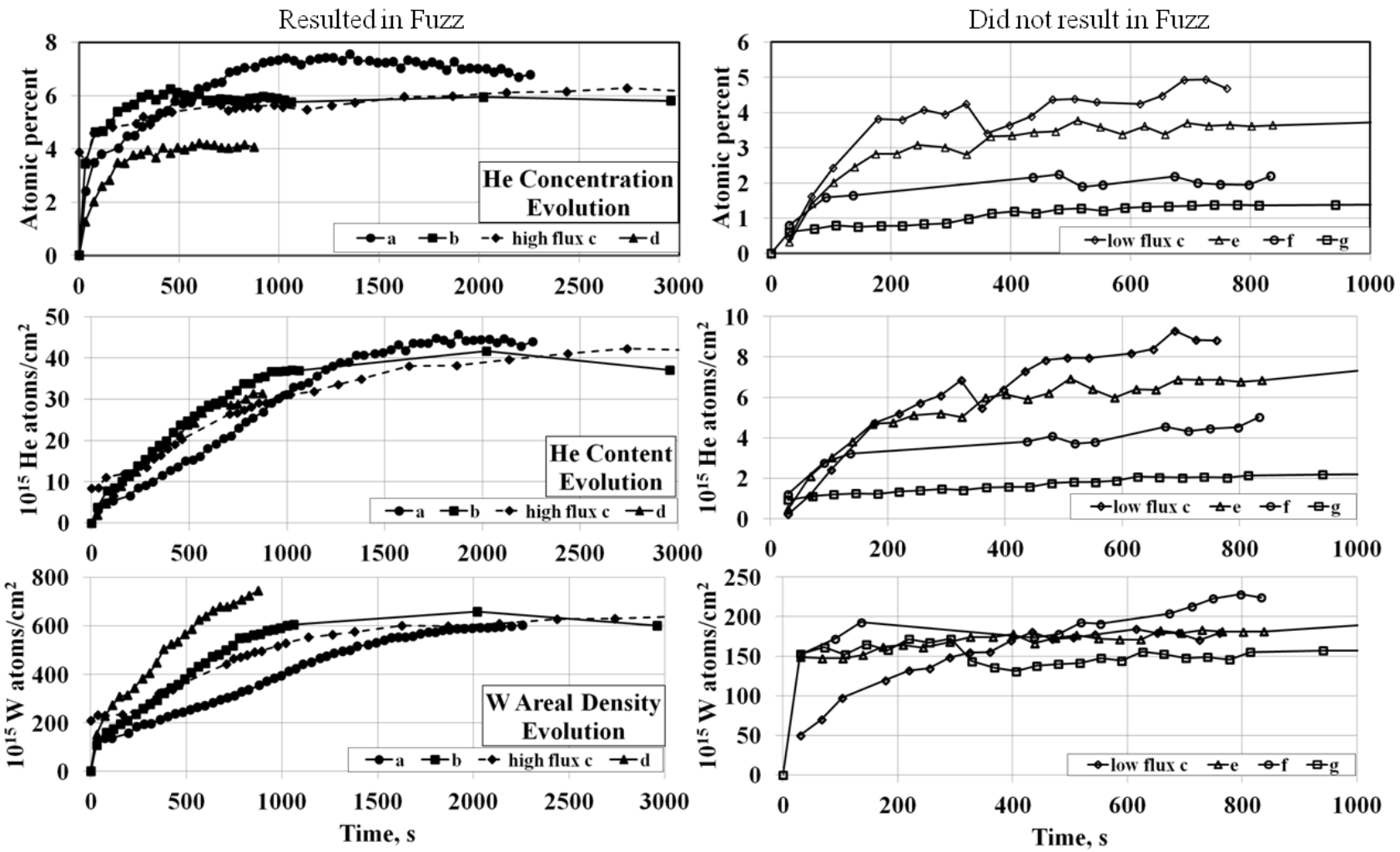

Figure 3-6 | Dynamic Helium concentration measurements.
Results from W samples that eventually developed fuzzy surfaces are on the left and results from samples that did not develop fuzzy surfaces are on the right. The He concentration evolution averaged through the W fuzz layer is on top, total He content evolution are in the middle panels, and, on bottom, the W areal density evolution of He-rich layers in W irradiated with He under the conditions of Table 3-1. Error bars were excluded for clarity. The uncertainty for the He concentration is approximately 15% The error for the W areal density is typically 3%.

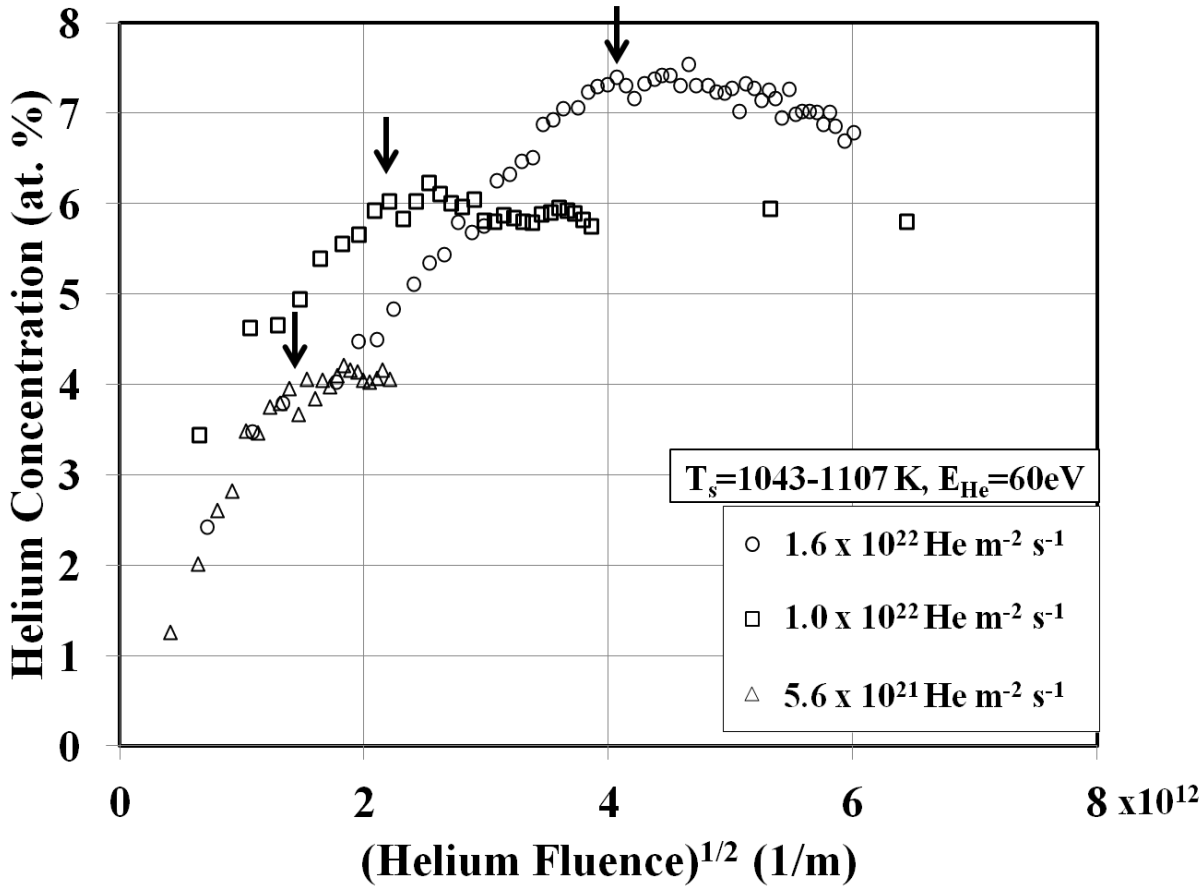

Figure 3-7 | Dynamic average He concentration of W fuzz layer measured using *in situ* ERD during the He irradiation.
The arrows are a guide to approximate the fluence reached when the He concentration saturates.

Over the W fuzz growth parameter range of this study, the He concentration saturates to a value between 1.5 and 7 at. %. This He concentration range is in agreement with post exposure measurements shown in Chapter 2. The value of this saturation level and time to saturation are dependent on the growth conditions. The He concentration appears to be monotonic with surface temperature. This is opposite to hydrogenic retention, where retention decreases rapidly with temperature. This demonstrates that there are fundamental differences between H/D/T trapping and He trapping (i.e. vacancy trapping vs. bubble filling). Previous ex situ measurements did not show such a clear relationship with surface temperature. It also appears that the He concentration starts to decrease after the fuzz has begun to grow. The surface temperature in these measurements is near one of the large He release peaks as observed in thermal desorption spectroscopy like in [32]. It is conceivable that there is a competition between the thermal release and defect trapping of He near these surface temperatures. Performing systematic scans in surface temperature, ion energy, and flux density could provide valuable insight into the mechanisms involved in the surface modifications. The measurements performed during the irradiation set a limit on how models of W fuzz growth incorporate the He influence in the nanostructure formation.

After the plasma exposure was ceased, these He concentration levels remained in the samples. This means that the He measured during exposure is truly that which is permanently trapped. Thus, there is no significant contribution of solute interstitial He in W observed in the measurements. Also, the amount of He in the space between the nano-tendrils is negligible, as it should be. As was suggested with the measurements in Chapter 2, the He concentration measured is inconsistent (too low by factor of 5-10) with speculation of void creation by loop-punching He bubbles. The presence of high pressure He certainly provides stresses to sustain W fuzz development but cannot directly explain fuzz growth. Also, the bubbles deform the surface, creating trapping sites for W adatoms [19]. In the low temperature regime, the W does not readily move around the He bubbles so fuzz is not created. As the surface temperature is increased, the W congregates to the bubble apexes and ridges where new bubbles can form and the process repeated [37]. The He supply rate has to be adequate for fuzz to develop, as was observed with sample C. This shows that there is a He flux density threshold for W fuzz growth as well.

3.5 Summary

In situ elastic recoil detection analysis was developed to investigate the role of the dynamic He concentration in the development of the nano-structuring of W surfaces that may be present in future fusion experiments. The adverse conditions of the DIONISOS plasma exposure chamber were mitigated by proper shielding of the solid state charged particle detector and through data analysis practices.

The He concentration was found to saturate at levels of 1 – 7 atomic percent depending on the specific exposure conditions with concentrations in fuzz general increasing as flux density increased. The measurements also showed an incubation period before the He concentration reaches a saturation level, and after which fuzz growth starts in earnest, that is dependent on the flux density. The dynamic measurement provides a basis for models on how much the average He concentration can be in evaluating the mechanisms involved in the nanostructuring of the W surface. These concentrations are not adequate to support loop-punching as a fuzz growth mechanism. The individual He concentration depth profiles of fully developed W fuzz layers show the He concentration to be uniform through the measurable "depth," which varies with the porosity of the He containing layer. Thus, the fuzz can be seen as highly structured nano-tendrils that have uniform single at. % He concentration throughout their depth.

Helium agglomeration and elevated surface temperature are the critical ingredients in the process that results in W fuzz from He irradiation [26]. Current theories and modeling suggest that the nucleation of high pressure, high density He bubbles at trapping sites progress into clusters, deforming the W surface and providing the initial deformation that leads to tendril growth [39,61].

3.6 Outlook

During the first plasma exposure tests in DIONISOS, the EMI protection was not available to the detector and the signal was too noisy in most discharge conditions. A noise free operating point was found when the input power and magnetic field were high enough for the plasma to be in the helicon wave-coupled mode. As mentioned in Chapter 1, the unique surface morphology that developed in this particular wave-coupled mode was in stark contrast to "normal" W fuzz and changed the direction of my research. There are many other aspects of the dynamic He concentration measurement that could be explored, but in terms of W fuzz growth, the conclusion that the He concentration is too low to represent bubbles bursting suffices for this thesis.

The remainder of this thesis is focused on characterizing why and how the surface morphology changed, since the nano-tendril bundles and single nano-tendrils provided a unique perspective on this family of surface morphology changes. The discovery of single nano-tendrils with aspect ratios of length to radius of 100 to 1 prompted an investigation into the possibility that nano-tendrils grow by similar mechanisms as metal whiskers in other fields of research. The whisker growth mode has many models, but one in particular stood out for its applicability to plasma exposure, the electric field nucleation theory of whisker nucleation and growth by electromigration. This hypothesis is tested in Chapter 4.

4 Nano-tendril bundles & Experimental investigation on the effect of plasma sheath electric field in the growth of tungsten fuzz

Following the results of the previous chapters, the mechanisms responsible for and controlling the growth of tungsten (W) nano-tendrils (or "fuzz") under low-energy helium (He) plasma exposure remain unclear. Through the *in situ* ERD He concentration measurements, the model that over pressurized He bubbles developed to cause deformation was eliminated as a cause. In this chapter, another test was devised that decoupled the plasma sheath-produced electric field and the He ion energy in order to determine the role of the surface electric field in fuzz growth. This was motivated by a theoretical paper [62] that provided an explanation for whisker growth in other metals due to the presence of an electric field perpendicular to the surface. In plasmas, a surface electric field is naturally present due to the sheath. However, the results show that the sheath electric field has little impact on nano-tendril growth, eliminating another possible cause for tendril growth. The well-established necessary growth conditions for W fuzz were maintained with He ion flux density $\Gamma_{He} > 10^{21}$ He·m^{-2}·s^{-1}, surface temperature $T_s = 1273$ K, He ion energy $E_{He} = 64$ eV, and He ion fluence $\Phi_{He} > 10^{24}$ He·m^{-2}. A grid is situated between the W sample and plasma, with the grid and sample potentials independently controlled in order to control the electric field at the surface of the sample while maintaining the same incident He ion energy to the surface. A calculation of the potential profile in the drift space between the grid and sample was used to account for space charge effects and calculate the electric field at the surface of the sample. Tungsten fuzz formed at all electric fields tested, even near zero electric field. Also, the depth of the resulting W fuzz layer was unaltered by the electric field when compared to the calculated depth determined from an empirical growth model. The conclusion is that the sheath electric field is not a necessary factor in producing nano-tendril growth and is, therefore, not controlling the growth. The results of this chapter were published in the Journal of Nuclear Materials [63].

4.1 Motivation

4.1.1 Plasma sheath electric field

Based on the results in Chapter 3, it is known that the He bubbles do not possess the necessary He pressure to overcome the strength of the W nor does the surface have a high enough He concentration to effectively lower the surface energy of W. Given the extreme environment that results in W fuzz growth, there are other possible mechanisms that could lead to nano-tendril growth.

The majority of experiments involving W fuzz growth use low temperature plasma ($T_e < 10$ eV) as the source of the He ions. He ions are extracted from the plasma through the plasma

sheath to a biased W sample. In most cases, the potential drop across the plasma sheath is on the order of 10 V, but the thickness of the plasma sheath is 10^{-5} – 10^{-4} m in linear plasma devices and tokamak divertor plasma environments. Therefore, there is an electric field 10^5 - 10^6 $V \cdot m^{-1}$ perpendicular to the solid surface. Surface structures due to thermal grooving and ion bombardment cause non-ideal surfaces that can further enhance the local electric field due to the plasma sheath by another two orders of magnitude [62,64,65]. Research in field ion microscopy (FIM), in which a high aspect ratio W probe is biased to a few kilovolts, shows that W electromigration, as a result of the large electric field, effectively "builds up" the probe tip [66,67]. Probe tip build up might be similar to how W nano-tendrils in W fuzz grow, but the electric field in FIM experiments is orders of magnitude larger than that due to a plasma sheath. In addition to the large probe bias, FIM experiments use He as an imaging gas. "Microprotrusions" with radii similar to the nano-tendrils of W fuzz are observed to grow on probe tips, which lead to arcing and vacuum breakdown. The growth of these "microprotrusions" is attributed to surface diffusion activated by He ion bombardment in the presence of large electric fields [68]. Even though plasma based W fuzz growth experiments have a lower electric field than in FIM, the plasma devices have a much larger ion flux density incident on the surface. Thus, there may be a synergistic effect of the sheath electric field and ion bombardment that results in W fuzz growth.

4.1.2 Nano-Tendril Bundles and Stand-alone nano-tendrils

While developing the *in situ* ERD technique for the DIONISOS exposure chamber, a new variation in W fuzz growth was observed, specifically, isolated nano-tendril "bundles", whose mere presence and geometry provide critical insights into fuzz growth mechanisms. Helicon plasma sources, like the one in the DIONISOS experiment, exhibit multiple modes of operation, a capacitively-coupled, an inductively-coupled, and a wave-coupled mode. The mode transitions are accompanied by sudden jumps in plasma density. The radial density profile of the wave-coupled plasma is peaked at the center while having an approximately uniform electron temperature across the plasma column. The first observation of the new bundle structures occurred with the flux density on axis approximately 1.6 x 10^{22} $He \cdot m^{-2} \cdot s^{-1}$ that dropped off linearly with plasma radius. The surface temperature was 1050 K and the target bias was -50 V. At these exposure conditions in the wave-coupled mode, three disparate regions of growth were observed, separated by different radii.

The nanostructure typically seen as W fuzz is characterized by 10-50 nm wide tendrils, intertwined in a volumetric layer covering the plasma facing surface, referred to as uniform W fuzz growth for the remainder of the thesis. Figure 4-1 shows progressively more magnified images of the new variant of W fuzz discovered in the DIONISOS plasma chamber. Towards the center of the plasma column in the wave-coupled exposures, discrete bundles of nano-tendrils populate the surface instead of uniform fuzz growth, and the surface no longer appears optically black. There is uniform fuzz growth on the outer radius of the target, with a transition region between the uniform fuzz growth and nano-tendril bundle growth. The nano-tendrils within the bundles have similar size characteristic to uniform W fuzz nano-tendrils grown at similar surface temperatures. The size of the nano-tendrils has been shown to depend on surface temperature as in [55], so this is not surprising. The area of the surface comprising the footprint of the nano-tendril bundles is only a few microns in

diameter, which is smaller than the grain size for these targets. The height of the nano-tendril bundles is several microns high, and can exceed the diameter of the base of the bundle. Even single nano-tendrils of approximately 10 nanometers in diameter and several microns in length are observed in the transition region separated by large distances (10s of microns) from other such nano-tendrils, as shown in Fig. 4-2. These isolated structures that grow away from the surface demonstrate the influential role of surface diffusion in the nanostructuring of W.

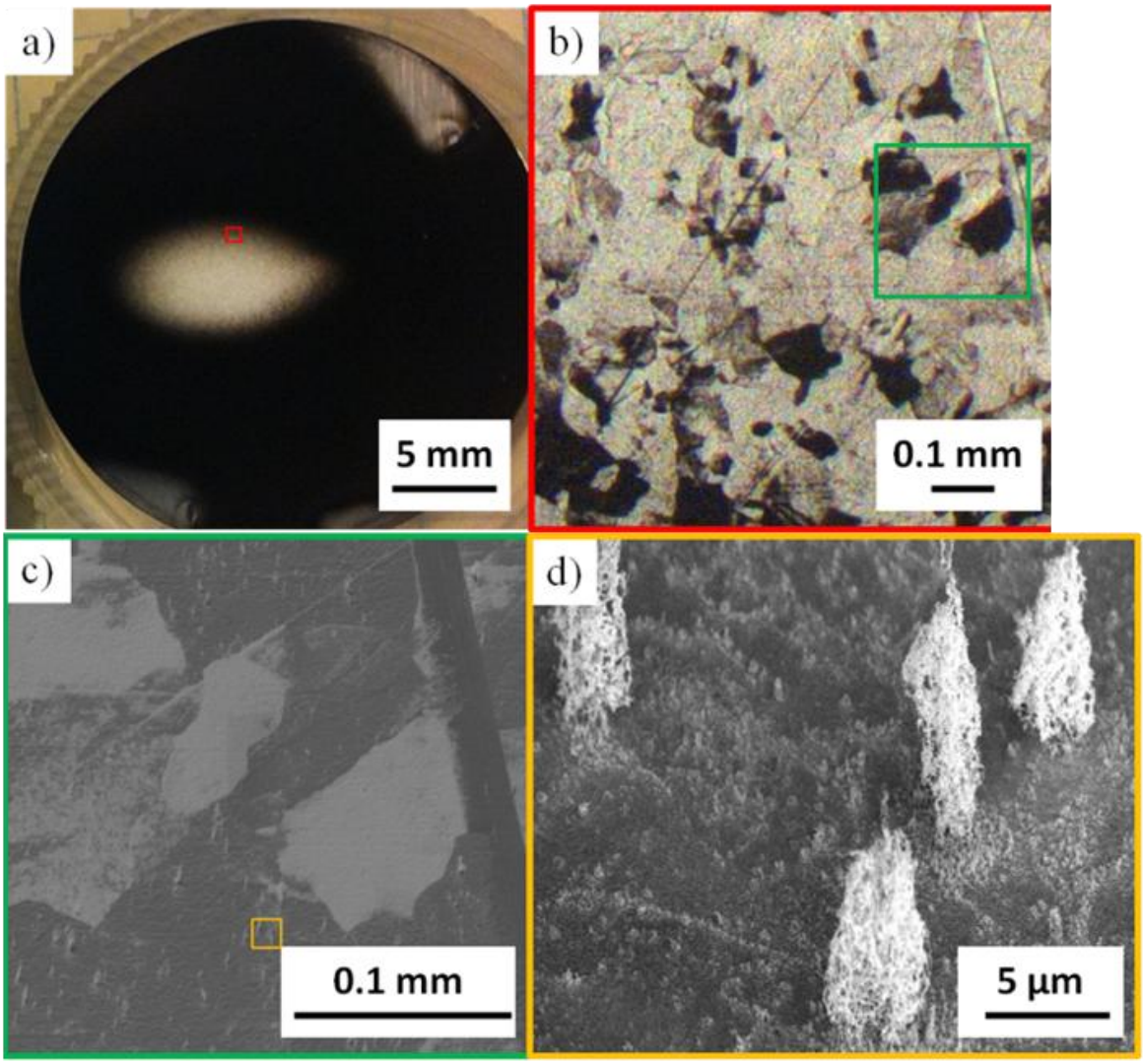

Figure 4-1 | Nano-tendril bundles.
Progressive imaging of the area of interest on a W target exposed to a wave-coupled helicon plasma discharge with peak flux density of 1.6 x 10^{22} $He \cdot m^{-2} \cdot s^{-1}$, a surface temperature of 1050 K, and target bias of -50 V. a) Photograph of W target after exposure showing characteristic blackening of surface due to nanostructuring except near the center of the target, which retained most of the original reflectivity as prior to exposure. b) Optical micrograph showing the detail of the transition region marked by the red outline in a). The black grains contain uniform W fuzz growth. c) Scanning electron micrograph showing the detail of the green outline in b). The light grains contain uniform W fuzz growth. The nano-tendril bundles populate the dark grains. d) Scanning electron micrograph showing the detail of the yellow outline in c). The viewing angle of the two SEM images is 52 degrees from normal to show the height of the nano-tendril bundles.

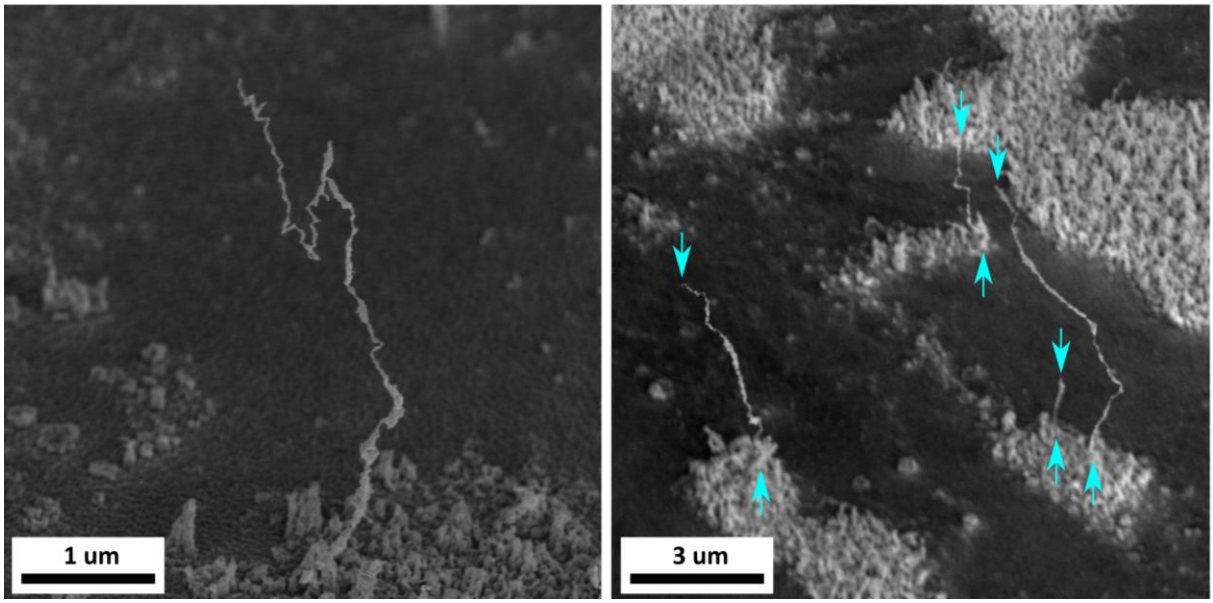

Figure 4-2|Single W whisker grown from the surface of a W target in the DIONISOS exposure chamber.

The remainder of the surface around the nano-tendril bundles appears pin-holey, similar to surfaces that have been loaded with He that is released during temperature ramps like in [69]. The transition region shows grain-to-grain variation in morphology, similarly as in [70] and [71], due to varying grain crystallographic orientation, which will be elaborated on in Chapter 6. The crystallographic orientation dependence indicates that these new structures are dependent on the ion energy. Also in Chapter 6, the ion energy distribution in the wave-coupled helicon mode of the DIONISOS plasma chamber is the studied further to illuminate the reason for the appearance of the new W fuzz variation.

The stand-alone W nano-tendrils are similar in size to the nano-tendrils of W fuzz, but are observed freestanding without neighboring nano-tendrils for support. The similarity in aspect ratio of these solitary W nano-tendrils to other metal whiskers [72–74] studied since the mid-20th century suggests W nano-tendril and fuzz growth could be based on similar principles as metal whisker growth. Whisker growth is another example of dramatic surface modifications, and so it is natural to consider the possibility of a link between whiskers and fuzz. A model for metal whisker growth recently published [62] suggests that large electric fields induced by surface inhomogeneity could cause whisker nucleation and enhance whisker growth. Applied electric fields from the plasma sheath could play a role in initiating or enhancing the whisker/nano-tendril growth process that develops into W fuzz. It is a combination of these observations that lead us to investigate the possible role of the sheath electric field in the nucleation and/or growth of W fuzz.

The electric field could affect W fuzz growth in two ways. First, the electric field polarization energy could affect the nucleation mechanism of nano-tendrils. As it is discussed in [62], the slender shape of a nano-scale metal whisker can possess electric field polarization energy due to the electric field within the metal whisker. The barrier to nucleate such metal whiskers is decreased when an electric field is present at the surface. The nucleation barrier

derived by Karpov takes into consideration the surface electric fields inherent to metals just by virtue of surface inhomogeneity, which actually serves as the dominant source of polarization energy in his model. The order of this inherent electric field is 10^8 $V \cdot m^{-1}$ for materials similar to W [75] as determined by the spatial variation of the surface electric potential. Since the electric potential variation is inherent to the material, the effect it may have in this experiment cannot not be diminished when coupled with ion bombardment as in FIM experiments. However, the electric potential variation alone would also be present during the high temperature annealing of samples, and nano-tendril or whisker growth is not observed after a 1 hour anneal at 1273 K.

The addition of an applied electric field via the plasma sheath decreases the nucleation barrier further. Thus, by decreasing the applied electric field, the nucleation density of metal whiskers on the surface would decrease. The decreased nucleation density would require a larger incubation fluence for nano-tendril growth. Therefore, the effect of decreasing the sheath electric field on nano-tendril nucleation would be observed through modifications to the incubation fluence.

Second, the electric polarization energy could also provide additional stimulus for nano-tendril growth. The growth rate of metal whiskers in an external electric field is proportional to the polarization energy [62], $\mathbb{E} = -\varepsilon\alpha E^2$, where ε is the permittivity, α is the polarizability, and E is the electric field strength. Therefore, by decreasing the sheath electric field, one would expect the nano-tendril and W fuzz layer growth rate to decrease as well. Based on these proposed mechanisms, the overall effect of decreasing the sheath electric field would be to decrease W fuzz growth, due to increased incubation fluence and decreased growth rate after incubation.

4.2 Experimental Materials and Methods

4.2.1 Growing tungsten Fuzz

The experiment was conducted in the DIONISOS plasma exposure chamber [25] using continuous He plasma. First, a sample without a grid to control the electric field was grown to establish a control case that had the necessary conditions for fuzz growth. The subsequent exposures testing the effect of electric field would be conducted to match the exposure conditions of the control case as closely as possible. W samples were 99.95 % pure PLANSEE W disks that were 1 mm thick and 25 mm in diameter. The surfaces were mechanically polished and then electropolished using a 4 % sodium hydroxide solution kept at 0 °C. The control W sample was mounted onto a ceramic heater that maintains the sample temperature using feedback from a thermocouple mounted inside the heater. The heater was taken to 1273 K. At this temperature, the heat flux from the plasma when the sample is biased to -50 V is comparable to the thermal radiation of polished W. At the beginning of the exposure, the temperature of the surface of the W sample is 1273 K. As the surface morphology changes to W fuzz, the emissivity increases to 1 [24], and the surface temperature is calculated to be 20 K lower than the heater temperature. Helium plasma was generated with an electron density of 6 x 10^{17} m^{-3} and an electron temperature of 2.8 eV as determined from a double Langmuir probe. This results in a He flux density of 3 x 10^{21}

$He \cdot m^{-2} \cdot s^{-1}$, which is in the range for fuzz growth (> 10^{20} $He \cdot m^{-2} \cdot s^{-1}$) [23]. The plasma potential was estimated from an uncompensated Langmuir probe to be 15 V. The plasma potential measurement was further corroborated by a four-gridded retarding field energy analyzer, which measured the peak in He ion energy to be 14 eV while the plasma facing grid was floating. The sample was biased with an additional -50 V to bring the final He ion incident energy to 64 eV. The sample was then irradiated in the plasma to a fluence of 7.5 x 10^{24} $He \cdot m^{-2}$, which is greater than the observed incubation fluence for W fuzz with ions of this energy [60].

4.2.2 Separating ion energy from surface electric field

At the interface between the plasma and the sample surface, an electric field is naturally generated. The magnitude of the electric field, $|E| = |d\phi/dx|$, as determined from Poisson's equation with conservation of energy and flux [76], a solution known as the Child-Langmuir law, and is

$$|E| = 2\left(\frac{J_i}{\epsilon_0}\sqrt{\frac{m_i}{2e}}\right)^{1/2}\left(V_p - V_{bias}\right)^{1/4}. \tag{4.1}$$

where J_i is the ion current density entering the sheath that satisfies the Bohm criterion, ϵ_0 is the permittivity of free space, m_i is the mass of the ions, e is the elementary charge, and $V_p - V_{bias}$ is the potential difference between the plasma and the sample surface.

The electric field at the surface of a sample exposed directly to the plasma described in section 2.1 with a measured current density of 487 $A \cdot m^{-2}$, plasma potential of 14 V, and a sample bias of -50 V is 5 x 10^5 $V \cdot m^{-1}$. To gain control over the electric field while simultaneously maintaining control over the He ion energy, a grid was situated between the plasma and the sample. The grid wire spacing was chosen to adequately shield out the influence of the plasma sheath from the sample surface. The characteristic length to do so is proportional to the Debye length,

$$\lambda_D = \sqrt{\frac{\varepsilon_0 k T_e}{e^2 n_e}} \tag{4.2}$$

For these plasma conditions, the Debye length is 14 μm. To keep the plasma from leaking into the drift space between the grid and sample, the wire spacing of the grid has to have a maximum dimension that is only 2 - 4 Debye lengths [77]. The gap size of the grid used in this experiment is 40 μm, or approximately $3\lambda_D$, so the criterion to shield out the plasma from the sample is met for a floating grid. Additionally, the grid is biased negatively, which extends the sheath and improves shielding. To test the plasma shielding capabilities of the grid, a -50 V bias potential was placed on the grid, and only ion current was measured on the sample for a sample voltage sweep from -100 V to +100 V, indicating that the plasma was

adequately shielded out of the drift space since no electron current could be measured even for positive sample bias with $V > T_e$.

The 25 μm thick grid has a transparency of 0.56 and is mounted on a 150 μm thick tantalum grid holder. The grid holder is mounted in front of the sample with 230 μm thick alumina spacers between the grid holder and the sample. This creates a total drift space thickness of 380 μm. The lateral size of the alumina spacers is comparable to their thickness. Eight alumina spacers were positioned in a circular array far away from the interaction region at the center of the sample holder to minimize the thermal conduction from the sample to the molybdenum clamping ring, which held the grid holder and alumina spacers in place by compression. A schematic of the modified sample is shown in Fig. 4-3.

The grid diminishes the ion flux incident on the sample surface due to the finite transparency of the grid. For this experiment, the flux density was taken as the measured current to the sample through the grid divided by the surface area observed to have grown W fuzz after exposure. The flux density calculated from these measurements during the experiment was in the range 1.2 - 1.6 x 10^{21} $He \cdot m^{-2} \cdot s^{-1}$, which is similar to the flux density from the plasma multiplied by the transparency of the grid. The flux density and fluence measured in this way are used for the drift space potential profile calculations described in section 4.2.3 and for determining the expected W fuzz layer thickness described in section 4.2.4.

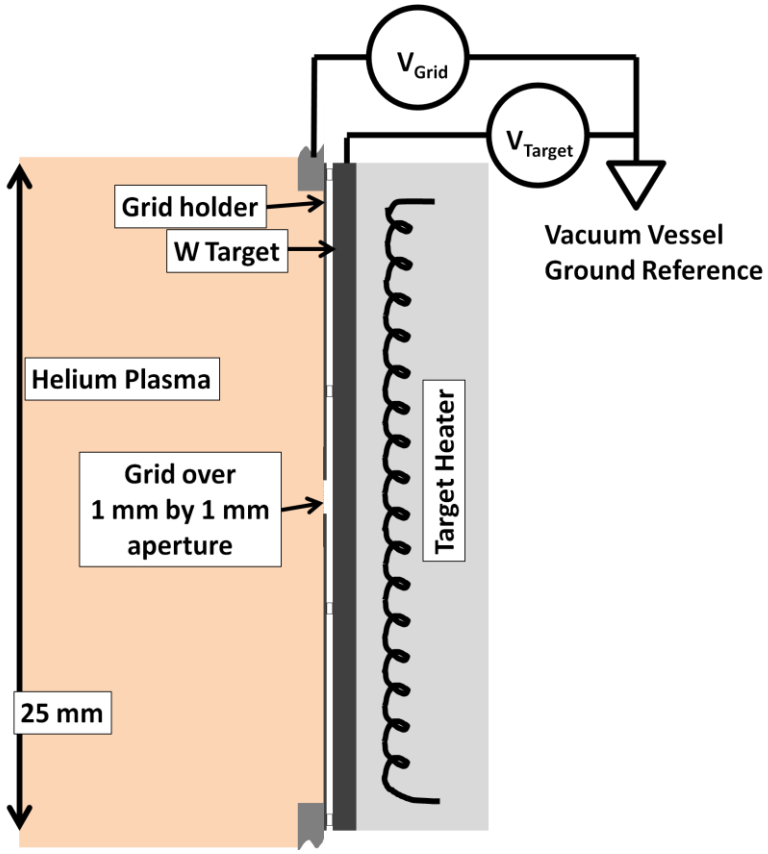

Figure 4-3 | Profile schematic of the modified sample with the grid mounted between the W surface and the He plasma.

4.2.3 Drift space potential profile

If there were no source of charge in the drift space, then the electric field would simply be the difference in potential between the grid and sample divided by the drift space distance. However, since the drift space contains ions extracted from the plasma, a potential distribution within the gap is present due to net positive space charge, and a subsequent electric field would be generated at the surface of the sample. Again, by solving Poisson's equation, along with continuity and conservation of energy, the potential distribution of the drift space [78] and the electric field at the surface of the sample were calculated. The 2D/3D effects of the grid wires were not taken into account as the drift space is an order of magnitude larger than the grid wires and spacing. The alumina spacers are very far removed from the grid area so that they do not affect the potential in the gap of the 1 mm by 1 mm irradiation region. Also, the calculation assumes there is no other source of charge in the drift space due to ionization. This is justified since the ionization mean free path is approximately 10 mm, which is 100 times the gap spacing. Also, the calculation assumes the ions are traversing the gap in one dimension perpendicular to the surface. There is some spread due to the thermal ion velocity distribution, but the effect on the potential distribution is assumed to be secondary to the average speed. The drift space distance is substantially larger than the ion-ion collision mean free path, which is calculated to be 50 μm. Therefore, momentum transfer collisions between ions have to be considered because the ions can gain additional velocity spread through the gap.

To measure the energy spread through the drift space, the grid and sample was used as a single grid energy analyzer by sweeping the voltage on the sample, which acts as the collector for the energy analyzer, and holding the grid bias fixed. This measurement gives an ion energy spread through to the collector of 10 - 12 eV, assuming that the ions are extracted from the plasma at room temperature. This energy spread through the drift space is not incorporated in the space charge calculation, but the error introduced by neglecting the energy spread through the drift space is second order to the potential distribution calculated using the average extraction ion energy > 50 eV through the grid. The potential distribution was calculated under the above assumptions using the current density measured during the experiment. Shown in Fig. 4-4 are the potential profiles for grid biases of -50 V, -80 V, and -90 V, with the sample bias fixed at -50 V, thus holding the incident ion energy at 64 eV.

In the case where the grid and sample are both -50 V, the surface electric field due solely to space charge is approximately 10 % of the sheath electric field that would be at the sample surface without the grid. The lowest surface electric field was 3 % of the sheath electric field, which required the grid-to-sample potential difference to be 30 V for the gap spacing and current densities in this experiment (see Fig. 4-4).

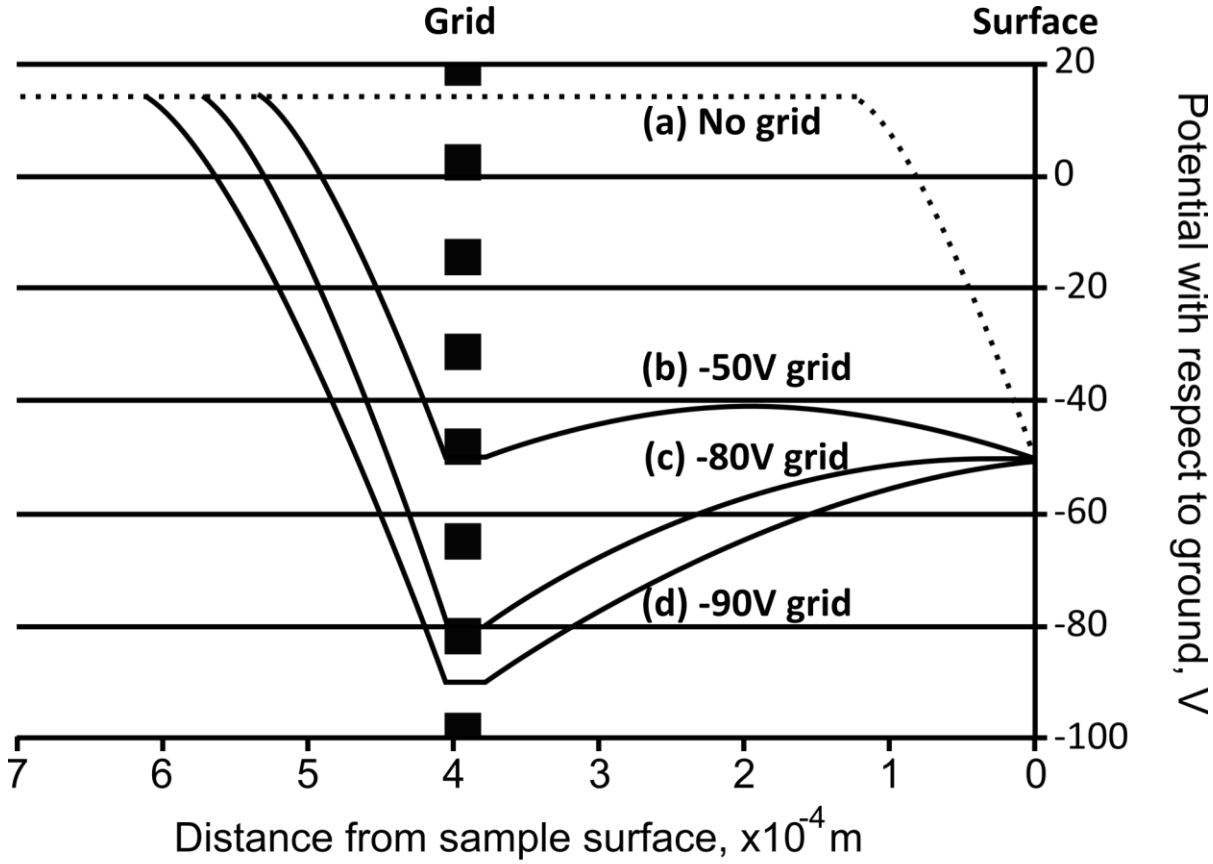

Figure 4-4 | Potential distributions with respect to ground calculated for the sheath potential drop and drift space.
Profile for (a) no grid and three exposures with grid biases of (b) -50 V, (c) -80 V, and (d) -90 V. The sample had a bias of -50 V and the plasma potential was measured to be 14 V. The grid is spaced 3.8×10^{-4} m from the sample surface located at x = 0.

4.2.4 Comparison to open plasma tungsten fuzz growth

In order to assess if changing the electric field affects the resulting fuzz layer, the grid-grown fuzz is compared to fuzz grown without the grid. However, due to small variations in plasma discharges, grid-sample mounting, and grid biasing, there are differences in the fluence for each exposure. The fuzz growth has been shown to follow diffusion-like growth in conditions similar to that used here [26]. Calculating the diffusion coefficient, D, at 1273 K using the pre-exponential factor of 9.9×10^{-14} $m^2 \cdot s^{-1}$ and activation energy of 0.71 eV, interpolated from data at 1120 K and 1320 K from the work of Baldwin and Doerner [26], based on this empirical formula, the expected thickness ($h_{Baldwin}$) of the resulting fuzz layers can be calculated from the fluence, or exposure time of each exposure,

$$h_{Baldwin} = \sqrt{2 \cdot D_{1273K} \cdot t}. \tag{4.3}$$

The fuzz layer depth was also shown to depend on the He flux density [23]. In order to account for the lower flux density used here compared to those for the Baldwin formula, a correction factor was applied from the flux density scan performed by Baldwin and colleagues [23]. The W fuzz growth rate saturates at a He flux density of 10^{22} $m^{-2}{\cdot}s^{-1}$. The flux density in this study is 1.2 - 3 x 10^{21} $m^{-2}{\cdot}s^{-1}$. The depth of the fuzz layer in [23] for a flux density similar to here was 1/5 that of the saturation fuzz layer depth. Thus, the expected fuzz layer depth is calculated from empirical data as

$$h_{cal} = \frac{1}{5} \cdot \sqrt{2 \cdot D_{1273K} \cdot t} \tag{4.4}$$

The fuzz layer depth was measured from cross section images made by Focused-Ion Beam (FIB) milling and compared to the empirical depth calculated with Eqn. (4.4).

4.3 Results

4.3.1 Morphology Comparison

The morphologies of W fuzz grown with and without the grid setup are shown in Fig. 4-5a and 4-5b, respectively, from a view normal to the surface. The electric field calculated for the two cases pictured are 5 x 10^5 $V{\cdot}m^{-1}$ for the no grid sample and 1.5 x 10^4 $V{\cdot}m^{-1}$ for the sample shielded by a grid biased at -80 V. The characteristic size of the nano-tendrils has not been altered compared to the control case, in agreement with the experimental evidence that the surface temperature has a strong influence on tendril size during W fuzz growth at these ion energies [55,79], either through surface tension or He bubble size. There is no fundamentally different nano-tendril morphology when the W sample is shielded behind a grid and is, therefore, not subjected to the plasma directly.

4.3.2 Growth Rate Comparison

When viewing this complex surface in the normal direction, it is unclear to what extent the sheath electric field played a role in the formation and growth of the fuzz. If the sheath electric field did play a role in the growth of W fuzz, one might expect the growth rate to be proportional to the square of the electric field through the electric polarization energy, as discussed in section 4.1. The depths of the fuzz layers grown with several low electric field situations were measured. The ratio of the grown fuzz layers to the calculated empirical value versus the magnitude of the calculated electric field is plotted in Fig. 4-6. The thickness of the fuzz layer, even with very low electric fields, is independent of the surface electric field (see Fig. 4-5c and 4-5d). Thus, it can be concluded that the sheath electric field of the plasma that is used to grow W fuzz does not factor into the resulting fuzz growth, in morphology or growth rate.

Additionally, a bias configuration was used that had a slightly retarding electric field at the surface of the sample, approximately 5% of the sheath electric field and is included in Fig. 4-6 as the point labelled “-90V”. The low positive field polarization did not affect the resulting

fuzz growth. As may be seen in Figs. 4-5 and 4-6, the fuzz layer and its growth are almost identical whether subjected directly to plasma or shielded; there is no drastic change in the growth of the fuzz layer.

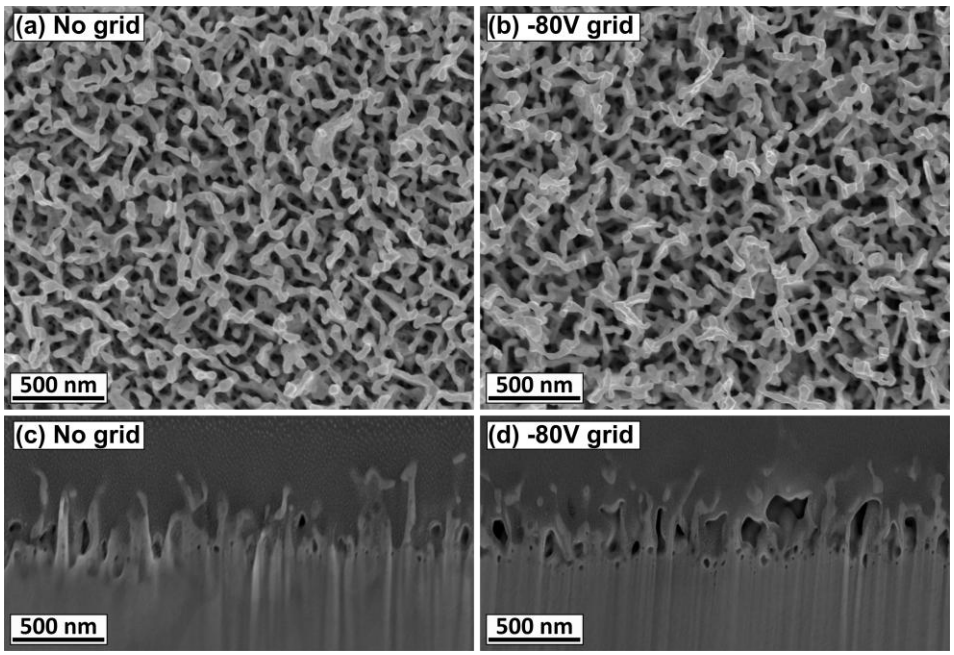

Figure 4-5 | Comparing tungsten fuzz for control case and low electric field case.
SEM micrographs showing the view of the control tungsten fuzz sample grown at 1273 K with 64 eV ions at 3.0 x 10^{21} He·m^{-2}·s^{-1} to a fluence of 7.5 x 10^{24} He·m^{-2} (a) normal to the surface and (c) in cross section. Also, the view of the W fuzz sample grown with the same plasma, but shielded by a grid with a bias of -80 V, (b) normal to the surface and (d) in cross section. The flux density and fluence to the surface of the sample in the shielded case were 1.6 x 10^{21} He·m^{-2}·s^{-1} and 6.9 x 10^{24} He·m^{-2}, respectively.

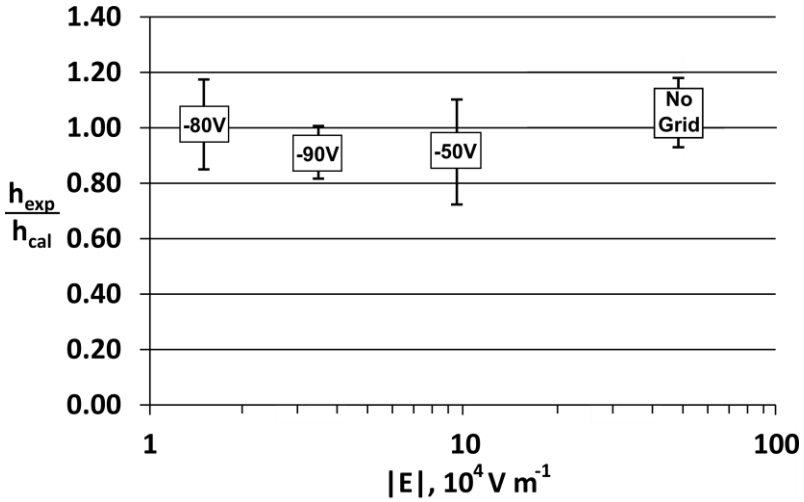

Figure 4-6 | Fuzz layer thickness versus surface electric field magnitude.
Fuzz layer thickness, h_{exp}, as measured by focused ion beam milling normalized to the fuzz layer thickness, h_{cal}, calculated using the empirical growth model Eqn. (4.4). The results are shown for the four biasing conditions of Fig. 4-4, corresponding to the data labels. The error bars denote the uncertainty in determining the layer thickness from cross section images.

4.3.3 Discussion

Although the plasma sheath electric field does not factor into the growth of W fuzz, this experiment does not address the possibility suggested in section 4.1 that inherent variations in surface potential due to the minimization of the electrochemical potential can generate large electric fields that could induce whisker/nano-tendril nucleation when coupled with He ion bombardment or He implantation. The FIM experiments do see a broad surface diffusion mechanism that is activated with the applied bias, but the microprotrusions were observed to be activated with the ion bombardment. The possibility of He bubbles factoring into the FIM experiments were considered by Schwoebel in [68], but the conclusion was that at the higher temperatures of 1200 K, similar to fuzz growth, the He bubbles could not nucleate and grow, unlike He plasma irradiated W, which readily develop He nano-bubble fields. The lower He flux and higher ion energy in the FIM experiments as compared to the plasma irradiation may be the reason for this difference in the bubble behavior. Even so, ion bombardment enhanced diffusion is worth pursuing as a possible mechanism to be tested in the development of W nano-tendrils. This will be a focus of Chapter 6.

Upon observing the solitary W nano-tendrils in DIONISOS [80] it is natural to ask why those exposures did not produce common uniform W fuzz, The inception of the experiment reported in this chapter was to test whether surface electric fields enabled W fuzz growth because of the ubiquity of the plasma sheath in the various observations of W fuzz growth. The null result of this experiment prompted a continued investigation of these intriguing new nano-tendril morphologies and their growth mechanisms. After this study of the electric field concluded, the grid-sample setup was used to measure the ion energy distribution function (IEDF) under the plasma conditions that produce solitary and bundled W nano-tendrils. The IEDF measurement showed that the incident ion energy distribution was more complex than originally thought. A detailed evaluation of the helicon wave-coupled mode plasma is given in Chapter 5.

4.4 Summary

By implementing an appropriate grid between the W sample and the He plasma, the electric field was decreased at the surface of the sample to 3 % of the electric field that would be present at the sample from the plasma sheath. The set up tested whether the sheath electric field plays a role in the nucleation or subsequent growth of the nano-tendril morphology that occurs when He plasma irradiates a W surface at elevated surface temperature.

The resulting W fuzz layers grown in this chapter, with direct exposure to the plasma, with a much lower electric field, and even with a low retarding electric field, are all similar in terms of their nano-tendril size and layer depth, when normalized to an empirical layer depth calculation. The conclusion is that at a temperature of 1273 K and incident ion energy of 64 eV, the sheath electric field does not impact the nucleation process nor the growth rate of the nano-tendrils that form when He plasma irradiates W at elevated surface temperatures.

5 Bimodal ion energy distributions in helicon wave-coupled helium plasma

Helium ion energy distributions were measured in the helicon wave-coupled plasma of the DIONISOS experiment with a retarding field energy analyzer in order to illuminate the role of average and oscillatory ion energy on nano-tendril formation. The shape of the energy distribution is bimodal, characteristic of RF plasma potential modulation. The bimodal distribution is located within a radius of 8 mm while the quartz tube of the plasma source has an inner radius of 22 mm. The ion energy distribution rapidly changes from bimodal to a single peak in the radius range of 7 to 9 mm. The average ion energy is approximately uniform across the plasma column including the bimodal and single peak regions. The widths of the bimodal distribution, ΔE, in the wave-coupled mode are large compared to the time-averaged ion energy, $\langle E \rangle$. On axis (r = 0), $\Delta E/\langle E \rangle \lesssim 3.4$, and at a radius near the edge of the plasma column (r = 22 mm), $\Delta E/\langle E \rangle$ ~1.2. The discharge parameter space is scanned to investigate the effects of magnetic field, input power, and chamber fill pressure on the wave-coupled mode that exhibits sharp spatial variation in the ion energy distribution. The results from this chapter are currently under review for publication [81].

5.1 Helicon plasma source discharge modes

For the study of tungsten fuzz in this thesis, a helicon plasma source has been used. The capability of helicon plasma devices to reach high plasma density with low electron temperature make them suitable for studying plasma-material interactions, such as the development of tungsten fuzz, because they produce reactor-relevant particle fluxes with controllable ion energy. As shown in Chapter 4, while using the helicon wave-coupled (W) mode in DIONISOS, the surface response varied significantly with radius on the target. The W mode used in these experiments has a peaked flux density profile and a fairly uniform electron temperature across the radius, as is seen by others using helicon plasma sources [82]. The layer thickness of tungsten fuzz on samples exposed to a flux density gradient has been shown elsewhere to be proportional to the flux density through the resulting exposure fluence gradient [14,33]. For samples exposed to the W mode of the DIONISOS plasma, the thickest layer of tungsten fuzz would therefore be expected at the center of the sample where the flux density is highest. However, instead the opposite occurred with the surface remaining predominantly smooth, with only sparse microscopic bundles of tungsten fuzz out to a certain radius of approximately 5 mm. Outside of this radius, typical tungsten fuzz is present at layer thicknesses predictable from empirical growth models that are based on the exposure fluence and sample temperature. The drastic change in the surface morphology on a single sample motivated this chapter on the study of the ion energy distribution in the plasma.

A uniform electron temperature across the radius of the plasma implies the plasma source is suitable for studies that require uniform incident ion energy across the targets. However, the plasma potential can oscillate due to radiofrequency (RF) excitation. From previous studies on helicon devices, the amplitude of plasma potential oscillations is large in the capacitively-coupled (E) mode, with the peak-to-peak potential double the average potential [43,83–85]. With increasing the magnetic field or antenna power, the average potential and modulation amplitude decrease when the plasma source transitions to the inductively-couple (H) mode. The plasma potential modulation amplitude in the H mode is comparable to the average plasma potential [84]. Increasing the magnetic field or input power further increases the plasma density such that the dispersion relation for helicon wave propagation is satisfied, and the plasma transitions to the W mode. The plasma potential decreases subtly through the H to W mode transition [86]. However, the plasma potential modulations in the W mode have not been discussed in the literature. In this study, the peak-to-peak plasma potential exceeds the average plasma potential by a factor of 2-4 in the W mode under the conditions studied so far. The modulation in the incident ion energy using the bimodal W mode plasma was the cause of the differences in nanostructure growth [87]. With ion irradiation energies at or below the sputtering threshold for a given target, the modulation of the incident ion energy provide new parameters to explore in plasma-surface interactions, modulated ion-induced adatom production, modulated low energy sputtering yields, and, in general, the effect of RF sheaths on plasma-material interactions which continues to be a topic of interest in fusion.

This chapter provides an overview of the diagnostics used to measure the plasma parameters of the DIONISOS helicon plasma chamber in a mid-power H mode and high-power W mode. Then, how the ion energy distribution changes with device parameters is shown, with focus on the bimodal ion energy distribution function in the W mode, and discuss of the nature of the plasma potential modulation in context with theories of helicon plasma discharge physics.

5.2 DIONISOS plasma chamber

The DIONISOS plasma chamber is shown schematically in Fig. 5-1. A Nagoya Type III antenna, which has a radius of 30 mm and a length of 110 mm, is supplied with radio-frequency (RF) power at f_{RF} = 13.56 MHz and surrounds a quartz tube into which the helium (He) gas is fed. Reflected power to the RF power supply is minimized by tuning the capacitors in the impedance matching network and is typically 1% of the output power of the supply. Four magnetic field coils immerse the plasma source and target chamber in a DC axial magnetic field that does not vary by more than 1.5% per cm on the chamber axis, and not by more than 0.5% per centimeter across the diameter at the axial location of the measurements made in this study. The device uses active cooling for the magnetic field coils and RF circuit so that the plasma source can be operated continuously and stationary. Once the plasma reaches equilibrium conditions, measurements are made at multiple radial locations. The plasma from the source region (x < -0.25 m) enters the target chamber, which has a radial bore radius of 0.1 m. The axial magnetic field maintains the plasma with a radius ~25 mm in the target chamber where plasma diagnostics and material targets can be placed. A target of interest is usually mounted on a sample holder that extends into the plasma at an axial position 0.38 m from the end of the antenna. At this axial position, measurements of the plasma density (n_e) and electron temperature (T_e) are made with a double Langmuir probe

(DLP) and of the ion energy distribution function (IEDF) with a retarding field energy analyzer (RFEA).

The measurements from these diagnostics were taken sequentially under reproducible discharge conditions. The probe measurements were taken with a grounded target in place. Due to the size of the RFEA, the target holder was removed during IEDF measurements. With the target holder removed, the plasma terminates partially on the grounded housing of the RFEA probe and partially on the grounded vacuum chamber wall. The differences in the boundary conditions show some changes in the mode coupling for the various discharge parameters.

Both the H and the W mode used as typical cases in this study were created with background neutral He gas fill pressures of 3.8 Pa. The model H mode used 700 W of RF input power with a background magnetic field of 0.046 T, while the model W mode used 1000 W of the RF power with a larger magnetic field of 0.077 T. A summary of the discharge conditions along with the measured values of the plasma parameters on the chamber axis for these model H and W modes is given in Table 5-1. The W mode is identified by the peaked flux density radial profile and the bright emission of light at the center axis to a radius of approximately 5 mm. Additionally, the bimodal IEDF within the bright central axis is characteristic of the high power, high magnetic field W mode. The H mode has a flux density gradient much lower than the W mode and uniform light emission across the radius of the plasma column.

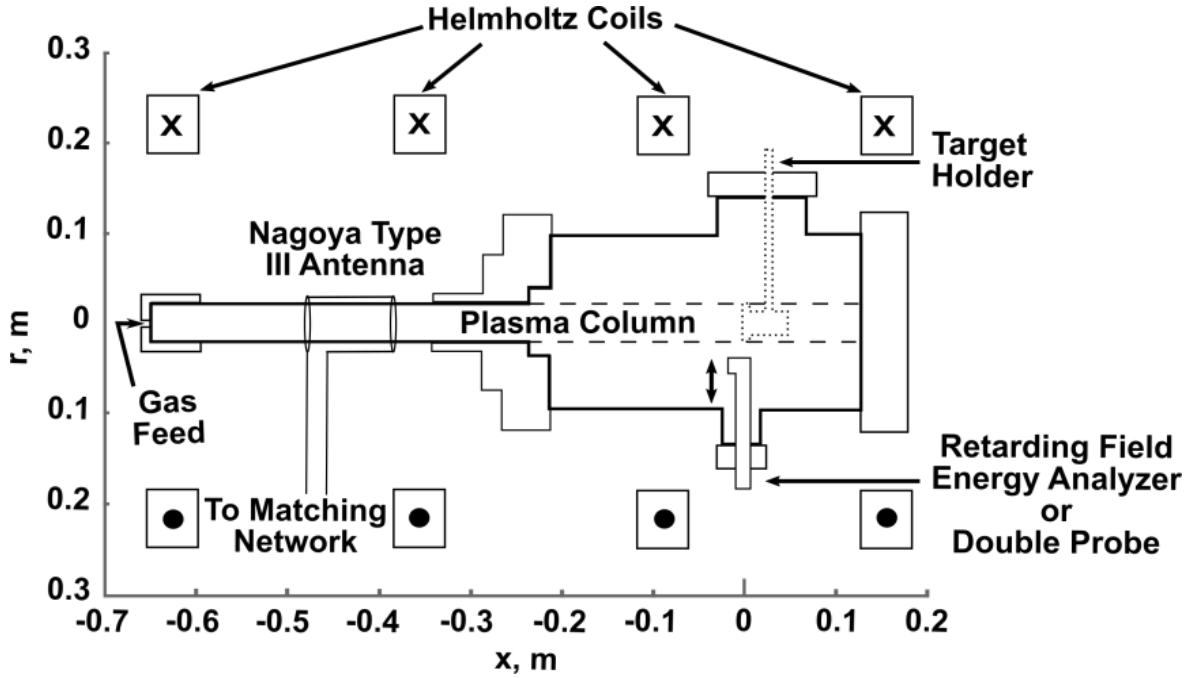

Figure 5-1| Schematic of the DIONISOS helicon plasma chamber.
The scale shows the axial location of the Nagoya type III antenna with respect to the location of the target holder, Langmuir probes, and retarding field energy analyzer.

Table 5-1| Summary of the conditions for the plasma discharges cases used in this study.

Parameter	H mode	W mode
Magnetic Field, T	0.046	0.077
Input Power, W	700	1000
Fill Pressure, Pa	3.8	3.8
Plasma density, 10^{17} m^{-3}	2.5	26
Electron Temperature, eV	4.8	4.8
Time-averaged plasma potential, $\langle \boldsymbol{V_p} \rangle$, V	26	18.9

5.2.1 Double Langmuir Probe

The DLP was made with 0.508 mm diameter soft stainless steel rods. The tips extended 1.0 mm away from individual alumina tubes and were separated by 1 mm, as shown schematically in Fig. 5-2. The DLP configuration was used to measure the plasma density and temperature to avoid mis interpreting the current-voltage (I-V) characteristic of an uncompensated single Langmuir probe in RF plasma. Although, RF rectification can lead to errors in DLP interpretation in low density RF plasma, high density plasma with large ratio of probe radius to Debye length are only weakly affected in the presence of RF sheaths [88]. DLP characteristics were evaluated using the equivalent resistance method [89,90]. For the equivalent resistance method, if the probe is operating in a thin sheath limit, which is valid when the Debye length,

$$\lambda_{\mathrm{D}} = \left(\frac{\varepsilon_0 k_{\mathrm{B}} T_{\mathrm{e}}}{e^2 n_{\mathrm{e}}}\right)^{1/2}, \tag{5.1}$$

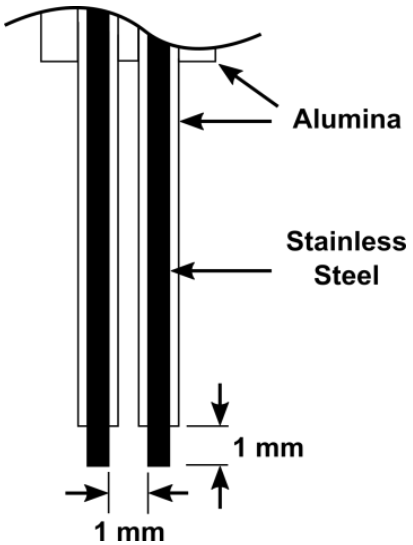

Figure 5-2 | Double Langmuir probe configuration used to measure the plasma density and electron temperature under the various plasma discharge conditions.

is small compared to the probe radius, r_p, where ε_0 is the permittivity of free space, k_B is Boltzmann's constant, and e is the charge of an electron, the ideal current between the probe tips, I, is related to the voltage between the probes, V, by the function,

$$I = A_p e n_e \left(\frac{k_B T_e}{2\pi m_i}\right)^{1/2} \tanh\left(\frac{eV}{2k_B T_e}\right), \tag{5.2}$$

where A_p is the surface area of one of the probe tips and m_i is the mass of the ion. Eqn. (5.2) is valid under the assumption that the ion gyro-radius is larger than the probe radius, which is satisfied here. By taking the first derivative of this function with respect to V and evaluating at $V = 0$,

$$\frac{dI}{dV}\Big|_{V=0} = \frac{eI_{i,sat}}{2k_B T_e}, \tag{5.3}$$

where $I_{i,sat}$ is the ion saturation current,

$$I_{i,sat} = A_p e n_e \left(\frac{k_B T_e}{m_i}\right)^{1/2}, \tag{5.4}$$

showing the electron temperature is equal to half of the voltage obtained when the linear fit to the origin of the DLP I-V characteristic is equal to the ion saturation current.

Experimental measurements often feature non-ideal DLP characteristics, so modifications to the equivalent resistance method go further to account for offsets in the inflection point of the characteristic and also for ion saturation currents that are proportional to the probe potential due to sheath expansion. The modified equivalent resistance method of Chang and Laframboise [90] gives the electron temperature as

$$k_B T_e = \frac{e\left(I_{i,pos} - I_{i,neg}\right)}{4\left(1.08\frac{dI}{dV}\Big|_{inf} - 0.79\frac{dI}{dV}\Big|_{i,sat}\right)}, \tag{5.5}$$

where $I_{i,pos}$ is the current intercept of the linear fit to the positive ion saturation region at the inflection point potential, $I_{i,neg}$ is the current intercept of the linear fit to the negative ion saturation region at the inflection point potential, $\frac{dI}{dV}\Big|_{inf}$ is the slope of the linear fit at the inflection point, and $\frac{dI}{dV}\Big|_{i,sat}$ is the slope of the linear fit to the ion saturation region. A detailed diagram of an example DLP characteristic and linear fits is shown in Fig. 5-3. Once the electron temperature is determined with Eqn. (5.5), the plasma density is calculated with Eqn. (5.4), with $I_{i,sat} = \left(I_{i,pos} - I_{i,neg}\right)/2$.

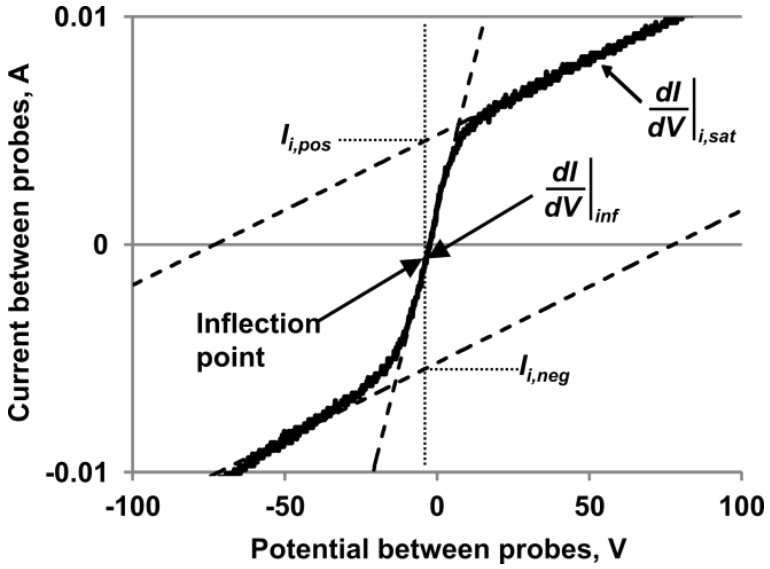

Figure 5-3 | Double Langmuir probe data analysis.
An example diagram of the double Langmuir probe I-V data along with the linear fits to the ion saturation regions and to the inflection point region. The values of the slopes and the current intercepts of the ion saturation fits at the inflection point potential are used to calculate the electron temperature and plasma density using Eqns. (5.4) and (5.5).

With the plasma density and electron temperature determined from the DLP characteristic, the Debye length was calculated and compared to the probe radius. For the measurements made in this thesis, the smallest ratio of the probe radius to the Debye length, r_P/λ_D, was the order of 1 for the E mode where the plasma density was typically 10^{16} m^{-3} or lower. For the H and W modes of interest in this thesis, the ratio was of the order of 10. Thus, the assumption that the DLP was operating in the thin sheath limit is valid for the investigation of the H and W mode and RF affects should be negligible.

5.2.2 Retarding Field Energy Analyzer

A conventional four-grid RFEA [91] was used to measure the IEDF at separate radial positions at the same axial position as the target holder. A diagram of the RFEA grid bias settings is shown in Fig. 5-4. The biasing scheme of the RFEA was chosen to minimize various artifacts that arise in RFEA I-V traces due to stray electrons [92]. The grid facing the plasma, Grid 1, was at the floating potential of the plasma so that the RFEA was analyzing neutral plasma. Then, the RFEA was used for ion collection by biasing Grid 2 negative with respect to the floating potential to shield out the plasma electrons energetic enough to overcome the potential barrier between the plasma potential and the floating potential. A voltage ramp was applied to Grid 3 to selectively repel the ions in the analyzer entering the RFEA. Grid 4 was biased negatively to repel secondary electrons generated at Grid 3 and at the collector plate from affecting the ion current measured on the Collector. Finally, the Collector was biased negatively to collect the ions transiting the RFEA. The current measured on the Collector as the retarding potential of Grid 3 is varied gives the amount of plasma ion flux that possesses an energy equal to or greater than the potential difference between the plasma and Grid 3.

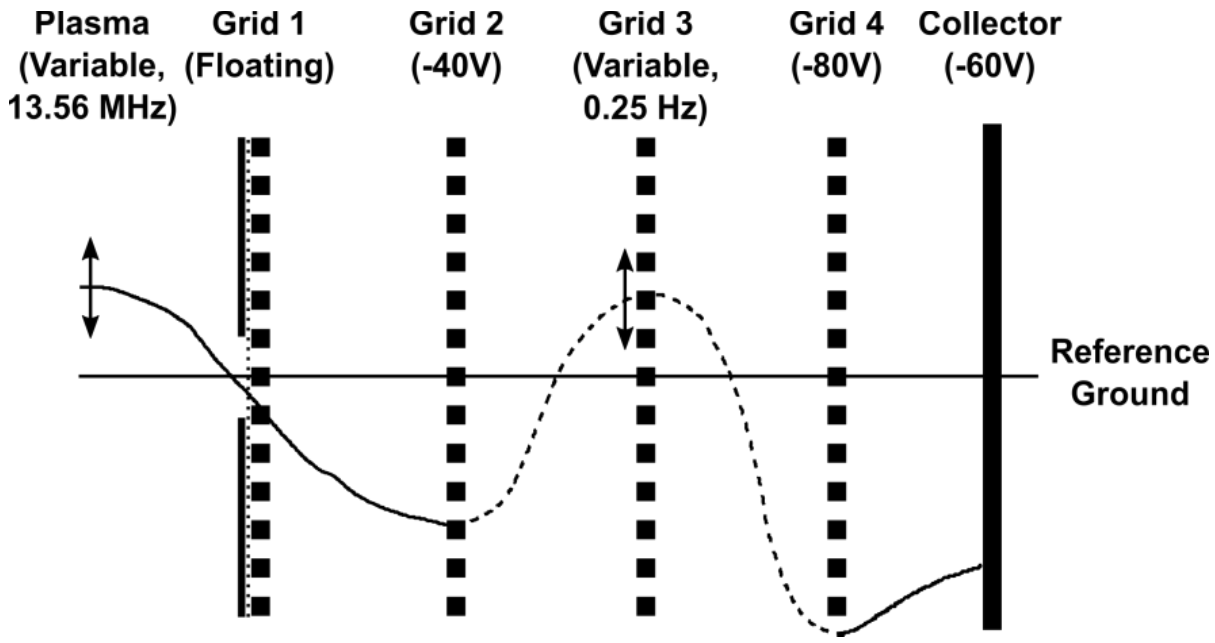

Figure 5-4 | Potential diagram in the RFEA for this study.
The grid aperture size is 152 μm and the space between the grids is 635 μm. The grids and collector plate are made from 127 μm thick stainless steel foil. Grid 1 was covered with a tungsten mesh with aperture size of 40 μm. Since the grid transmission coefficient is 0.26 and the entrance slit was limited to 500 μm, the grids were aligned during assembly to maximize the collector current signal.

The grid aperture size of the stainless steel grids of the RFEA was 152 μm. The smallest calculated Debye length in the plasmas examined was approximately 10 μm. Typically, the aperture size should be no bigger than twice the sheath thickness, so that the plasma is properly screened out of the analyzer. The thickness of the sheath can be approximated from the Child-Langmuir space-charge limited current density,

$$j_{\mathrm{SCL}} = \frac{4}{9}\varepsilon_0\sqrt{\frac{2e}{m_{\mathrm{i}}}}\frac{\left(V_{\mathrm{p}}-V_{\mathrm{G}}\right)^{3/2}}{{x_{\mathrm{s}}}^2}, \tag{5.6}$$

where j_{SCL} is the space-charge limited current density supplied by the plasma, $V_{\mathrm{p}} - V_{\mathrm{G}}$ is the potential difference in the sheath, and x_{s} is the sheath thickness. Taking the current density as that satisfied by the Bohm criterion,

$$j_{\mathrm{Bohm}} = n_{\mathrm{e}} e c_{\mathrm{s}}, \tag{5.7}$$

where c_{s} is the ion sound speed

$$c_{\mathrm{s}} = \left(\frac{k_{\mathrm{B}}T_{\mathrm{e}}}{m_{\mathrm{i}}}\right)^{1/2}. \tag{5.8}$$

Setting $j_{\mathrm{SCL}} = j_{\mathrm{Bohm}}$ and solving for x_{s} leads to an expression that gives the approximate sheath thickness in terms of the Debye length,

$$x_{\mathrm{s}}{}^2 = 0.63 \left(\frac{e(V_{\mathrm{p}} - V_{\mathrm{G}})}{k_{\mathrm{B}} T_{\mathrm{e}}}\right)^{3/2} \lambda_{\mathrm{D}}{}^2. \tag{5.9}$$

So, the sheath thickness with no external bias applied to Grid 1 is about 2 to 3 times larger than the Debye length. Then, the aperture diameter should be no larger than 4 to 6 times the Debye length to fully shield out the plasma from the RFEA. However, this criterion is not met by the floating grid for the highest density plasmas used in this study. The situation is alleviated in two ways by sheath expansion that occurs between Grid 1 and Grid 2. First, the grids have a transmission coefficient of 0.26, so the plasma density in the space between Grid 1 and Grid 2 is decreased by a factor of 4, assuming the plasma beamlets expand in the space between Grid 1 and 2. Decreasing the plasma density by a factor of 4 increases the Debye length by a factor of 2, doubling the sheath thickness. Second, the potential difference between Grid 1 and Grid 2 is approximately 40 V, which increases the sheath by another factor of 20 to 30 (see Eqn. (5.9)), depending on the electron temperature. Therefore, the plasma should be adequately shielded out of the rest of the RFEA by Grid 2. A fine tungsten mesh was placed over Grid 1. The aperture size of the 25 μm thick tungsten mesh was 40 μm, meeting the requirement for adequate shielding of the plasma from the RFEA. The stainless steel mesh then acted as a scaffold for the tungsten mesh. A slit with dimensions of 0.5 mm in the radial direction and 1 mm in the azimuthal direction with respect to the plasma device coordinate system was cut in molybdenum foil and placed over the tungsten mesh to hold it in place and to serve as the entrance slit to the RFEA.

The ion current collected by the RFEA at $r = 0$ for the W mode versus the retarding potential of Grid 3 is shown in Fig. 5-5a. The IEDF represented by the first derivative of the RFEA I-V characteristic is also shown as the dashed line in Fig. 5-5a. The ramp rate of the potential on Grid 3 was 0.25 Hz, which is much slower than fluctuations in the plasma potential. Periodic oscillations in the plasma potential result in a bimodal IEDF, since the potential spends more time in the vicinity of the maxima and minima. The peak separation is proportional to the peak-to-peak value of the plasma potential, if the oscillations are sinusoidal. As can be seen in Fig. 5-5a, the bimodal distribution is uneven, indicating the plasma potential waveform is not perfectly sinusoidal, and may be closer to a half-wave [93]. Also, the width of the rise on either side of the collector current derivative from zero to the peak is on the order of 5 V, which would indicate that the ion temperature would be on the order of 2.5 eV, which is unlikely for helicon plasma sources, which typically have ion temperatures less than 0.1 eV [94]. It is more likely that the resolution of the RFEA is on the order of 2.5 V. The IEDF is the convolution of the RFEA transfer function, which would be similar to a normal distribution with a full-width half-maximum of 2.5 V, and the time-averaged IEDF entering the RFEA from the plasma. The convolution elongates the minimum and maximum edges of the true IEDF, and decreases the separation of the peaks. This is shown as an example in Fig. 5-5b. Thus, the minimum and maximum energies of the IEDF from the measurement are taken as the half-widths of the minimum and maximum slopes, as annotated in Fig. 5-5a.

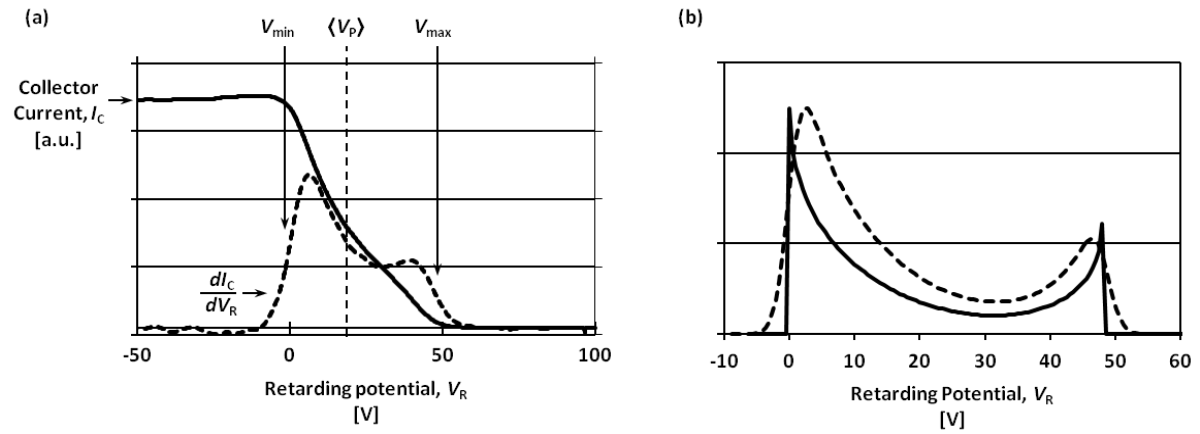

Figure 5-5 | Retarding field energy analyzer data analysis.
(a) Plots of the I-V characteristic measured on the collector of the RFEA positioned on the axis of the W mode (solid line) and its first derivative (dashed line), showing the IEDF at this location. (b) Plot of a theoretical time-averaged IEDF characteristic of a half-wave plasma potential modulation before entering the RFEA (solid line) and as measured on the RFEA collector (dashed line). The broadening due to the RFEA instrument was modeled as a normal function with a variance of 2.5 V.

The IEDF measured with the RFEA might not represent the local plasma potential and its oscillations due to several possible effects which are now examined. One possible mechanism that would give rise to lower energy peaks in the IEDF would be from collisions in the RFEA that would decrease the energy of ions entering the analyzer. However, the mean-free-path for charge exchange collisions between ions and neutral gas atoms is approximately 10^{-2} m for the neutral He gas pressure of 3.8 Pa, assuming the gas is at room temperature. The spacing between the grids of the RFEA is 6.35 x 10^{-4} m, so charge exchange collisions in the analyzer have a very low probability of occurring.

Another mechanism could be that ions lose parallel momentum and be lost when they collide with the structure of the RFEA. The loss of directivity of the ions would affect the magnitude of the upper potential peak, but would not necessarily give rise to a population of lower energy ions at a common energy, which is what is shown in the IEDF data. Even so, the ion collision time is considered for the H and W mode discharges. The ion collision time is inversely proportional to the energy of the ion, so the shortest ion collision time would be for the least energetic ions. The shortest ion collision time for 5 eV ions is on the order of 10^{-4} s. The average ion transit time through the sheath is given by Charles [43] as

$$\tau_{\mathrm{av}} \approx 1.2\sqrt{\frac{\varepsilon_0 m_{\mathrm{i}}}{n_{\mathrm{e}} e^2}}\left(\frac{2e(V_{\mathrm{p}}-V_{\mathrm{G}})}{k_{\mathrm{B}}T_{\mathrm{e}}}\right)^{1/4}. \tag{5.10}$$

The longest ion transit time would occur for the highest potential difference across the sheath over Grid 1, since the sheath thickness expands as the potential increases, as in Eqn. (5.9). For a test ion at 50 eV, with the electron temperature at 5 eV, the ion transit time across the sheath is 10^{-9} s. Therefore, the probability of momentum exchange collisions between ions is negligible.

Yet another possible mechanism that would distort RFEA results is that electron impact ionization could also occur in the vicinity of the RFEA entrance and also inside the RFEA from secondary electrons released from the grids or the collector. This would generate ions at various locations inside the RFEA with varying energies upon collection. The first ionization energy for He atoms is approximately 25 eV, which could be possible if the ion impact energies inside the RFEA are great enough. Assuming that the interior of the RFEA also has a neutral He gas pressure of 3.8 Pa, and taking the ionization cross section as 10^{-20} m^2, the ionization mean-free-path is 0.1 m, which is much larger than the RFEA.

An experimental validation of the RFEA in the W mode was conducted to ensure the reliability of the IEDF measurement. Grids 2-4 were removed so that there is only Grid 1 and the Collector operating in the RFEA. In this configuration, a DC bias is applied to Grid 1to screen out the plasma electrons while the potential on the Collector is swept. The secondary electrons generated in the RFEA are expelled out from Grid 1 when the Collector potential becomes more negative than the potential on Grid 1. A plot of the current intensity measured in the W mode on the Collector for various DC potentials applied to Grid 1 is shown in Fig. 5-6 at r = 4 mm. The shape of the bimodal IEDF hardly changes as the Grid 1 potential is varied. An additional peak in the IEDF at the Grid 1 potential is due to the secondary electrons that are lost from the RFEA as the Collector potential sweeps more negative than the Grid 1 potential. The peak is of the same sign as the ion current because the current of the secondary electrons leaving the RFEA are of the same sign as the current of ions entering the RFEA. As the potential on Grid 1 is made more negative, the ions from the plasma are entering the RFEA with much higher energy. This would have an effect on the measured IEDF if collisions or ionization were present at non-negligible levels. As can be seen from Fig. 5-6, the IEDF remains mostly the same at each Grid 1 setting.

The mechanisms that could "distort" the RFEA measurements are largely neglibilbe. Therefore, it is safe to assume that the bimodal IEDFs, represented by the current intensity as illustrated in Fig. 5-5, are representative of the real plasma potential oscillations. If the ion transit time through the sheath is longer than the RF period, the ion experiences an average potential that is dependent on the phase when the ion enters the sheath [43]. Averaging over the oscillating potential changes the IEDF by decreasing the separation of the two peaks in the distribution. As the ion transit time becomes much longer than the RF period, the ion would attain an energy more of on the order of the time-averaged plasma potential once it enters the RFEA. Therefore, to estimate the true extent of the plasma potential swing, the ion inertia effects in the RF sheath have to be addressed. The average ion transit time from Eqn. (5.1) multiplied by the frequency of the plasma potential oscillations, ω_{RF}, is a metric of the influence of the averaging effects from ion inertia. It is assumed that the plasma potential oscillation frequency is the same as the source antenna frequency, 13.56 MHz. If the oscillations in the plasma potential are sinusoidal, the ratio of the separation in potential of the peaks in the IEDF, $\Delta E = V_{\max} - V_{\min}$, to the energy equivalent of the peak-to-peak RF plasma potential is given [43] as

$$\frac{\Delta E}{eV_{pp}} = \left(1 + \left(\frac{\omega_{RF}.\tau_{av}}{2}\right)^2\right)^{-1/2}. \tag{5.11}$$

The values of $\omega_{RF}.\tau_{av}$ in the W modes studied here range from 0.86 to 0.99 and in the H modes, 0.92 to 0.98. Thus, if there were sinusoidal plasma potential oscillations, they would be shown in the IEDF measurement. Therefore, the potential difference between the peaks, or edges, in the IEDF, ΔE, is indicative of the presence and magnitude of plasma potential oscillations in the various modes of operation in the DIONISOS helicon plasma exposure chamber.

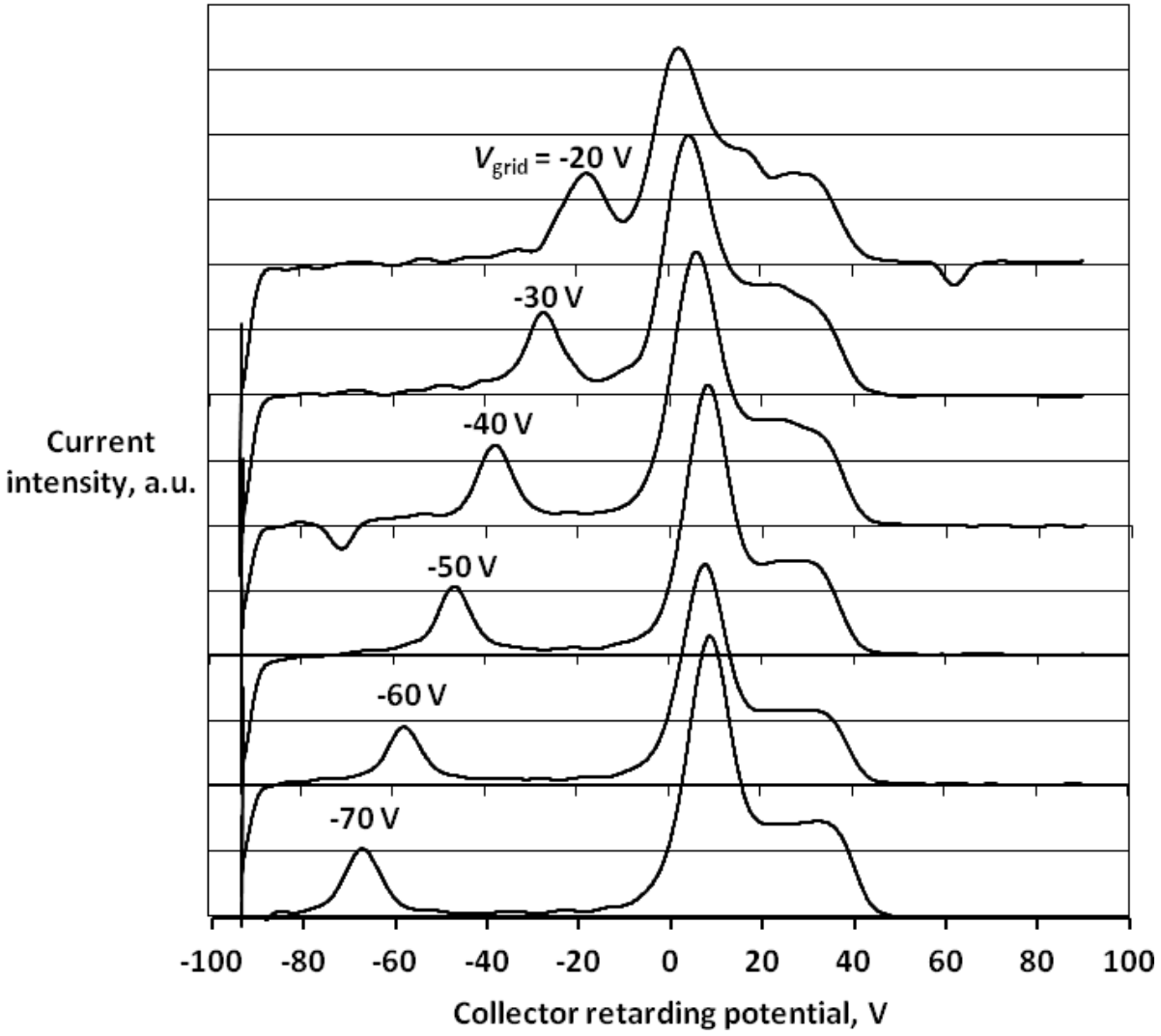

Figure 5-6 | Retarding field energy analyzer operation test.
Current intensity plots for the grid collector configuration of the RFEA where Grids 2-4 are removed. Different DC potentials are applied to Grid 1 and the current to the Collector is measured as the potential on the Collector is swept. The ion contribution of the current intensity does not change, while the secondary electron contribution changes with the Grid 1 potential setting.

5.3 Measurements of DIONISOS plasma discharge modes

5.3.1 Inductively- and wave-coupled mode profiles

The radial profiles of the plasma density and electron temperature measured from the DLP are shown in Fig. 5-7a and 5-7c for the model H and W mode, respectively. Note that the density scale is a factor of 10 lower for the H mode plot than for the W mode plot. The electron temperature for both discharges is very similar and is approximately 5 eV at $r = 0$ with a gradual taper to 3 eV at the edge of the plasma, $r = 22$ mm. The main difference between the H and W mode that is shown through the DLP is through the magnitude of the density. The density in the W mode is a factor of 10 larger than in the H mode. Also, the density gradient is an order of magnitude larger in the W mode than in the H mode. The highly peaked density profile is a signature of the W mode in helicon devices [82].

The changes in the IEDF with respect to radius for the H and W modes are shown in Fig. 5-7b and 5-7d, respectively. The contour plot depicts the current intensity, dI_C/dV_R, which represents the IEDF, with respect to retarding potential, V_R, and radius. The current intensity for Fig. 5-7b is a factor of 10 lower than for Fig. 5-7d. The current intensity plot for each radius was analyzed for the three potential values of V_{min}, V_{max}, and $\langle V_p \rangle$, as illustrated in Fig. 5-5a. The minimum and maximum potentials at each radius are connected by separate solid lines, while the average potential is shown as a cross for each radius. Unlike the density and electron temperature, the IEDF with respect to radius has vastly different behavior between the H and W modes. The current intensity for the W mode is bimodal at the center, with a minimum and maximum potential difference of 47 V at $r = 0$. The bimodal character of the IEDF continues out to a radius $r = 8$ mm, where the distribution suddenly shifts to a single peak. The width of the single peak is 6 V, which is close to the resolution of the RFEA, as discussed in section 5.2.3. For $r > 8$ mm, the width of the single peak increases until it becomes 30 V at $r = 18$ mm. The IEDF at each radius in the H mode has only one distinct peak. However, the width of the "peak" at $r = 0$ is very broad at 50 V. The width gradually decreases with increasing radius, until the width is 8.5 V at $r = 20$ mm.

A broad IEDF has been observed by Kim and Chang [83] in similar H mode discharges, in which they interpreted the IEDF as a single broad peak. The IEDF is still representative of plasma potential oscillations, but the peaks are not distinguishable. The new observation focused on here is that in the W mode discharge with He, the IEDF is clearly bimodal, with peak-to-peak potentials up to a factor of 2.5 greater than the time-averaged plasma potential for this model W mode, and varies with radius across the plasma. The restriction of the location of the bimodal IEDF to $r < 8$ mm coincides with the higher density, where the helicon dispersion relation can be satisfied for good wave coupling, and the maximum in the density gradient, which may set up a potential well to trap the helicon wave and enhance coupling, as for the radially localized helicon (RLH) mode [95].

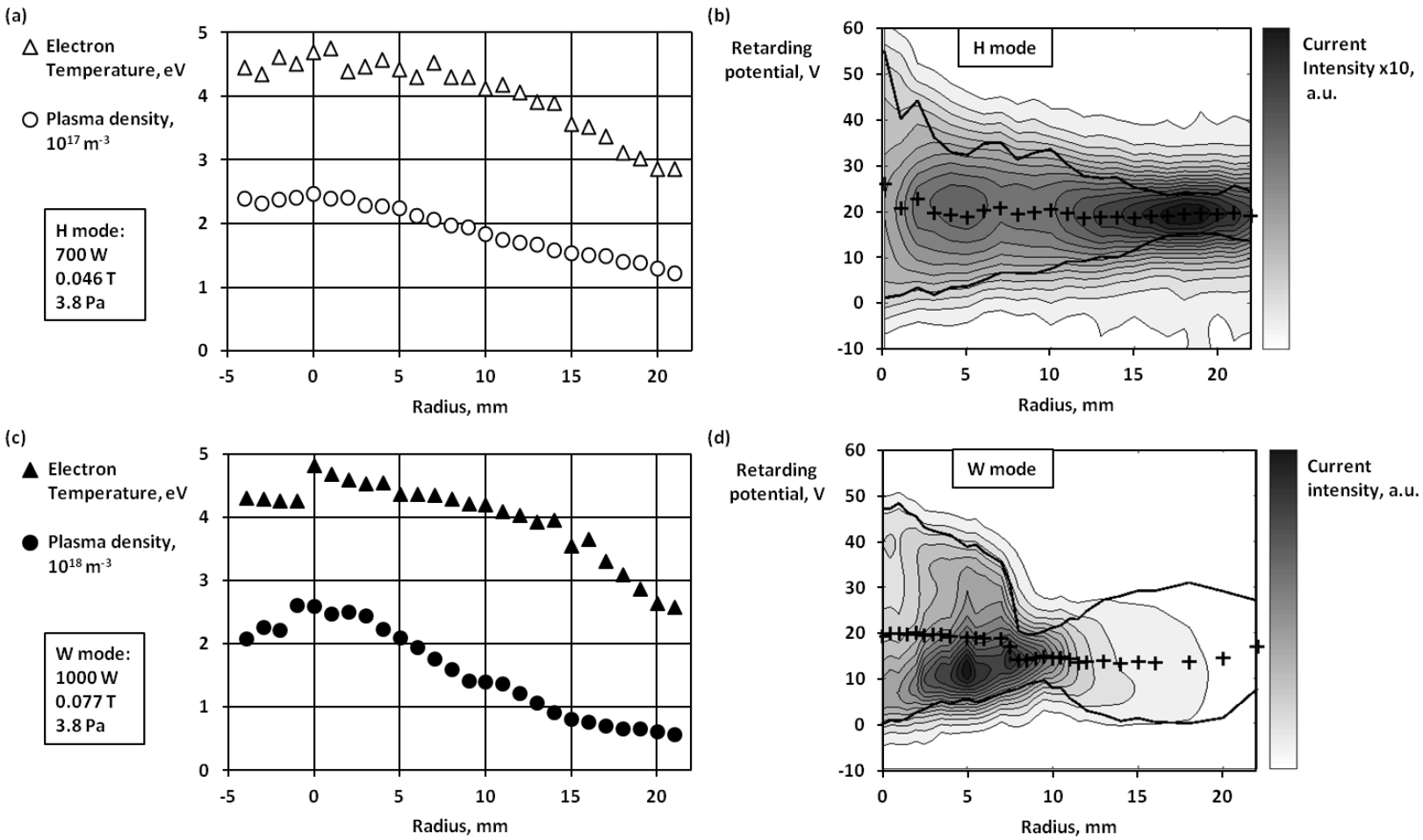

Figure 5-7 | Inductively- and wave-coupled discharge mode profiles.
(a) and (c) The plasma density (open circle, solid circle) and electron temperature (open triangle, solid triangle) profiles measured with a double Langmuir probe across the radius of the H and W mode, respectively, in helium with discharge conditions given in Table 5-1. (b) and (d) Contour plots of the current intensity with respect to retarding potential and radius in the H and W mode, respectively. The solid lines mark the minimum and maximum edges of the current intensity profile and the average plasma potential is shown as the cross points. The measurements were taken at an axial location 0.38 m from the end of the helicon antenna. The radius of a typical target and the helicon source quartz tube are 12.7 mm and 22 mm, respectively.

The variation in IEDF with radius in the W mode roughly coincides with the variation in surface morphology. A tungsten sample exposed to the W mode with a surface temperature of 1020 K and a DC bias of -50 V is shown in Fig. 5-8. The axis on the image is nominally aligned with the axis of the IEDF radial profiles. The black surface of the sample is the macroscopic view of tungsten fuzz; tungsten fuzz readily absorbs light. There is tungsten fuzz at larger radii on the sample. Near the center of the sample, where the sample appears bright, the sample is macroscopically reflective with dispersed growth of nano-tendril bundles and single nano-tendrils. Where there is a grey region, between r = 6 mm and r = 7 mm in the image, there is transition in surface morphology. The changes in surface morphology due to the radial variation in the IEDF will be explored in more detail in Chapter 6.

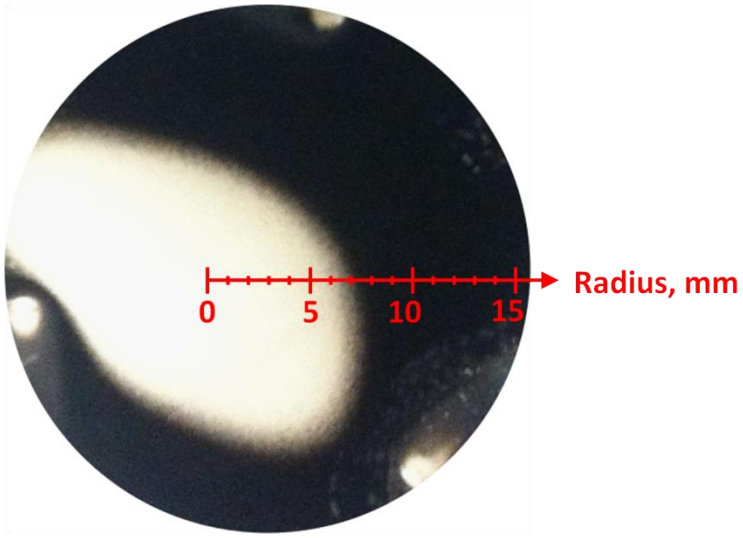

Figure 5-8 | Tungsten sample after exposure to the wave-coupled mode plasma.
The surface temperature was1020 K and the DC bias was -50 V. The axis is nominally aligned with the axis scanned by the RFEA in Fig. 5-7d.

5.3.2 Mode transitions with respect to magnetic field

It is well known empirically that the presence of H or W mode is affected in helicon sources by the axial magnetic field strength. The measurements made as the magnetic field is varied are shown in Fig. 5-9 for two values of input power, 700 W and 1000 W, and for the chamber fill pressure of 3.8 Pa. The electron temperature, shown in Fig. 5-9a, as well as the density, shown in Fig. 5-9c, change the most as the plasma is transitioning between modes. The transitions are accompanied by varied changes in the IEDF measurements, as well, shown in Fig. 5-9b and 5-9d for the 700 W and 1000 W case, respectively. The electron temperature decreases and the density increases the fastest for magnetic fields between 0.04 T and 0.06 T for both input powers. The width of the distributions, $\Delta E = V_{max} - V_{min}$, also decrease in this magnetic field interval. As is annotated in Fig. 5-9c, for magnetic fields lower than 0.04 T at 700 W, the plasma is in the low density E mode. In this mode, the plasma is tenuous enough for the fields of the antenna to penetrate the plasma. This is because the skin depth, δ, is large compared to the radius of the plasma, a. The skin depth, for $\omega_{RF} \ll \omega_{pe}$, is approximated [86] as

$$\delta \approx \frac{c}{\omega_{pe}} = \left(\frac{m_e}{\mu_0 n_e e^2}\right)^{1/2} \tag{5.12}$$

for a collisionless plasma, where c is the speed of light in vacuum, ω_{pe} is the electron plasma frequency, m_e is the electron mass, and μ_0 is the permeability of free space. As the magnetic field increases, so does the density, which means the skin depth decreases. Once the density reaches a value of approximately 2 x 10^{17} m^{-3}, the density no longer increases with increasing magnetic field. The skin depth, using Eqn. (5.12), corresponding to this plasma density is approximately 12 mm, while the plasma radius is 22 mm. This in agreement with the result of Kaeppelin *et al.* which showed that once the skin depth becomes about half of the plasma radius, the plasma mode has transitioned from a capacitively-coupled E mode to the inductively-coupled H mode [86].

The plasma density of the H mode at 700 W is identical to the density of the H mode at 1000 W, but the H mode exists at a much lower magnetic field for the higher input power case, shown in Fig. 5-9c. The electron temperature is slightly higher in the H mode for the higher input power case. As the magnetic field is increased with the input power at 1000 W, the electron temperature decreases, which is similar to the behavior shown for the E to H mode transition at 700 W. At 1000 W, when the magnetic field is greater than 0.07 T, the plasma transitions fully to the W mode. The new mode is clearly shown in Fig. 5-9d by the change in the IEDF to the bimodal distribution discussed in section IIC. The value of the density at the H to W mode transition is indicative of a transition to resonant wave-coupling. The dispersion for the RLH mode, derived by Breizman and Arefiev [95,96] by including radial variation in the cold plasma whistler wave dispersion, and subsequently verified with experiments [97,98], satisfies the relation,

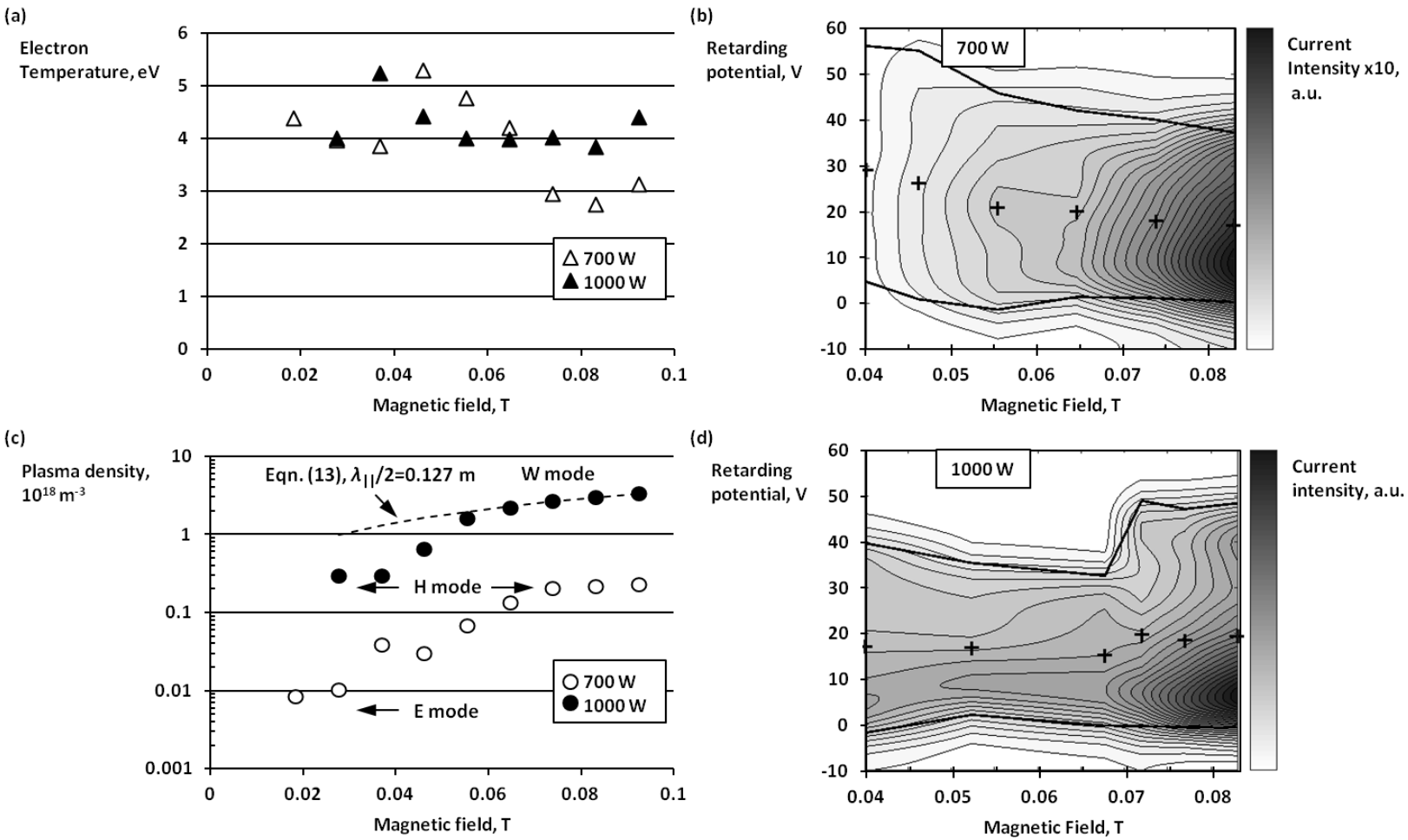

Figure 5-9 | Mode profiles with respect to magnetic field.
(a) The electron temperature and (c) plasma density measured at different magnitude fields with an input power of 700 W (open triangle, open circle) and 1000 W (solid triangle, solid circle). A fit to Eqn. (13) using the top four W mode data points is shown as the dashed line. Also shown are contour plots of the current intensity with respect to retarding potential and magnetic field for input powers of (b) 700 W and (d) 1000 W. The solid lines mark the minimum and maximum edges of the current intensity profile and the average plasma potential is shown as the cross points. The chamber fill pressure was 3.8 Pa for all measurements in these plots.

$$\omega \approx \omega_{ce} \frac{k_{\parallel}^2 c^2}{\omega_{pe}^2}, \tag{5.13}$$

where $k_{\parallel}$ is the wave number parallel to the background magnetic field and ω_{ce} is the electron cyclotron frequency. The frequency of the wave is approximately equal to the driving frequency of the antenna, 13.56 MHz, and the parallel wave number is dependent on the length of the antenna and the distance between the conducting boundaries. Thus, the dispersion relation for the RLH wave, Eqn. (5.13), couples the magnetic field, from ω_{ce}, to the density, through ω_{pe}. For parallel wave number $k_{\parallel} = \pi/l_a$, and the magnetic field 0.07 T, the plasma density that satisfies Eqn. (5.13) is 3.3 x 10^{18} m^{-3}, which is very close to the value measured with the DLP, 2.7 x 10^{18} m^{-3}. A fit to Eqn. (5.13) using the top four points of the experimental data of the density in the W mode in Fig. 5-9c results in a parallel wavelength of 0.127 m, while the antenna length is roughly 0.11 m. Also, as can be seen in Fig. 5-9c, the trend $n_e \propto B$ holds very well.

5.3.3 Mode characteristics with respect to input power

The measurements made as the input power is varied are shown in Fig. 5-10 for two values of magnetic field, 0.046 T and 0.077 T, and for the chamber fill pressure of 3.8 Pa. The mode transitions from E to H mode at 0.046 T and H to W mode at 0.077 T as the input power is increased are clear, shown by the electron temperature and plasma density in Fig. 5-10a and 5-10c, respectively. Again, during the mode transitions, the electron temperature decreases, and the density increases sharply. At 0.046 T, the E mode is characterized by low plasma density and large ΔE, shown in Fig. 5-10b. The wide IEDF at low input power is a characteristic of the capactively-coupled E mode in helicon plasma devices [84]. While the plasma is in the H mode, as the input power is increased, the density continues to increase and the potentials decrease.

At 0.077 T, the plasma transitions from H to W mode near an input power of 900 W, shown in the IEDF measurements in Fig. 5-10d. The potential difference between the two well-defined peaks in the bimodal IEDF for the W mode increases as the input power increases, without very much change in the density. The electron temperature also increases with increasing input power along with the increasing potentials. The increase in ΔE is much greater than the increase in electron temperature and $\langle V_p \rangle$. The density does not increase by very much in the W mode and the device geometry and magnetic field are fixed, so the density profile (i.e. the density gradient) does not change very much either. Upon measuring the radial variation in the W mode at 1200 W and 1400 W, it was found that the radius at which the distribution transitions from bimodal to a single peak was almost identical to the W mode at 1000 W, shown in Fig. 5-7d. Thus, once the plasma is in this W mode, with density more or less fixed by the dispersion relation Eqn. (5.13), the extra power that is absorbed increases the plasma potential. This indicates that it may be crucial to measure the IEDF in helicon plasma devices to fully understand the possible interactions the plasma will have with targets.

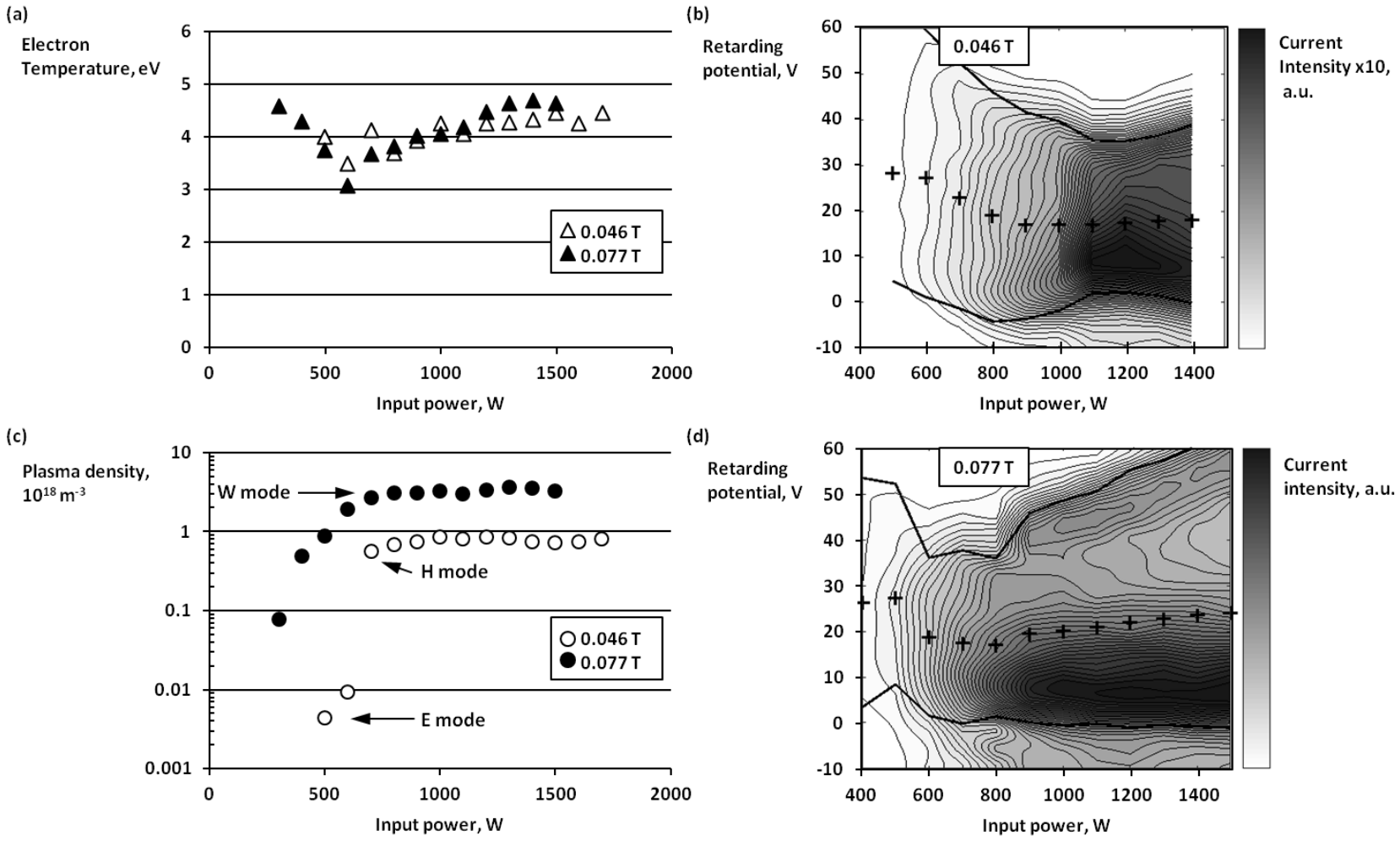

Figure 5-10 | Mode profiles with respect to input power.
(a) The electron temperature and (c) plasma density measured at different values of input power with a magnetic field of 0.046 T (open triangle, open circle) and 0.077 T (solid triangle, solid circle). Also shown are contour plots of the current intensity with respect to retarding potential and input power for magnetic fields of (b) 0.046 T and (d) 0.077 T. The solid lines mark the minimum and maximum edges of the current intensity profile and the average plasma potential is shown as the cross points. The chamber fill pressure was 3.8 Pa for all measurements in these plots.

5.3.4 Mode characteristics with respect to chamber pressure

Measurements made as the chamber pressure is varied are shown in Fig. 5-11 for the two combinations of magnetic field and input power used for the H and W modes listed in Table 5-1 and discussed in section 5.3.1. As the chamber pressure increases, or, similarly, as the collision frequency increases, the two modes have similar behavior in terms of electron temperature and density, shown in Fig. 5-11a and 5-11c, respectively. The electron-neutral collision frequency, ν_{en}, in He with a pressure of 3.8 Pa is approximately 60 MHz for an electron temperature of 4 eV [99], while the electron-ion collision frequency, ν_{ei}, is approximately 2 MHz and 11 MHz for plasma densities of 0.5×10^{18} m^{-3} and 2.5×10^{18} m^{-3}, respectively, and a Coulomb logarithm of $\ln\Lambda = 12$, assuming a Maxwellian electron distribution [100]. Power loss due to radiation from the excitation of neutral gas is proportional to the neutral gas pressure, resulting in lower power absorption in the plasma for fixed input power [96]. This might account for the decrease in plasma density and ΔE in the H mode, since $\nu_{en} >> \nu_{ei}$.

For the W mode, coulomb collisions are more frequent due to higher density, enabling wave coupling to the plasma. Although Coulomb collisions have been shown to dominate wave coupling [101,102], the wave absorption is competing against the radiative power loss. Also, even though the ionization rate is a small portion of the overall electron collision rate, it drops off precipitously as the electron temperature decreases [99]. The small decline in electron temperature seen in Fig. 5-11a means the ionization rate decreases, as well, which results in a lower plasma density. Also, as the chamber pressure increases, ΔE increases, shown in Fig. 5-11d. The increase in ΔE is a consequence of the decrease in plasma density, since the power to the ions is proportional to the product of the plasma density and the plasma potential [86,99]. The modest increase in plasma potential, even for a factor of 2 decrease in the plasma density, may be due to the shared power balance among the electrons, ions, and neutrals.

For chamber pressure greater than 6 Pa, the plasma transitions to a higher density W mode. This particular W mode is characterized by an IEDF that is narrow and appears to have one peak, shown in Fig. 5-11d. For resonant helicon modes, Caneses and Blackwell [102] show that the damping length is inversely proportional to the total collision frequency, $\nu_e = \nu_{en} + \nu_{ei}$. The collision frequency increases with increasing chamber pressure, even though the plasma density decreases, because the neutral collisions dominate over Coulomb collisions. The higher density W mode, may be due to more favorable coupling to a higher mode number wave for shorter damping lengths. For higher order modes, with shorter damping lengths, the wave number would be higher, and, according to Eqn. (5.13), the plasma density would be higher, for a fixed magnetic field. Though this is a qualitative explanation for the plasma behavior, a more detailed investigation of the power balance in the resonant W modes that exhibit the bimodal and "monoenergetic" IEDF is left for future work.

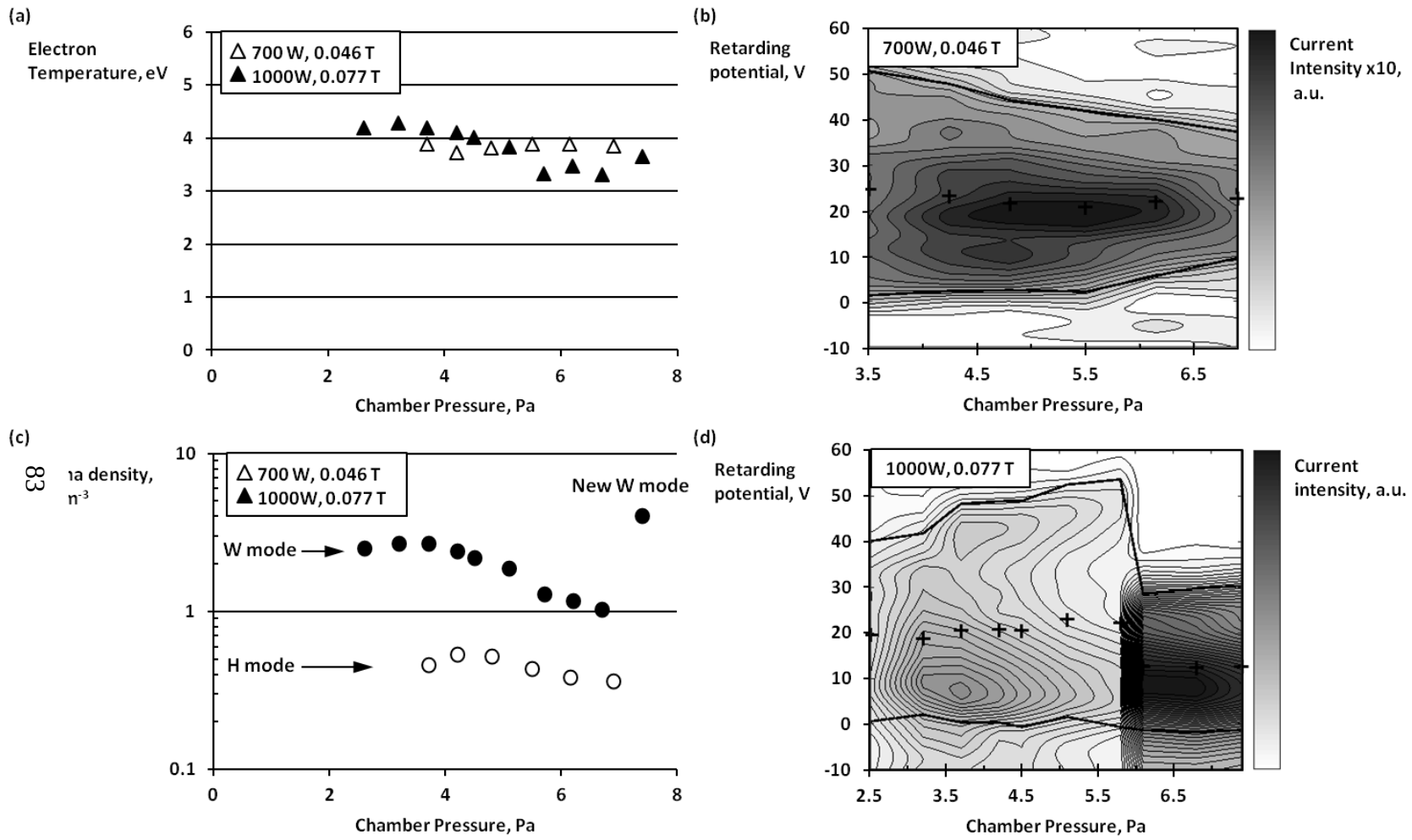

Figure 5-11 | Mode profiles with respect to chamber pressure.

(a) The electron temperature and (c) plasma density measured at different values of chamber fill pressures with a combination of input power and magnetic field of 700 W, 0.046 T (open triangle, open circle) and 1000 W, 0.077 T (solid triangle, solid circle). Also shown are contour plots of the current intensity with respect to retarding potential and chamber fill pressure for input power and magnetic field combinations of (b) 700 W, 0.046 T and (d) 1000W, 0.077 T. The solid lines mark the minimum and maximum edges of the current intensity profile and the average plasma potential is shown as the cross points.

5.4 Summary

The first thorough measurement of ion energy distributions in a helicon plasma source across the H and W mode of plasma operation have been obtained. The resonant helicon wave-coupled W mode of the DIONISOS plasma source exhibits plasma potential oscillations, shown by measurements made with a retarding field energy analyzer. The plasma potential oscillations vary radially in the plasma, with larger oscillation amplitudes on axis. The bimodal IEDF transitions to a "monoenergetic" IEDF at a radius r = 8 mm, while the inner radius of the quartz tube of the source is r = 22 mm. Discharge parameters were varied to study the behavior of the bimodal IEDF in the W mode. Radial variations in both the ion energy distribution and the ion flux density make the W mode of the helicon source challenging to work with for plasma-surface interaction research. However, once these properties are understood, the radial variation can provide a means to study multiple irradiation conditions in a single exposure, if the surface analysis diagnostic used can achieve spatial resolution that is much less than the characteristic change in the plasma behavior. Therefore this work provides key new insights to understand plasma-material interactions in helicon-source linear plasma devices, while also providing a new tool to understand oscillatory incident ion energy for surface effects. Since most fusion reactor designs use RF heating sources that couple through the boundary plasma, this also points to the need to understand RF-driven modifications to ion energy distributions in confinement devices.

The intrinsic variation in the IEDF with radius in the W mode roughly coincides with the variation in surface morphology with radius that forms on tungsten samples exposed to the W mode plasma. The correlation of the tungsten fuzz suppression and nano-tendril bundle growth with the large amplitude ion energy modulation is investigated further in the next chapter.

6 Cornucopia of nano-tendril surface morphology on tungsten surfaces exposed to radiofrequency helium plamsa

In this chapter, the DIONISOS experiment was used to study the impact of 13.56 MHz frequency RF helium (He) plasma on the surface morphology of tungsten (W). Helium ion energy distributions with a span of 70-75 eV, while still below the sputtering threshold result in nano-tendril bundles (NTBs) and free-standing W whiskers on surfaces at 1020 K. The NTBs are distributed intragranularly with coverage of less than 10% while reaching up to 30 microns height normal to the surface for He ion fluence of 7.6×10^{25} m^{-2} and flux density of 10^{22} $m^{-2} \cdot s^{-1}$. Analysis of the NTB interior and sub-surface structure is provided through focused ion beam cross section.

Observing how the surface morphology changes under RF conditions provides new experimental evidence that strongly supports the suggestion that the combination of He ion bombardment and bubble agglomeration result in adatom/ surface defect diffusion and surface roughening that are the basis for the development of nano-tendrils. By temporal modulation of the incident He ion energy, and manipulation of the surface defect kinetics, a new and diverse set of nanostructure types are found which clearly reveal that surface kinetics govern the formation of the tendrils. By varying the exposure conditions with these new experimental tools, different structures such as corrugations, isolated nano-tendrils, nano-tendril bundles (NTBs), and fuzz (Fig. 6-1) develop. Each type of nanostructure provides information pertaining to the nature of the surface morphology changes.

The complex structures and growth environment make it difficult to determine with direct experimental observation the driving mechanisms of nano-tendril growth. The premise of this chapter is to show through mutually supportive evidence that the nature of nano-tendril growth lies in the He ion-induced surface kinetics and adatom migration influenced by the stresses induced by He bubble growth within the material. The grain orientation, which affects the surface diffusivity, is shown to factor into the resulting surface morphology in the transition region where the character of the ion energy distribution function (IEDF) changes from bimodal to "monoenergetic," as shown in Chapter 5. Also, the corrugation pattern wavelength, observed prior to fuzz growth and coincident with NTB growth, is analyzed with a topographic instability model.

The isolated NTB growth due to ion energy modulation was presented at the 22nd International Conference on Plasma Surface Interactions in Controlled Fusion Devices and will be published in the journal Nuclear Materials and Energy [87].

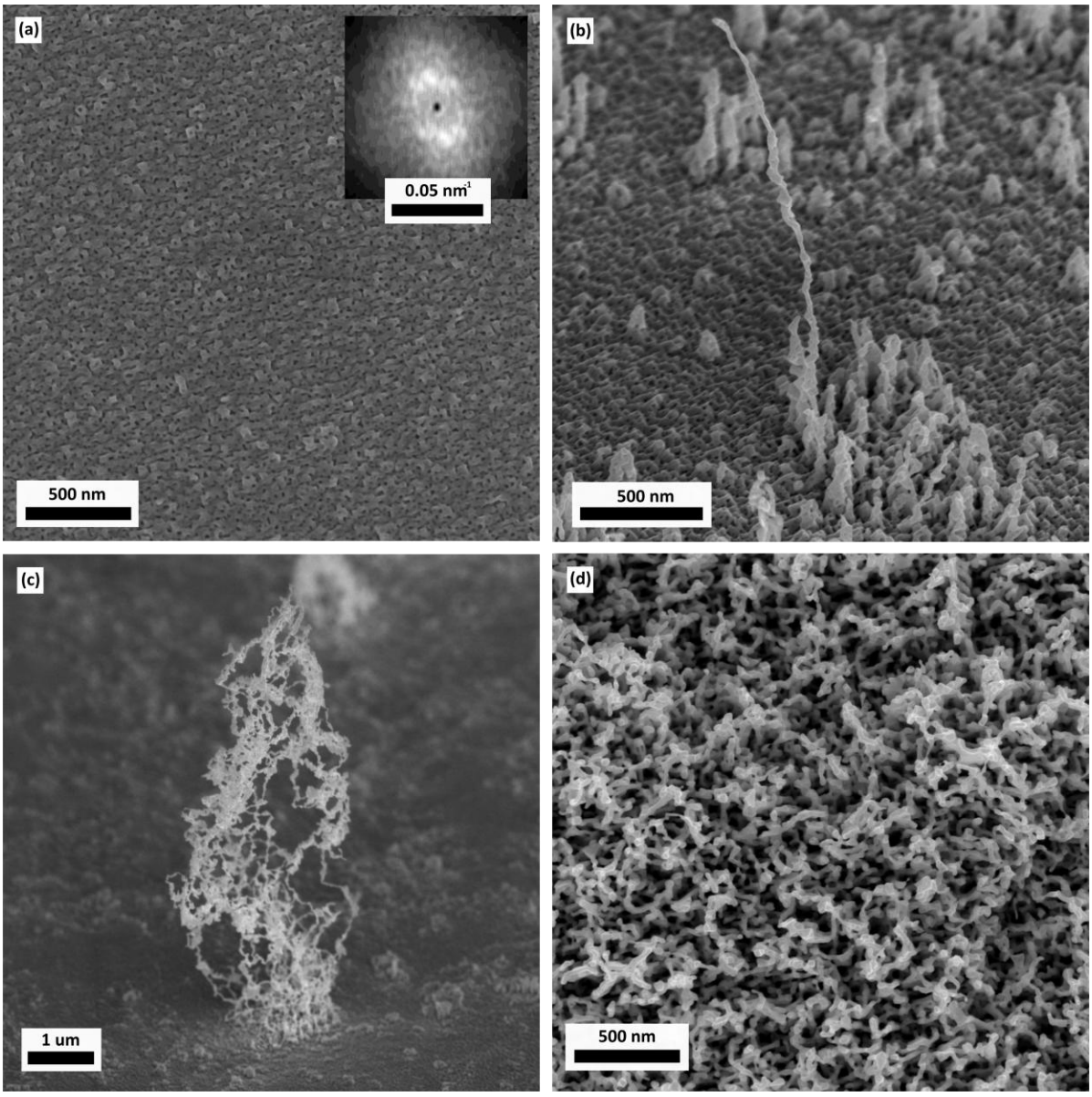

Figure 6-1 | SEM images of varieties of nanostructures due to modulation of helium bombardment energy on polycrystalline tungsten at different surface temperatures.

(a) Surface corrugations that have a characteristic wave number vector as represented by the 2D Fast Fourier Transform (image inset), with white as maximum and black as zero. The DC value at the center of the FFT is blocked to enhance the off center peaks in the distribution. The W sample was exposed with a surface temperature of 1020 K and He flux density of 4.5 x 10^{21} $m^{-2} \cdot s^{-1}$ to a He fluence of 5.8 x 10^{25} m^{-2}. The time-averaged He ion energy was 48 eV with modulation amplitude of +/- 22 eV at a frequency of 13.56 MHz. (b) Image of an isolated nano-tendril with the tip 2.2 μm above the surface and 20 nm thick at the tip to 117 nm thick at the base. (c) Image of a nano-tendril bundle (NTB) that is 2.9 μm wide and 8.3 μm tall normal to the surface. The individual tendril thickness in the NTB ranges from 20 to 60 nm. The (a) corrugations, (b) isolated nano-tendril, and (c) NTB were observed on the same sample, but on separate grains. (d) Image of a standard, quasi-uniform fuzz layer with an average depth of 0.95 μm. The individual tendrils of the fuzz layer are 20 nm thick. The growth conditions for the layer of fuzz are identical to (a), (b), and (c) but with a constant ion energy of 45 eV, i.e. with no applied energy modulation at 13.56 MHz. Images (a) and (d) were taken with the electron beam normal to the surface, while images (b) and (c) were taken with the sample normal tilted 52° from the electron beam . The typical grain size for these W samples is ~10-100 μm.

6.1 Bias modification

The samples used were 99.95% pure W disks with a diameter of 25.4 mm and a thickness of 1 mm. The surface to be exposed to the plasma was first mechanically polished and then electropolished in a 4% solution of sodium hydroxide (NaOH) kept at 0°C in a 1 L stainless steel vessel, which also served as the cathode in the electropolish circuit. The W sample was placed in a PTFE block with the edges of the sample sealed with high vacuum silicone grease such that the only exposed area of the anodic side of the electropolish circuit in the NaOH solution was the polished side of the W sample. The best electropolishing conditions were found to be with a voltage of 7 V applied to the W sample and limiting the current to 0.7 A, resulting in a current density of 0.14 $A \cdot cm^{-2}$.

The samples are either mounted to a ceramic heater stage for high temperature exposures or to a water-cooled stage for low temperature exposures. The temperature is feedback controlled for the high temperature exposures with a type K thermocouple mounted in the ceramic heater. The surface temperature was monitored with an infrared (IR) pyrometer at a fixed spectral wavelength of 1.6 μm assuming an emissivity of 0.3. Since the growth of nano-tendrils and fuzz on the surface changes the emissivity, the heater thermocouple was used as a measure of the sample temperature for the high temperature exposures when the surface morphology is expected to change. At the flux densities and ion energies used in this thesis, and with the maximum water cooling capacity of the cooled sample holder, the lowest temperature achieved was 530 K as measured by the IR pyrometer. The low temperature exposures do not have nano-tendril growth, so the pyrometer temperature reading was used to measure the sample temperature in the low temperature exposures.

A bias tee was fabricated that would allow a high frequency (13.56 MHz) potential modulation to be applied to the sample simultaneously with the DC bias. The resulting potential waveforms at the sample and on the atmospheric side of the bias feedthrough were checked with a high frequency probe. It was found that there were minimal losses through the transmission line to the sample. The high frequency probe attached to the feedthrough was then used to monitor the sample potential waveform during plasma exposure. The DIONISOS helicon plasma exposure chamber is shown schematically in Fig. 6-2.

6.2 Ion energy modulation effects

Helicon plasma sources exhibit multiple distinct modes of operation depending on the magnetic field, input power, and neutral gas pressure, as shown in Chapter 5. For this chapter, a helicon wave-coupled mode and an inductively-coupled mode were used. The helicon mode was generated with a magnetic field of 0.083 T, input power of 1000 W, and a background He gas pressure of 4 Pa. The inductive mode was generated with a magnetic field of 0.05 T, input power of 700 W, and background He gas pressure of 4 Pa. The flux density and electron temperature radial profile for the two plasma modes are shown in Fig. 6-3, determined from a double Langmuir probe. The plasma flux density was derived from the ion saturation current to a Langmuir probe that could be positioned at different radial locations in the plasma. The plasma flux density of the helicon wave-coupled mode of DIONISOS is peaked on axis, as is the plasma potential modulation. Thus, the ion-induced

effects are different from the center to the edge along the radius of a single sample. The flux density of He ions at the center of the plasma is twice that of the edge, with a nearly linear dependence between the center and the edge. The effect of the flux density gradient on the surface morphology is negligible in this flux density range, since the flux density gradient scale length is of the order of tens of millimeters, while diffusion lengths are tens of nanometers at the temperatures used. Therefore, the differences in the final surface morphology across the radius of the sample are due to the changes in the ion energy modulation at different flux densities.

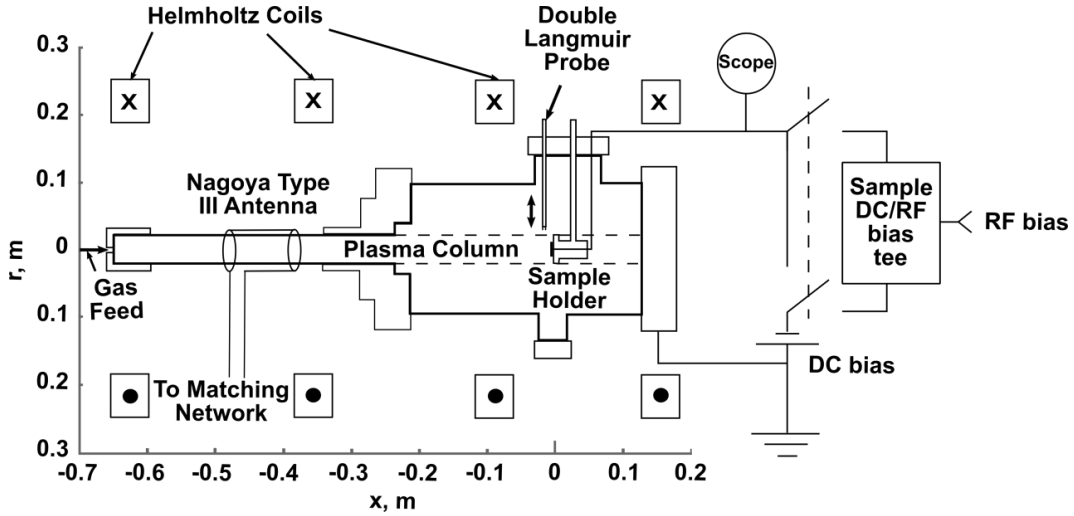

Figure 6-2 | Schematic of the DIONISOS plasma exposure chamber with bias modification.
The DC/RF biasing circuit allows for both DC and RF components of the sample bias to be controlled independently.

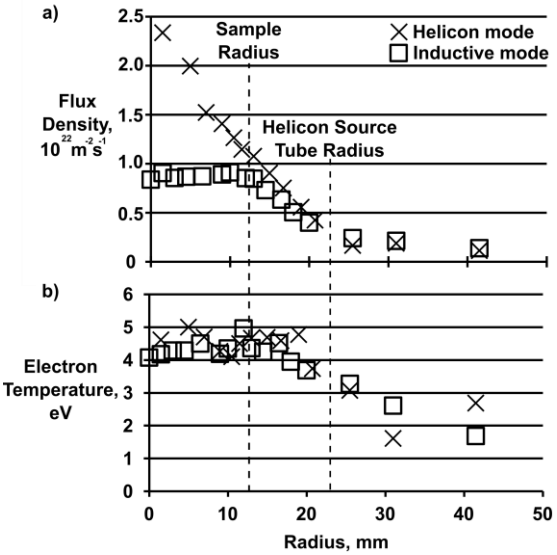

Figure 6-3 | Plasma flux density and electron temperature profiles.
(a) He ion flux density and (b) electron temperature radial profiles for the helicon mode (x) and the inductive mode (□). Measured with a double Langmuir probe located at x = -0.01 m in Fig. 8-1. The sample surface is at x = 0 m.

6.2.1 Single grid-collector retarding field energy analyzer

The ion energy distribution function (IEDF) incident on the targets was analyzed by constructing a single grid-collector retarding field energy analyzer (RFEA) in place of the sample, as in Chapter 4. The grid is a W mesh with a transmission factor of 0.56 mounted on a molybdenum foil with an entrance aperture at the center that is 1 mm by 1 mm. The hole size of the grid, 40 μm, is of the order of 3-4 Debye lengths in these plasmas (λ_D = 10-15 μm). Since the grid holes are larger than twice the Debye length, degradation of the energy resolution of the RFEA due to curvature of the potential around the grid bars is expected [92]. However, sheath expansion due to the negative bias applied to the grid alleviates this effect. Thus, the grid effectively mimics the conditions present when there is a target mounted on the target holder. The final ion energy resolution is estimated to be $\Delta E \sim 5$ eV. The space between the grid and the collector was 380 μm, while the ionization mean free path is on the order of 1 cm, so there should be no ionization within the drift space between the grid and the collector. Also, the drift space is narrow enough to avoid space charge effects. To use this grid-collector set up to measure the IEDF incident on a target, the grid was biased with -50 V, swept the voltage on the collector from -100 V to 100 V, and measured the current to the collector simultaneously.

Though simple to implement and compact, the single grid-collector RFEA requires additional considerations of the contribution from secondary electrons to the collector current. The ion current to the collector is the same polarity as secondary electron current leaving the collector. As the collector potential is swept, the current to the collector shows two levels of saturation. The highest level of saturation occurs when the collector potential is lower than the grid bias, as seen in Fig. 6-4a for the RFEA used to measure the IEDF in the inductive mode plasma. The net current collected saturates when the collector potential is below the grid bias because the secondary electron emission from the collector is lost from the analyzer to the plasma. When the collector potential sweeps above the grid bias, the secondary electrons from the collector are effectively suppressed. A second level of saturation is observed in this potential region where the secondary electrons are suppressed and the collector potential is still below the lowest energy ions, so all of the ion current available is collected. The collector current decreases again once the collector potential is high enough to repel the lowest energy ions.

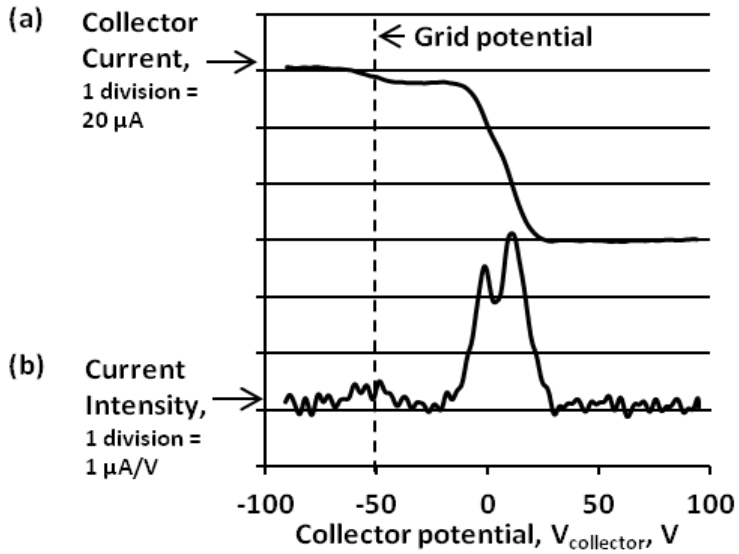

Figure 6-4 | Grid-collector retarding field energy analyzer data analysis.
(a) Collector current measured through a grid biased at -50 V as the collector potential is swept from -100 V to 100 V at the center of the inductive mode plasma. (b) Current intensity, or the derivative of the collector current with respect to the collector potential in (a). The current intensity is proportional to the ion energy distribution function passing through the grid.

The current intensity on the collector, shown in Fig. 6-4b, is the derivative of the measured collector current versus the collector potential, and is proportional to the local IEDF in the plasma after passing through the sheath and the biased grid. Since the collector potential sweep rate, 0.25 Hz, is much slower than the fluctuations in the plasma or sheath, 13.56 MHz, the current intensity represents the time-averaged IEDF incident on the target at the center of the plasma convolved with the transfer function of the RFEA, which is assumed to be a Gaussian function with a variance of 5 eV and an unknown normalization. However, the shape of the IEDF, not the magnitude, is important here. As can be seen in Fig. 6-5a, the IEDF at the center of the helicon mode is a broad, bimodal distribution from 25 eV to 100 eV with two dominant peaks in the distribution separated by approximately 50 eV. The bimodal IEDF in the helicon mode is naturally occurring as was shown in Chapter 5. In short, the time-averaged IEDF in helicon sources can be broadened due to RF modulation of the plasma potential [83].

To isolate the effect of RF broadening or time modulation of the plasma potential in the resulting surface morphology in the helicon mode, the effect of an RF bias on the sample was tested with the plasma in the inductive mode, which has less RF pickup from the antenna and a naturally more narrow IEDF [84]. The IEDF measured at the center of the inductive mode is shown in Fig. 6-5b; little broadening is present in the IEDF. To make a baseline comparison to W fuzz growth, a W sample was subjected at 1020 K with a DC bias of -50 V to the inductive mode for a He fluence of 5.8×10^{25} m^{-2} and W fuzz formation was the result, shown in Fig. 6-6. To impose similar RF broadening in the time-averaged IEDF incident on the sample as found naturally in the helicon mode, a bias tee circuit was constructed so that an RF potential could be used to modulate the DC bias to the sample, shown schematically in

Fig. 6-2. The input power from the RF bias supply was selected so that the peak-to-peak value of the modulated sample bias was comparable to the peak-to-peak value of the bimodal IEDF measured in the helicon mode, approximately 50 V peak-to-peak (Fig. 6-5a and 6-5c). Obtaining this spectrum required 1-2 W of RF power. The voltage waveform, from which the peak-to-peak potential was measured, was monitored with a high frequency voltage probe on the bias feedthrough into the plasma chamber. The resulting IEDF measured through the grid with the RF modulated bias in the inductive mode, shown in Fig. 6-5c, is bimodal with similar FWHM and peak-to-peak potential as the IEDF measured at the center of the helicon mode, Fig. 6-5a. The exposure conditions are summarized in Table 6-1.

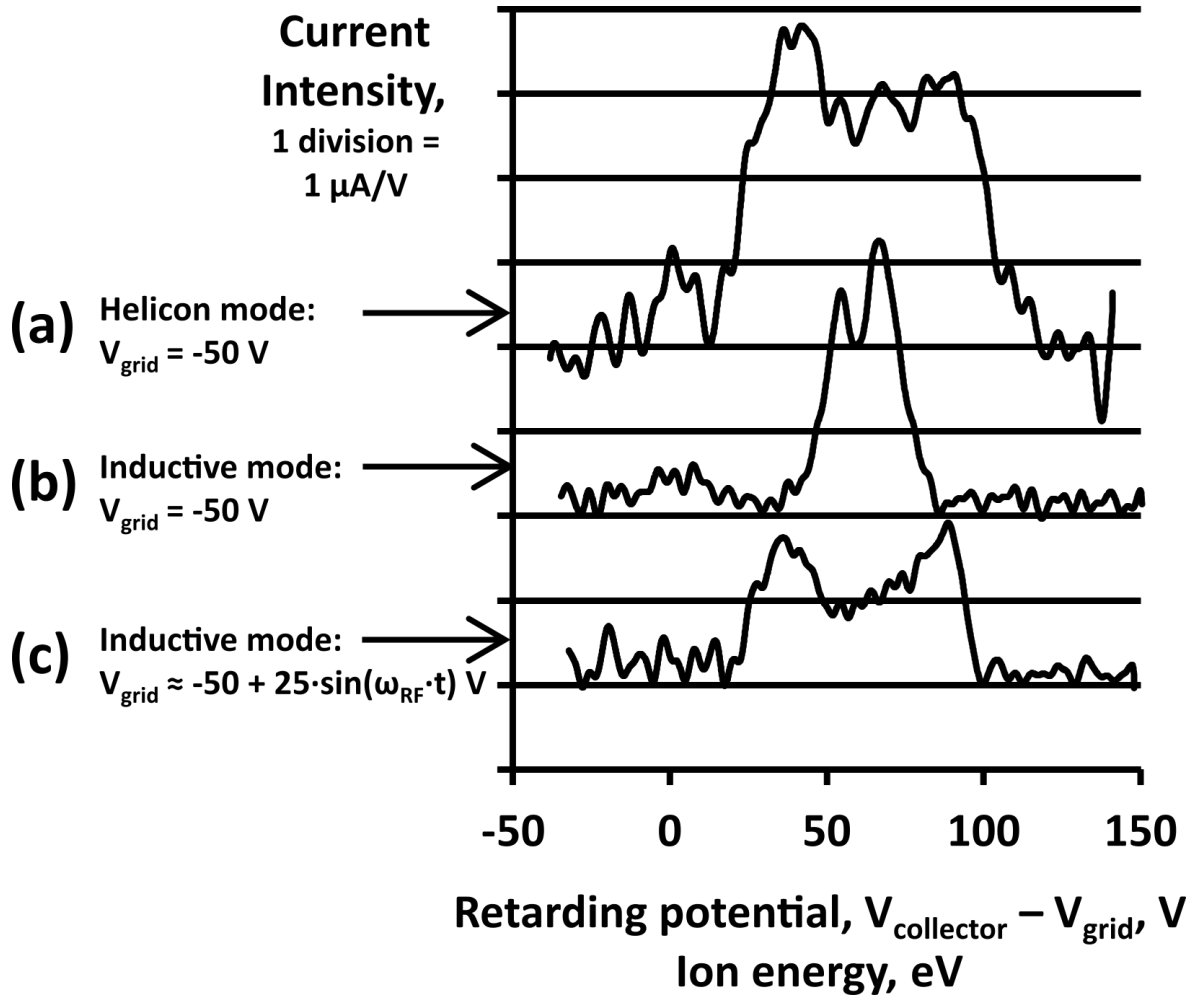

Figure 6-5 | Ion energy distribution functions.
(a) Time-averaged ion energy distribution function (IEDF) measured on axis in the helicon mode through the grid with -50 V DC bias. (b) IEDF measured on axis in the inductive mode through the grid with -50 V DC bias. (c) IEDF measured on axis for the same inductive mode as in (b) but with a -50 V DC bias modulated with 1 W of RF power at 13.56 MHz resulting in modulation at +/- 25 V.

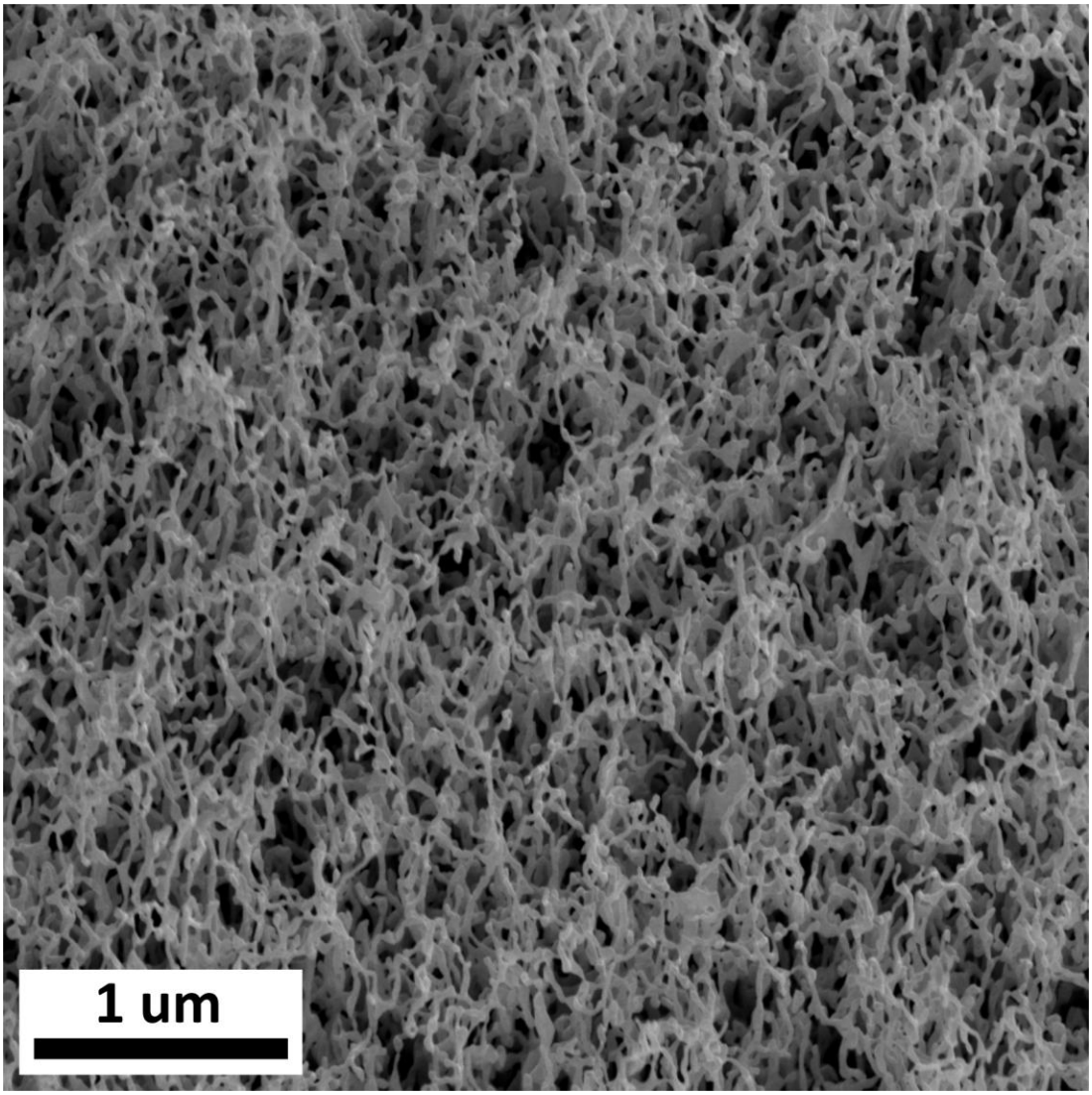

Figure 6-6 | Tungsten fuzz
Scanning electron micrograph of W fuzz grown on a sample at 1020 K in the inductive mode plasma with a DC bias of -50 V for a He fluence of 5.8 x 10^{25} m^{-2}. The local ion energy distribution is shown in Fig. 6-5b. The thickness of the W fuzz layer was measured to be 1.5 μm. The viewing angle is 52° from the sample normal.

Table 6-1 | Exposure conditions

		Helicon Mode V_{bias} = -50 V	Inductive Mode V_{bias} = -50 V	Inductive Mode $V_{bias} = -50 + 25 \cdot \sin(\omega_{RF} \cdot t)$ V
Input power,	W	1000	700	700
Magnetic field,	T	0.083	0.050	0.050
Fill pressure,	Pa	4	4	4
Peak flux density,	10^{22} $m^{-2} \cdot s^{-1}$	2.5	0.9	0.9
Exposure fluence,	10^{25} m^{-2}	7.6	5.8	5.8
Electron temperature,	eV	4.5	4	4
Average ion energy,	eV	63	56	54
IEDF FWHM,	eV	75	24	71

6.2.2 Induced ion energy modulation produces nano-tendril bundles

The NTB structures, shown in Fig. 6-7a and 6-7b, were observed after a W sample with a surface temperature of 1020 K and DC bias of -50 V was exposed to the helicon mode of DIONISOS. The local He fluence at the location where the SEM images were taken (Fig. 6-7a and 6-7b) is estimated to be 7.6 x 10^{25} m^{-2}. A layer of fuzz with a gradient in layer thickness might be expected due to the gradient in the flux density measured in the helicon mode, Fig. 6-3a. However, at the center of the sample, which has a broad, bimodal IEDF as shown in Fig. 6-5a, the macroscopic reflectivity of the sample remained relatively unchanged. Higher resolution imaging with a scanning electron microscope (SEM) revealed that the reflective area of the sample had nano-tendril growth, but in the form of NTBs. The area remained mostly reflective due to the low coverage (<10%) of the NTB structures, as seen in Fig. 6-7a, and the relative smoothness of the surrounding area.

To confirm that the broad, bimodal IEDF is the reason for the NTB growth that forms instead of fuzz using the helicon mode plasma, RF modulated bias was applied to a W sample at 1020 K and subjected the sample to the inductive mode for the same amount of total collected charge as the W fuzz sample exposed with only a DC bias to the inductive mode, or the equivalent of a He fluence of 5.8 x 10^{25} m^{-2}. The sample remained macroscopically reflective, except for near the edges of the sample and near the mounting clips. The surface morphology of the outer radii of the sample and under the clip hardware was W fuzz. Microscopic inspection revealed NTB growth in the reflective area, as seen in Fig. 6-7d, but the NTBs were smaller than those grown in the higher flux density helicon mode. Also, some grains contained a spread of single nano-tendrils growing 2 μm perpendicular to the surface, shown in Fig. 6-7e and 6-7f. Therefore, the RF modulation of the ion energy is integral to the transition from W fuzz to NTB growth. The difference in size between the NTBs from the plasma born RF modulation and the sample bias RF modulation is likely due to the difference in flux density in the two exposures. The inductive mode has a flux density at the center a factor of three less than the helicon mode. The growth of W fuzz has been shown to have a flux density dependence, but saturates after a certain flux density level is reached and the saturation that could also be dependent on the ion energy and surface temperature [23]. In the present case, the NTB width and height from the surface also increases with increased flux density. The dependence of the NTB growth on varying the exposure parameters will be discussed in Chapter 7.

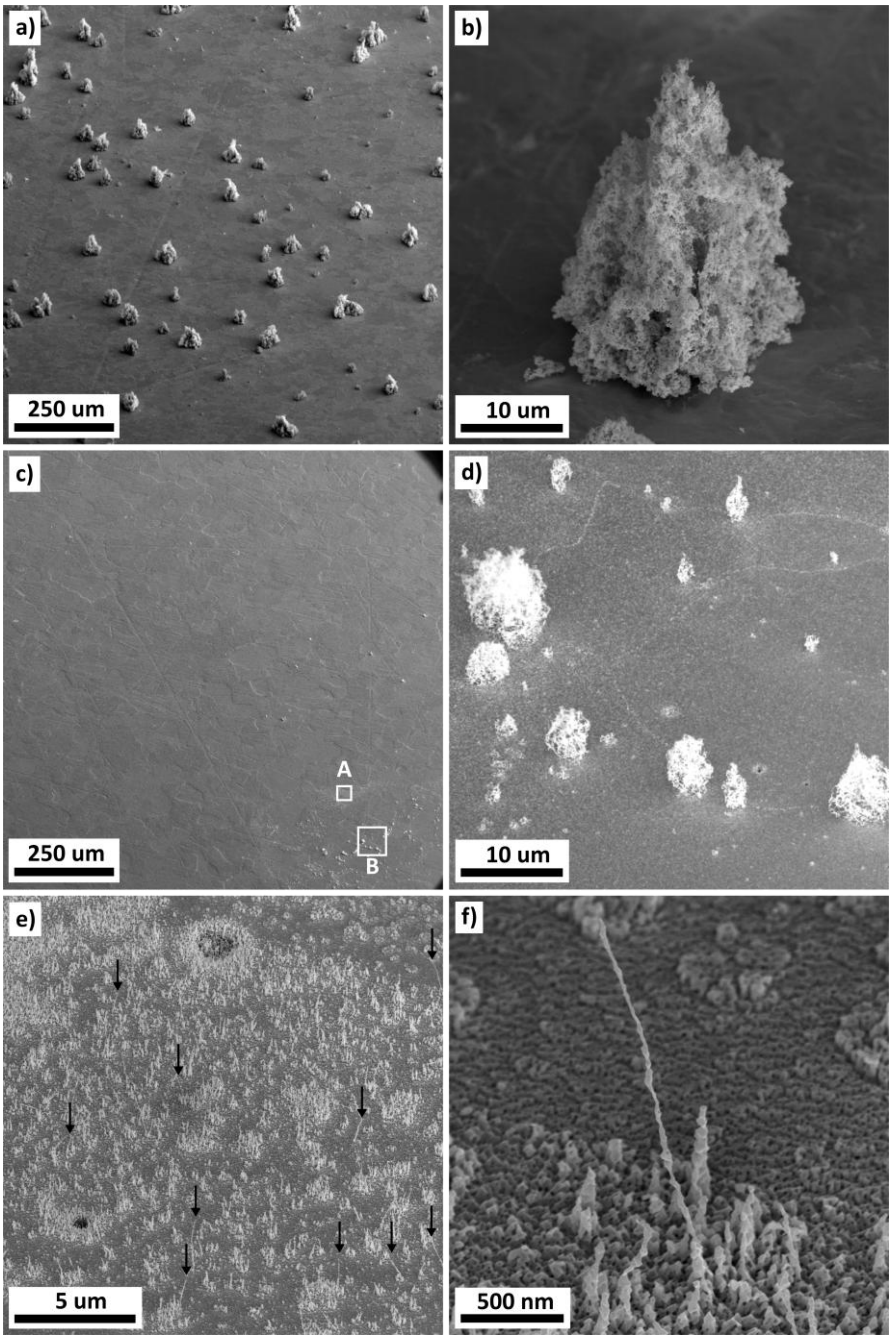

Figure 6-7 | Various forms of nano-tendril surface morphology.
(a) Scanning electron micrograph showing Nano-Tendril Bundle (NTB) growth on a W sample after exposure at 1020 K in the helicon mode plasma with a DC bias of -50 V for a surface averaged He fluence of 7.6 x 10^{25} m^{-2}. The local He ion flux density of the area in view was 2.5 x 10^{22} $m^{-2}s^{-1}$. The local ion energy distribution under these conditions is shown in Fig. 6-5a. (b) Micrograph of a NTB from the same sample as shown in (a). (c) Micrograph near the center of a sample exposed with the RF modulated bias in the inductive mode plasma for the same He fluence as the sample in Fig. 6-6. (d) Detail of the NTB growth in box labeled B in (c). (e) Detail of the grain in the box labeled A in (c) showing multiple single nano-tendrils growing on the grain, some indicated with black arrows. (f) Detail of a single nano-tendril from the grain in (d). All viewing angles are 52° from the sample normal.

6.3 Nano-Tendril Bundles

Quasi-uniform W fuzz growth has been reported as a progression from near-surface bubbles, pinholes, and corrugations at low He fluence, with slight variation depending on crystal orientation [33,59,70,71,103,104], into widespread nano-tendril growth, as long as the sample temperature and He ion energy were above approximately 900 K and 20 eV, respectively. The experimental evidence that has been available so far has shown the inevitable growth of W fuzz over the whole surface of polycrystalline W at long time scales. By amplitude modulation of the incident He ion energy, as opposed to constant ion energy, a rich variety of nanostructures, as shown in Fig. 6-1, was revealed. To demonstrate this, two W samples were exposed to identical He plasmas, but with different biasing schemes. One sample had a DC bias, resulting in a constant ion energy of 45 eV, and one had a bias with a DC component equal to the first sample plus an oscillating component at 13.56 MHz, resulting in an ion energy distribution centered around 48 eV but with peaks in the distribution at 26 eV and 80 eV (Fig.6-5c). In the DC case, the sample developed a W fuzz layer over the sample surface with a depth of 0.95 μm after a He fluence of 5.8 x 10^{25} m^{-2}, as measured by focused-ion beam (FIB) cross section. The W fuzz layer thickness measured is close to the calculated value of 0.89 μm using the empirical growth formula [26] of Baldwin and Doerner, with a correction factor for the lower flux density [23]. In contrast, the sample with ion energy modulation showed a wide variety of features including surface corrugation (Fig 6-1a), isolated nano-tendrils (Fig. 6-1b), and NTB growth (Fig. 6-1c) after exposure to the same background plasma and He ion fluence as the DC case.

The isolated nano-tendrils and NTBs grow much higher away from the surface than the fuzz growth in the DC case, yet clearly are constituted of nano-tendrils like those in fuzz, providing valuable insight to the tendril growth mechanisms. These isolated structures, existing at spatial scales much smaller than grain sizes, indicate that the ion energy modulation effectively increases the growth rate of individual nano-tendrils.

Further insights on tendril growth are obtained by imaging the surface below and adjacent to an NTB structure. A large NTB was coated in platinum (Pt), cross-sectioned by FIB milling, and imaged with the SEM (Fig. 6-8). Cavities from blistering of W after deuterium plasma exposure has been shown to be prevalent in the first 5 μm near the surface [105]. However, in this case just below the surface of the NTB and down to 5 μm deep into the bulk, there is no evidence of voids, or a depression in the bulk W, that would have supplied the W that formed the NTB (see Fig. 6-8b); in fact, quite the opposite, the W in the NTB certainly originate from surrounding surface. High-resolution image analysis of Fig. 6-8b shows the NTB is situated on top of a small "pedestal" of solid W that is 150 nm higher than the smooth surface around the NTB. The quantity of W atoms in the NTB tendrils is the equivalent of a solid W disk 150 nm thick and ~35 micron radius; a distance ~half of the lateral spacing between NTBs on the surface. The most robust interpretation is that the "pedestal" is actually at the original height of the W surface, and the surrounding surface has been lowered by providing W atoms to the NTB. Furthermore, the NTB is clearly attached to the surface, as the nano-tendrils extend from the bulk surface into the NTB.

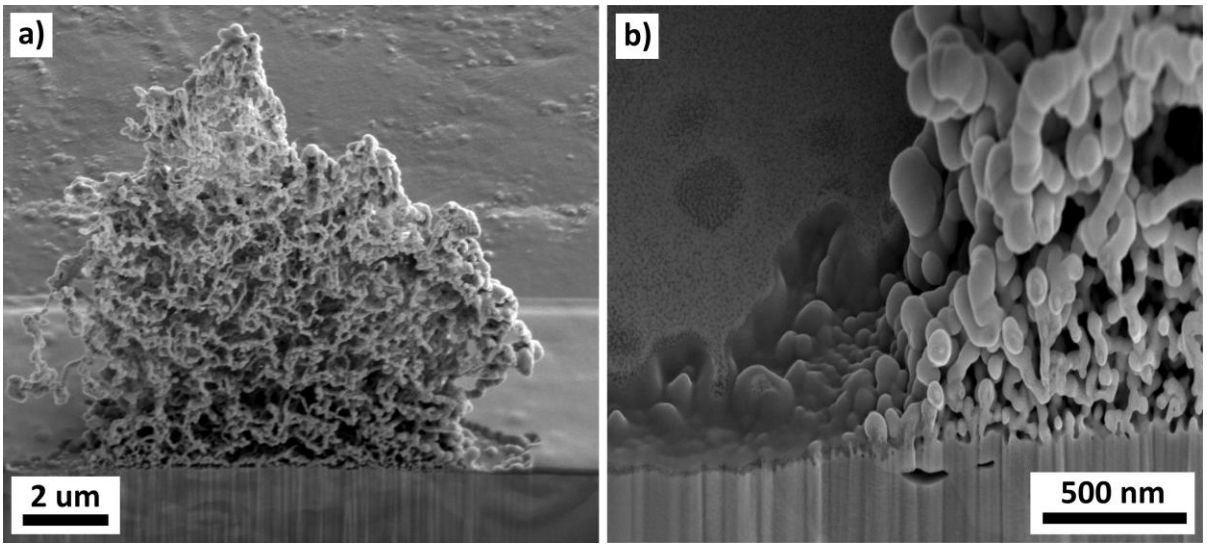

Figure 6-8 | Cross section of a nano-tendril bundle.
(a) Scanning electron micrograph of a nano-tendril bundle near the center of a sample exposed at 1020 K to a He fluence of 7.6 x 10^{25} m^{-2} in the helicon mode plasma after coating with platinum and milling with a gallium ion beam showing the cross section of the nano-tendril bundle. (b) Higher resolution image of a portion of the nano-tendril bundle cross section showing more detail of the difference in the surface morphology between the nano-tendril bundle and the surrounding area, as well as the sub-surface microstructure. The height of the NTB in this cross section is 10 μm and the diameter of the individual nano-tendrils within the NTB range from 40 to 100 nm.

Surface migration of W appears to be the only viable explanation for the formation of the NTBs, It is not possible that the migration is due to the W atoms becoming free of the surface due to some erosion mechanism and re-depositing in the NTB. First the full range of incident He ion energy is below the threshold for physical sputtering. Second, if there was a flux of W atoms away from the surface surrounding the NTB/nano-tendrils by some unspecified erosion mechanism, simple geometry arguments disallow the NTB/nano-tendrils to grow from line of sight accumulation of the eroded W, due to the vanishingly small solid angle subtended by the NTB to surrounding surfaces. Since the W atoms in the NTB clearly do not originate from beneath the NTB, the only explanation left is that the tendrils must be formed by surface migration of the W to the NTB/nano-tendril structures, presumably by W adatoms. This is feasible from an energy point of view because the production of adatoms by ion bombardment will have a lower energy threshold than sputtering [17]. Given the compelling visual evidence for the adatom migration mode of tendril growth, other features of the growth conditions are examined both for general validation of the model and insight as to why ion energy modulation produces these isolated nano-tendril structures.

6.4 Crystallographic orientation effects

The results of section 6.3 clearly point to surface adatom diffusion as the source of NTB growth. The effect of W grain surface crystal orientation is an obvious starting point for further investigation. For orientation measurements, mechanically polished W disks were electropolished using a 4 % sodium hydroxide (NaOH) solution that was maintained at 0°C in a stainless steel vessel, which served as the cathode for the electropolish circuit. The W disks were mounted in a PTFE block with a voltage feedthrough such that only the polished side of the disk was exposed to the NaOH solution. A seal around the edge of the W disk within the PTFE block was created by coating the inside of the block with silicone high vacuum grease. The PTFE block with the W disk mounted on it was placed in the NaOH solution and the best electropolish conditions were found with a bias of 7 V and a current of 0.7A, resulting in a current density of 0.2 $A \cdot cm^{-2}$. The current density was maintained for 45 seconds. Then, the PTFE block and disk were removed from the NaOH solution, rinsed in distilled water, rinsed in ethanol, and then air blown dry. The electropolished samples were kept in a container with silica gel desiccant to avoid oxidation as the samples were transported to the microscopy lab for orientation measurements.

First, fiducial marks were milled into the samples with focused-ion beam (FIB) milling using an FEI Helios NanoLab 600 dual beam field emission scanning electron microscope (SEM) with a gallium ion beam. The fiducial marks were used to compare orientation data to images of post exposure morphology on specific grains. Then, the orientation information along the radius of two samples was performed on a FEI/Phillips XL30 field-emission gun SEM equipped with an EDAX OIM advanced package. A primary electron acceleration voltage of 20 kV was used with a spot size and aperture of 5 each. The samples were exposed to the modulating plasma mode with ion energy distribution as in Fig. 6-5a, which is known to produce a mixture of fuzz and NTBs across the sample. After exposure, optical images were taken along the radius of one sample with an AxioCam MRc digital camera attached to a Zeiss ICM 405 optical microscope shown in Fig. 6-9a. For greater resolution, electron microscopy was performed on the other sample along the radius of the transition region between fuzz and NTBs. Full fuzz growth absorbs optical light, so the grains with full fuzz coverage appear darker than grains without full fuzz growth in optical micrographs. In contrast, surfaces with very high curvature emit more secondary electrons than smooth surface, so nano-tendrils and fuzz appear brighter in SEM micrographs than smoother surfaces. For consistency with optical imaging, the color of the SEM images of Fig. 6-10b has been inverted to show full fuzz grains as dark.

A threshold grayscale value was set in the micrographs that corresponded to full fuzz growth grains. Then, the crystal orientation maps were compared to the micrographs using the fiducial marks milled into the sample before the He exposure for aid in placement and scaling of the images. The crystal orientations that were associated with the full fuzz grains on the micrographs were catalogued and used to generate inverse pole figures for the 5 intervals in radius as shown on the radius axis of Fig. 6-9 and Fig. 6-10. Texture plots of the resulting categories for light and dark grain were calculated by harmonic series expansion to the 16^{th} term with a resolution of 5 degrees.

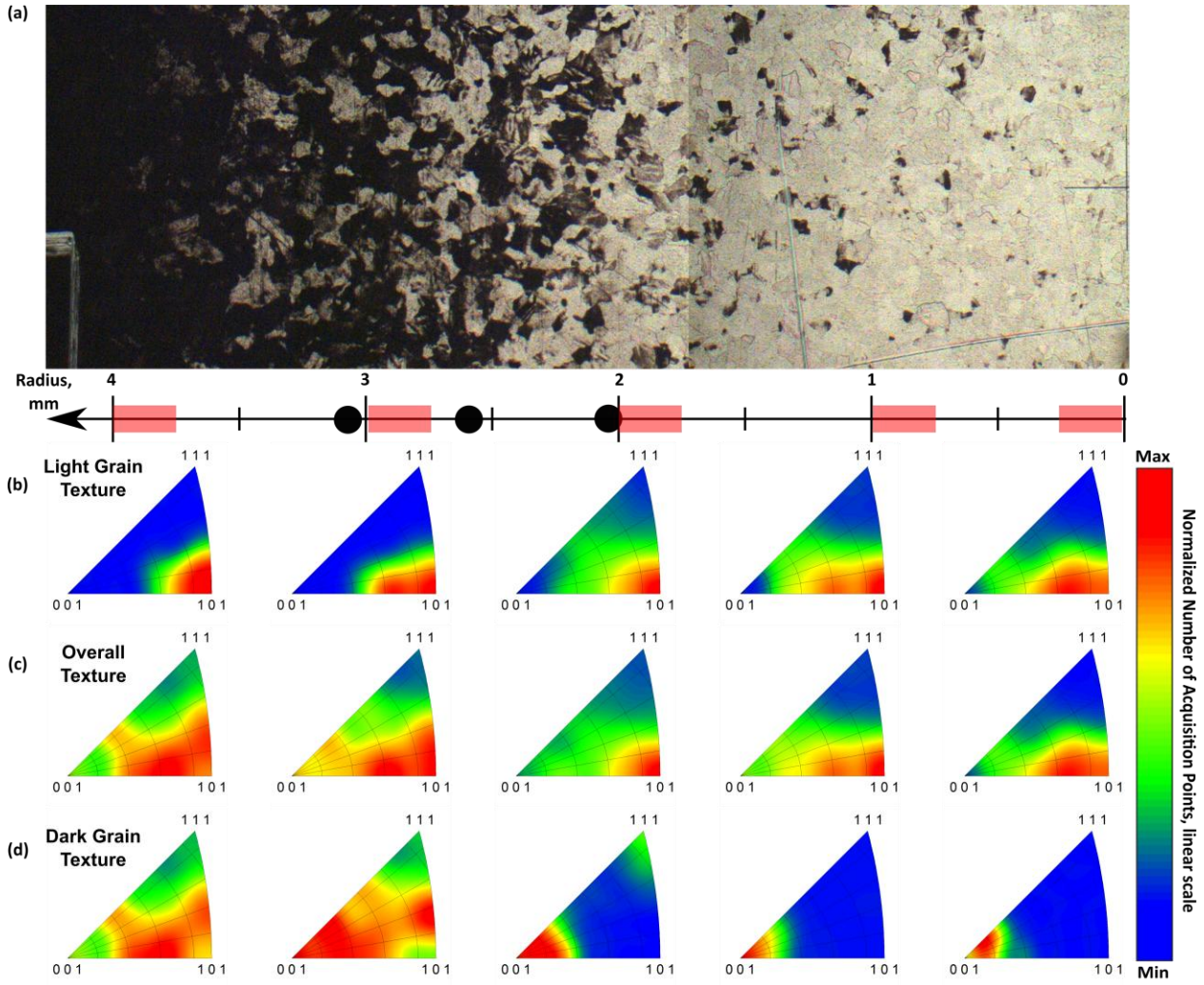

Figure 6-9 | Tungsten fuzz growth dependence on ion energy modulation and crystallographic orientation.

(a) Composite optical micrograph of the radial transition from full fuzz growth (r > 4 mm, dark surfaces) to varied nanostructure growth (r < 4 mm, mixture of dark and light surfaces). The W sample was heated to 1020 K and subjected to He plasma with peak He ion flux density of 9.7 x 10^{21} $m^{-2}{\cdot}s^{-1}$ at r = 0 mm and intrinsic ion energy modulation due to the 13.56 MHz RF plasma source for 2500 seconds. The incident ion properties were as follows: at r = 0 mm, $\langle E \rangle$ = 60 eV, ΔE = 42 eV and at r = 4 mm, $\langle E \rangle$ = 55 eV, ΔE = 32 eV. (b) Texture plots of the light grains which have corrugations and isolated nano-tendril/NTB growth. (c) Overall texture plots of all the grains in the corresponding radius interval for comparison to (b) and (d) texture plots. (d) Texture plots of the dark grains which have fuzz growth. The horizontal axis shows red rectangles as the 5 radial intervals in which the crystal orientation data was used to generate the texture plots of (b), (c), and (d). The black dots on the radial axis mark the locations of where corrugation wavelengths were measured for Fig. 6-14.

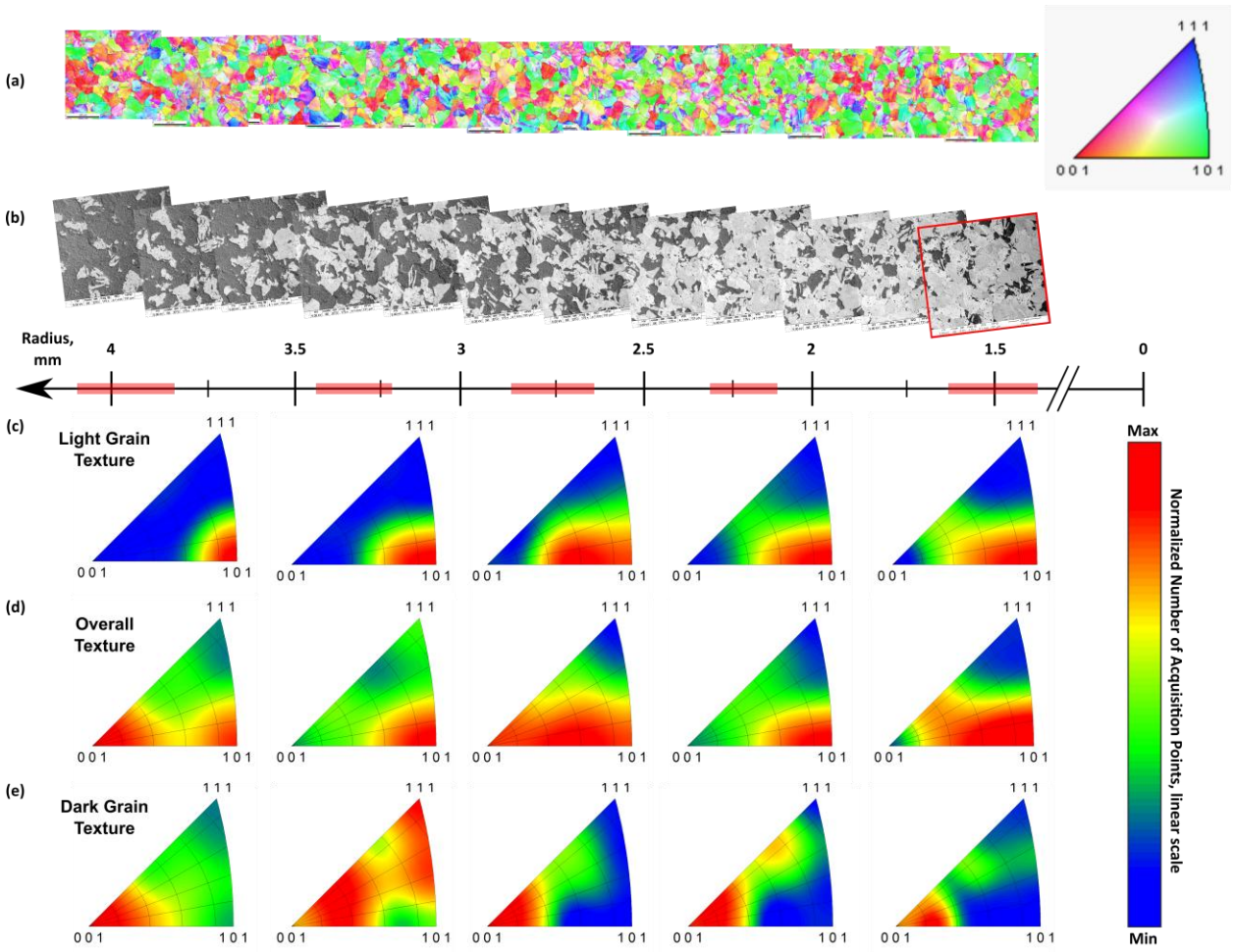

Figure 6-10 | Grain-to-grain threshold for full tungsten fuzz growth depending on ion energy modulation and crystallographic orientation.
(a) Composite of OIM orientation maps showing the crystal orientation measured along the radius of the sample before it was exposed to plasma. The inverse pole figure to the right is the color map legend to the stereographic projection of the crystal orientations. (b) Composite of SEM images showing the radial transition from full fuzz growth to varied nanostructure growth. The color of the SEM images has been inverted so that full fuzz growth appears dark and non-full fuzz growth appears light. The W sample was heated to 1020 K and subjected to He plasma with greater amplitude modulation at the center of the sample than at larger radii and a He ion flux density of 9.7×10^{21} $m^{-2} \cdot s^{-1}$ at the center. The average ion energy incident at r = 0 mm was 55 eV with a peak-to-peak modulation of 42 eV at 13.56 MHz. The peak-to-peak modulation was 32 eV with the same average ion energy of 60 eV at a radius of r = 4 mm. The minimum He fluence was 8.4×10^{24} m^{-2} and occurred at r = 12.7 mm. For r > 4 mm, almost all grains showed full fuzz growth. For r < 1.5 mm, almost all grains had alternative nanostructures of corrugations, NWs, and NTBs. (c) Texture plots of the grains without full fuzz growth. (d) Texture plots of all the grains to compare to the texture plots of (c) and (e). (e) Texture plots of the grains with full fuzz growth. The horizontal axis for (a) and (b) shows the radial interval in which the crystal orientation data was used to generate the texture plots of (c), (d), and (e) as red rectangles. The wavelength and orientation of corrugations were analyzed from the SEM image at r = 1.5 mm which is traced in red in (b).

The transition region (0 mm < r < 4 mm) shows grains that have full fuzz growth coverage immediately adjacent to other grains that instead have nano-tendril/NTB structures (Fig. 6-11). Orientation imaging microscopy (OIM) was performed on the W sample prior to exposure with an EDAX OIM advanced package on an FEI/Phillips XL30 field-emission gun SEM. Nanostructures were grown on the sample and imaged with a Zeiss ICM 405 optical microscope equipped with an AxioCam MRc digital camera for a wide view of the transition region. Full fuzz growth absorbs light, so the grains with full fuzz coverage appear black in the optical images of Fig. 6-9a and 6-11a. Starting at larger radii (i.e. r > 4 mm at left of the image in Fig. 6-9), every grain shows full fuzz growth. Moving to the right in the image, the grains that first exhibit NTB growth and retain macroscopic optical reflectivity have a {101} orientation (see Fig. 6-9b). It should be noted that the overall grain texture of the sample is not uniform, as shown in Fig. 6-9c, but mainly has {101} and {001} components, with the {111} type grains contributing less than 5% to the overall texture. The {001} type grains are the only type to show full fuzz growth (see Fig. 6-9d and Fig. 6-10e) near the center of the sample (r < 0.5 mm) where the ion energy amplitude modulation and flux density are the greatest. The conclusion of Fig. 6-9 and 6-10 is that under conditions of 13.56 MHz ion energy modulation, the dominant tendril growth structure (i.e. fuzz or NTB) is highly dependent on invidual grain orientation. This is generally expected if surface diffusion is playing the dominant role in nano-tendril growth because adatom surface energy barriers vary with grain orientation.

The change in He fluence (or flux) across the sample is not the cause of the radial variation in fuzz growth. This is first obvious by the variation in tendril growth on adjacent grains that have effectively identical flux/fluence. Secondly, others have shown that at low He fluence, precursor structures such as corrugations [59,70,71,103] and loops [33] are observed rather than fuzz. The fluence necessary prior to fuzz growth has been called an incubation fluence [22–24], and its value is reported in the range 1.5 – 4 x 10^{24} m^{-2} in the temperature range 1000 – 1200 K. In Fig. 6-9, the lowest He fluence on the sample is 2.9 x 10^{25} m^{-2} – well in excess of the incubation fluence. Also, full fuzz growth occurred on the sample in Fig. 6-9 for *lower* flux density/fluence regions (larger radii). If the ion irradiation was monoenergetic, the fuzz growth would increase with the flux density/fluence, which is the opposite of what is observed here.

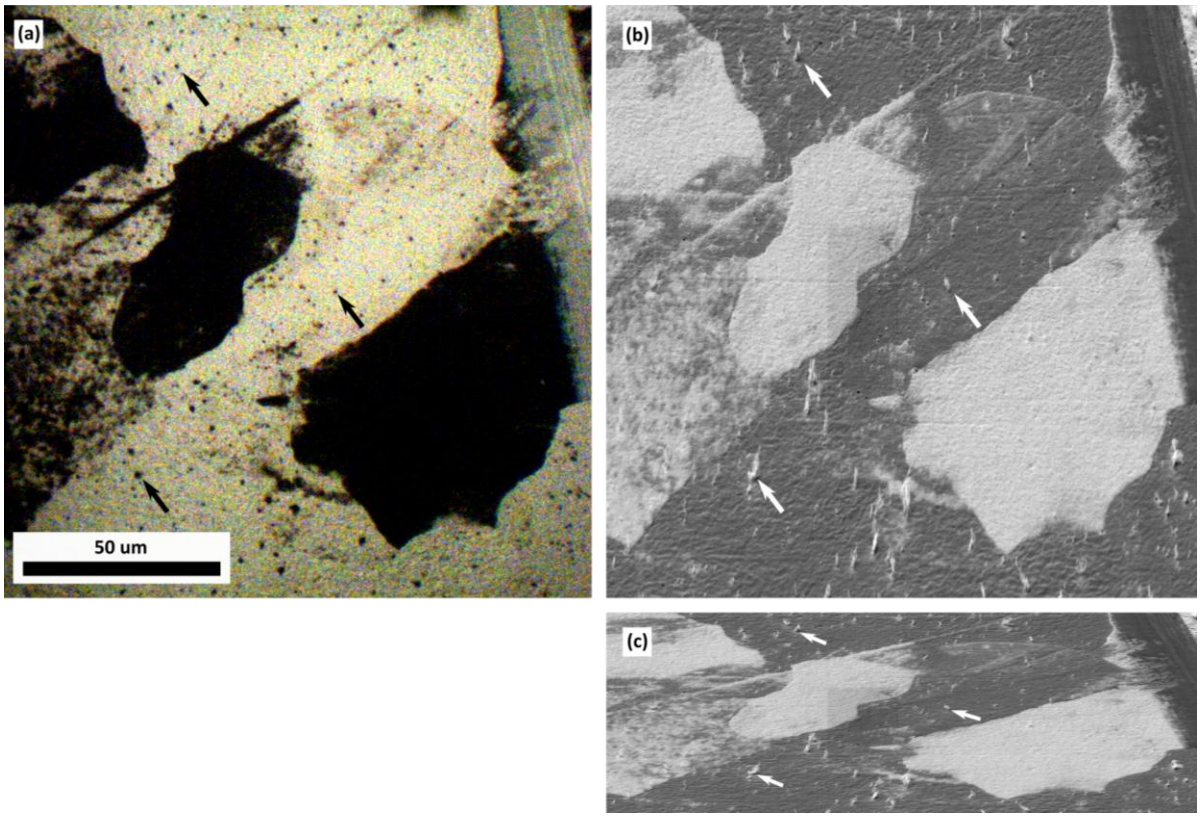

Figure 6-11 | Comparison of optical and electron micrographs of surface morphology.
(a) Higher magnification optical micrograph at r = 2 mm from the sample in Fig. 6-9 viewing perpendicular to the surface. The black areas are grains with fuzz growth and the small black dots are isolated nano-tendrils/NTBs. The arrows highlight three corresponding NTBs among the images, but there are over 100 NTBs in the viewing area. (b) SEM micrograph of the same area as (a). The sample was tilted by 70 degrees from the electron beam in the SEM for orientation analysis. The y-direction in the electron micrograph is corrected so that the surface plane appears normal to the viewing direction, like in (a). The fuzz and NTBs are brighter than the smoother surface because high curvature surfaces emit more electrons. (c) Same electron micrograph as (b) without the y-direction corrected for tilt, showing the view along the electron beam direction and the large NTBs. The scale bar in (a) is valid for (b) and (c), as well.

Since ion energy modulation has been shown here to inhibit fuzz growth on an initially smooth surface, the effect of ion energy modulation on a sample with full fuzz already grown on the surface was tested. Tungsten fuzz was grown on two samples with the same exposure conditions. One sample was used for imaging the fuzz (Fig. 6-12a) and the second sample was imaged after exposure to the helicon wave-coupled plasma with ion energy modulation of ΔE = 42 eV (Fig. 6-12b). After being subjected to the He ion energy modulation, the surface regained macroscopic reflectivity and, upon microscopic inspection, exhibited clear NTB growth (Fig. 6-12c). The surface regained macroscopic reflectivity because the surface roughness decreased during the exposure to the plasma with ion energy modulation. This test clearly verifies that ion energy modulation produces surface W migration conditions that both make NTBs and alter existing nano-tendrils. Importantly this reconfirms that surface mobility is commonly governing the creation/destruction of tendrils in NTBs/fuzz. The coverage of NTBs is greater when the initial surface condition is W fuzz versus smooth, but this may simply be due to the greater roughness W fuzz promoting a higher probability of

NTB growth. Tungsten fuzz surfaces can be made smooth again by high temperature (>1000 K) annealing [106]. In this case, ion energy modulation may be inhibiting nano-tendril growth in specific locations and the high temperature is activating nano-tendril decomposition by surface tension forces.

There is an obvious large impact of both grain orientation and ion energy modulation involved in determining the dominant type of nano-structure produced on a grain. A heuristic explanation based on adatom surface migration follows; tendril growth is set by the time-dependent rate competition between production, annihilation with vacancies (produced simultaneously with adatoms during ion bombardment), diffusion, and incorporation into nano-tendrils. While a detailed model is beyond the scope of this thesis, the trends of these new experimental observations follow this explanation.

1. Adatoms are produced predominantly by the He ion bombardment, since the thermal equilibrium adatom concentration at these temperatures is negligibly low. The yield of adatoms per incident ion is a nonlinear function of the incident ion energy above the threshold for adatom production [18,19,107]. This adatom production rate is varied instantaneously by the energy modulation present. Also, the adatom yield is dependent on the surface crystal orientation. Surface orientations with higher roughness have lower surface binding energy [108] and so would yield more adatoms per ion of a given energy. Thus, the adatom production rate is granular and temporally dependent.

2. The isolated nano-tendril/NTB growth favors a situation where the energy modulation is largest. In this case, the instantaneous rate of adatom production will be both the highest and lowest at the zenith (60 eV + 21 eV = 81 eV) and nadir (60 eV – 21 eV = 39 eV), respectively, of the modulation period in Fig. 6-9. This would present a change in adatom yield by up to an order of magnitude over the period of the modulation (74 ns for f_{RF} = 13.56 MHz).

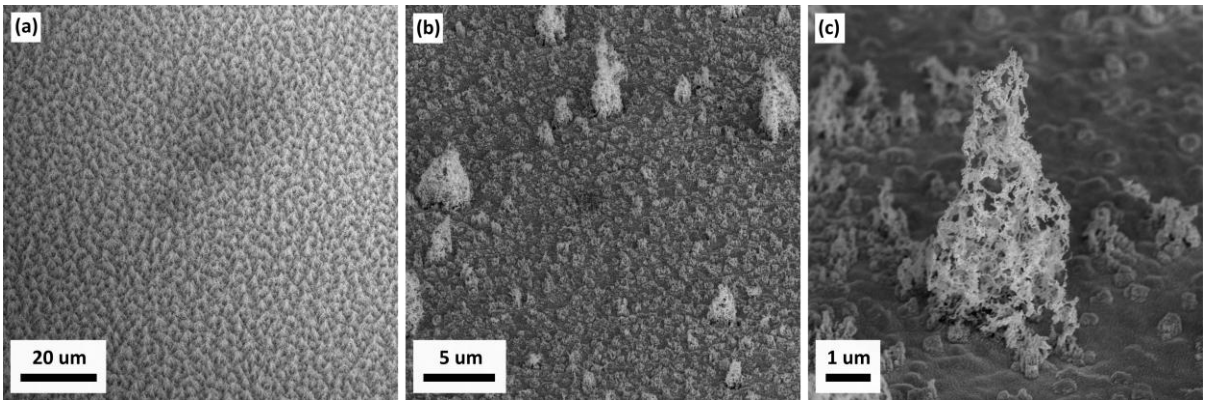

Figure 6-12 | Ion energy modulation changes tungsten fuzz to NTB growth.
(a) SEM image of a W sample at 1020 K exposed to a He flux density of 2.6 x 10^{21} $m^{-2}\cdot s^{-1}$ with a DC bias of -50 V for 3000 s, resulting in W fuzz. (b) SEM image of a W sample prepared in the same way as in **a**, and then exposed at 1020 K to a He ion flux density of 9.7 x 10^{21} $m^{-2}\cdot s^{-1}$ with intrinsic He ion energy modulation at 13.56 MHz for 5000 s. The average ion energy and peak-to-peak ion energy were $\langle E \rangle$ = 60 eV and ΔE = 42 eV, respectively. (c) Higher magnification image of a NTB and the surface detail on the sample in (a). The viewing angle for each micrograph is 52°.

3. The change in the adatom production rate over the period of the energy modulation impacts the rate competition between kinetic and thermal effects sufficiently to modify the nano-tendril nucleation on the surface, i.e. the ion energy modulation is effectively decreasing the lifetime of nano-tendrils, or characteristic time for nano-tendril decay. This decreases the quasi-steady state coverage of nano-tendrils. With fewer nano-tendrils, their growth rate increases, ultimately limited by the diffusivity of the adatoms.

4. The hierarchy of surface self-diffusivity of W [109,110], i.e. W adatom migration on a W substrate, is such that the {101} plane has higher diffusivity than the {111} and {001} planes. This is because the {101} plane is the close-packed plane of the BCC crystal structure of W. Under the same ion energy modulation and fluence, isolated structures occur on grains with higher diffusivity. This is consistent with the requirement that the isolated nano-tendril/NTB must form from larger average migration distances than occurs with uniform fuzz. Conversely, uniform fuzz favors slower diffusion. This hierarchy is completely consistent with the results shown in Fig. 6-9 and 6-10.

6.5 Topographic instability model

The results of the previous sections clearly indicate that the nano-tendrils grow due to surface adatom W diffusion and that growth is affected by ion-energy distributions and grain orientation as expected. However another underlying question to nano-tendril growth is why they are the energetically favorable structures to occur. This leads us to hypothesize that the tendrils, and their nucleation, are in fact a form of topographic instability. This view is partially driven by the presence of periodic surface "corrugations" in Fig. 6-13. In order to investigate this hypothesis, an analytical formula is derived to estimate the corrugation wavelength to compare to the experimental measurements. Since there is theoretically no physical sputtering involved in the development of the corrugations seen in this work, the principles of the Bradley-Harper linear instability model [111] were applied but only with the essential terms for thermally activated surface relaxation, *B*, and roughening due to Ehrlich-Schwoebel (ES) diffusion barriers across steps. Assuming the surface starts as a plane, *h*, and that the surface plane changes slowly with respect to diffusion, the partial derivative of the surface plane with respect to time is

$$\frac{\partial h}{\partial t} \cong \sum_i [-S_i \nabla_i^2 h - B_i \nabla_i^2 (\nabla_i^2 h)], \tag{6.1}$$

where the sum is over the principal crystal directions *i* for surfaces with anistropic diffusion. The relaxation coefficients [112] are

$$B_i = \frac{\gamma D_i C \Omega^2}{k_B T}, \tag{6.2}$$

where γ is the surface tension, D_i is the diffusivity in the i direction, C is the areal density of the diffusing species, Ω is the atomic volume, k_B is Boltzmann's constant, and T is the surface temperature. The roughening coefficients in the small curvature approximation [113] are

$$S_i = \frac{\Gamma Y_a l_{i,s} {l_{i,d}}^2 \Omega}{2(l_{i,s}+l_{i,d})a_0}, \tag{6.3}$$

where Γ is the He ion flux density, Y_a is the adatom yield due to He ion bombardment, $l_{i,s}$ is the so-called Schwoebel length in the i direction, $l_{i,d}$ is the diffusion length in the i direction, and a_0 is the lattice parameter. The Schwoebel length is defined as

$$l_{i,s} = a_0\left[exp\left(E_{i,ES}/k_B T\right) - 1\right], \tag{6.4}$$

where $E_{i,ES}$ is the ES energy barrier that is responsible for the anisotropic diffusion up and down terrace steps in the i direction. The diffusion length is taken as the mutual spacing of the adatoms generated during the He ion bombardment,

$$l_{i,d} = \left(\frac{D_i}{\Gamma Y_a}\right)^{1/4}. \tag{6.5}$$

Equation (6.5) is valid only early in the exposure when adatoms annihilate mainly with vacancies produced simultaneously during the ion bombardment (i.e. thermal vacancies are negligible and the nano-tendril areal density is low.). Equation (6.1) is solved in Fourier space with the principal crystal directions i=1 and i=2 on the surface, $h(x,y,t)$ with initial amplitudes $A_0(k_1,k_2)$, aligned in the x and y directions

$$h(x,y,t) = A_0(k_1,k_2)\exp\left[i(k_1 x + k_2 y) + rt\right], \tag{6.6}$$

where r, called the amplification factor, has to be

$$r = S_1 k_1^2 + S_2 k_2^2 - B_1 k_1^2(k_1^2 + k_2^2) - B_2 k_2^2(k_1^2 + k_2^2), \tag{6.7}$$

to satisfy Eqn. (6.1). Solving for the maximum amplification factor with respect to k_1 and k_2 gives the dominant characteristic wave number that would appear at long time scales compared to diffusion. Taking the partial derivative of Eqn. (6.7) with respect to the wave numbers and setting equal to zero gives

$$k_i = \sqrt{\frac{S_i}{2B_i} + k_j^2 \frac{(B_i+B_j)}{2B_i}}, \tag{6.8}$$

where *i* is one principal direction and *j* is the other. Assuming strong anisotropic diffusion such that one principal direction wave number is much greater than the other (i.e. $k_i >> k_j$), the dominant wave number is found to be (dropping the subscripts),

$$k \cong \sqrt{\frac{S}{2B}}, \tag{6.9}$$

giving the characteristic wavelength of the corrugations as

$$\lambda = \frac{2\pi}{k} = 2\pi\sqrt{\frac{2B}{S}}. \tag{6.10}$$

Substituting Eqn. (6.2)-(6.5) into Eqn. (6.10) leads to

$$\lambda = 4\pi\left(\frac{\gamma\Omega a_o}{k_B T}\right)^{1/2}\left(1+\frac{l_d}{l_s}\right)^{1/2}, \tag{6.11}$$

with

$$\frac{l_d}{l_s} = \frac{1}{a_0}\left(\frac{D_0}{\Gamma Y_a}\right)^{1/4}\left[\frac{\exp\left(-\frac{E_d}{4k_B T}\right)}{\exp\left(\frac{E_{ES}}{k_B T}\right)-1}\right]. \tag{6.12}$$

Since there is no data available for the adatom yield of W from He ion bombardment, a model value was assumed. It has been shown with xenon bombardment of platinum [18] that the adatom yield can be comparable to the sputter yield at or below the threshold for sputtering. Since the He ions are below the threshold energy for physical sputtering on W, the approximate value for the adatom yield is $Y_a = 10^{-3}$ for this He ion energy range [19]. For a He flux density of 5 x 10^{21} $m^{-2}\cdot s^{-1}$, the adatom yield rate is $\Gamma\cdot Y_a = 5 \times 10^{18}$ $m^{-2}\cdot s^{-1}$, which is equivalent to 0.25 monolayers of W per second. Also, the diffusion parameters are taken to be those measured for the {101} surface [109].

Also, the characteristic time for the dominant wavelength to develop can be calculated from the inverse of Eqn. (6.7). For the dominant principal direction, Eqn. (6.7) to lowest order is

$$r_{k_1 \gg k_2} \cong S_1 k_1^2 - B_1 k_1^4 = \frac{S^2}{4B}. \tag{6.13}$$

The inverse of the amplification factor is equivalent to the 1/e time constant for the surface to show the dominant wave vector. Using Eqn. (6.2)-(6.5) in Eqn. (6.13) and taking the inverse leads to

$$\tau_{k_1 \gg k_2} \cong \frac{16\gamma a_0^2}{k_B T} (D_0 \Gamma Y_a)^{-1/2} \left[\frac{1+\frac{l_d}{l_s}}{\exp\left(-\frac{E_d}{4k_B T}\right)} \right]^2 . \tag{6.14}$$

Equation (6.11) is used to derive a value for the ES barrier from a fit to the data of corrugation wavelengths in the text. Equation (6.14) is used to calculate the 1/e time constant of corrugation development assuming the derived ES barrier.

6.6 Helium ion-induced corrugations

Corrugations such as in Fig. 6-1a are observed at the surface for all of the temperatures and ion energies in this study, but vary in magnitude and wavelength depending on grain crystal orientation, surface temperature, and He ion plasma exposure conditions (see Fig. 6-13). The corrugations even develop without ion bombardment at elevated temperatures, such as during annealing of a polished W sample at 1270 K for 1 hour (Fig. 6-13a). This may be due to restructuring of surfaces to lower energy states by surface tension and surface diffusion activated by high temperature [114]. Miyamoto, *et al.* also observed corrugations in W samples at this temperature under TEM investigation without ion bombardment [115] which they attributed to restructuring due to surface tension. However, thermally activated restructuring is enhanced by He ion bombardment (compare Fig. 6-13a to 6-13b), so that He ion bombardment can produce more pronounced corrugations even for temperatures below 900 K (see Fig. 6-13d).

During plasma exposure, but prior to W fuzz growth, corrugations develop during what is called an incubation period [22–24]. Once W fuzz growth begins and the fuzz layer thickness increases, the morphology of the base is hidden and variations in the nanostructure growth due to crystal orientation are no longer apparent by SEM inspection. Parish, *et al.* have also observed the crystal orientation to change along the length of individual nano-tendrils [116]. Other researchers studying W fuzz have hypothesized [70,71] that the corrugations are a harbinger to nano-tendril growth, where roughening by corrugations and perforation of the surface with He bubbles leads to necessary surface deformation for nucleation of nano-tendrils. In this theory, He bubbles near the surface of the W cause corrugations due to bubbles expanding the W lattice along slip planes, with the close-packed direction <111> being the common slip direction for BCC metals.

Another possibility is the corrugations develop from topographic instabilities due to anisotropic diffusion of adatoms, which, in the absence of He bubbles, have been observed and studied for many decades due to ion bombardment involved in semiconductor and thin film research [41,111–113,117–120]. The main difference here when compared to these other fields of research is the presence of He bubbles in the surface. Void or bubble superlattices have been found to develop during ion bombardment by Di *et al.*[121], but the superlattice is usually produced with higher energy ions (22 keV) and lower sample temperatures (520 K). Also, He gas accumulation was considered by Schwoebel [68] as a possible cause of "microprotrusions" he observed on field emitter tips, but the low He flux density was thought to be too low for appreciable bubble pressures to form, and the temperature was high enough

for He cluster dissociation rather than accumulation. He concluded that the microprotrusions were not due to He accumulation and bubble nucleation. For low energy, high flux He ion bombardment, such as used in our plasma experiments, He bubbles have so far been necessary for nano-tendril growth, but the contribution of the He bubbles may be towards affecting surface diffusion through adatom production [61,122] and surface stresses [19,37,38] rather than volumetric expansion of the lattice. This fits with our observation that He bubble pressure is insufficient for significant bulk distortion.

By modulating the ion energy, and, thus, modifying the surface kinetics, the growth of uniform fuzz that is normally active under constant ion energy conditions is suppressed, as shown in the previous sections. The prevailing morphology becomes the corrugations with a low coverage (θ < 10 %) of nano-tendril and NTB growth. From the crystal orientation data and imaging of the surface, corrugations are most pronounced on high diffusivity surfaces. The high diffusivity surfaces are the {101}, {112}, and {123} oriented grains and have <111> close-packed directions on the surface.

The wavelengths of the corrugations were determined by calculating the Fast Fourier Transform of corrugated grains in the SEM image bordered in red in Fig. 6-10b and on SEM images taken at the radial locations marked by black dots on the radial axis in Fig. 6-9. The distribution of wavelengths is plotted in Fig. 6-14a as the dashed line. The distribution of wavelengths on another sample subjected to the same He plasma, but with a lower temperature of 690 K, is shown in Fig. 6-13d. The wavelength distribution has a similar shape between the two temperatures, i.e. with a skewed distribution towards smaller wavelength. However, the lower temperature distribution is shifted to shorter wavelengths. There is no measurable dependence of the wavelength on the presence of ion energy modulation shown here. The corrugation wavelengths were measured at two additional temperatures of 1270 K and 530 K exploiting the robust temperature control capabilities of the sample stages in this flux density and ion energy range. The corrugation wavelength of images in other published works [59,79] studying He ion bombarded W with He flux densities and average ion energies listed in Table 6-2 were also measured. The results are summarized in Fig. 6-14b. The corrugation wavelength clearly increases with the surface temperature.

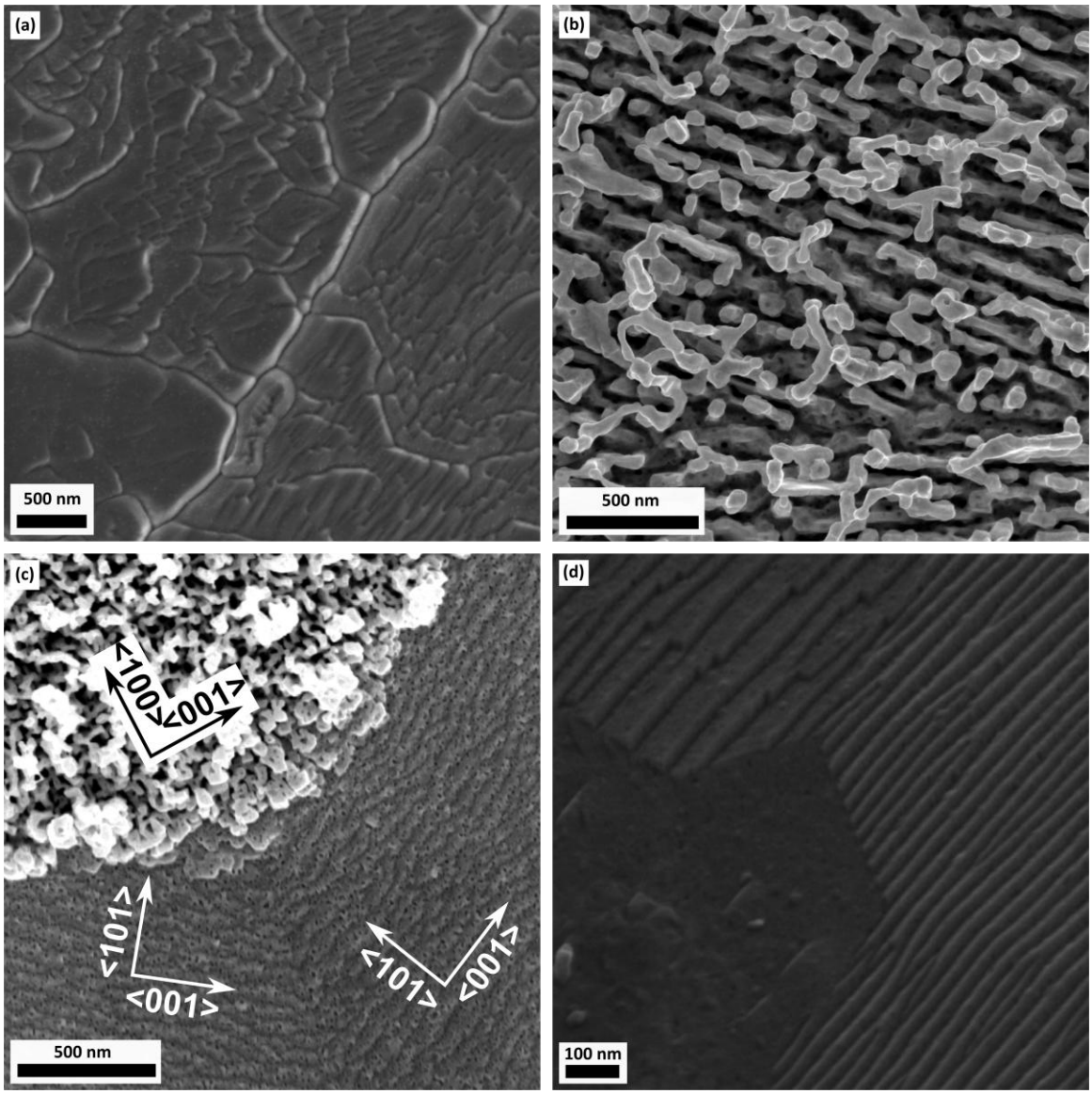

Figure 6-13 | Thermally activated and helium ion-enhanced corrugations on tungsten.
(a) SEM image of a W sample that was mechanically polished, then annealed at 1270 K for 1 hr (no He ion bombardment). Corrugations with a characteristic wavelength of 123 nm are on the lower right grain in the image. Grain boundary grooving due to the annealing can also be seen. (b) Image of a W sample prepared in the same way as in (a), and then subjected to a He ion flux density of 1.5 x 10^{21} $m^{-2} \cdot s^{-1}$ and a constant He ion energy of 50 eV to a He fluence of 4.9 x 10^{24} m^{-2} with a surface temperature of 1270 K. The corrugations at the surface can be seen through the thin grove of nano-tendrils that are 600 nm tall normal from the surface as measured by FIB cross section (not shown). The corrugation wavelength of the upper grain in the image is 130 nm. (c) Image at r = 1.5 mm of the W sample of Fig. 6-10 showing a grain with full fuzz growth (upper left) adjacent to two grains with only corrugations. The height of the nano-tendrils of the full fuzz growth grain is 300 nm with the base of the fuzz layer level with the corrugations of the adjacent grains. The full fuzz growth grain is vicinal to the {001} orientation while the two corrugated grains are vicinal to the {101} orientation. The principal crystal directions on the surface for each grain are labeled by the axes over each grain. The characteristic wavelength of the corrugations on both corrugated grains is 58 nm with the wave vector aligned parallel to the <101> direction. (d) Image of a W sample exposed to the same plasma as (c), but with a lower surface temperature of 690 K. Two areas on the image have corrugations in the same direction: upper left grain wavelength = 67 nm, right/lower grain wavelength = 36 nm.

The corrugation wavelength follows the trends expected from the linear instability model derived for sputter-patterning and epitaxial growth. Assuming appropriate adatom yield and diffusion parameters [18,19], the only free parameter left to calculate the corrugation wavelength is the ES barrier, E_{ES}. The best fit for this model was achieved with E_{ES} = 0.145 eV and is plotted as the dashed line in Fig. 6-14b. One of the earliest observations of a step diffusion barrier was presented by Ehrlich and Hudda [123] during Field Ion Microscopy (FIM) studies on W, in which they state a barrier of 0.065 eV for {101} surfaces. It should be noted that the FIM work was performed at a lower temperature (< 350 K). Also, the FIM technique is a direct observation of the displacement of adatoms on the surface, whereas this work derives a diffusion barrier indirectly from the long time-scale redistribution of the surface. Also, the concurrent roughening due to pores opening on the surface from the release of He would affect surface diffusion and is not incorporated in the simple model from which Eqn. (6.10) was derived.

Taking the ES barrier as derived from the fit to the data, the 1/e time constant for corrugations to develop can be calculated with (see methods)

$$\tau = \frac{S^2}{4B}. \tag{6.15}$$

For the experimental parameters in Table 6-2, the 1/e time constant ranges from 16 to 160 s. Besides time, morphology changes have been correlated with the He fluence to the surface, which is simply the exposure time multiplied by the He flux density. For these experiments, the characteristic 1/e He fluence ranges from 1.3 to 7.9 x 10^{23} m^{-2}. This is an order of magnitude lower than the incubation fluence observed for W fuzz growth, which fits with the observation that these corrugations develop prior to W fuzz growth.

The topographic instability model describes the corrugation wavelength well at these ion flux densities and energies. We've also analyzed images of corrugations in other published works at lower ion energy [11,70] (E_{He} < 40 eV) or lower flux density [71] (Γ_{He} < 10^{21} $m^{-2}\cdot s^{-1}$) and found that the characteristic wavelength is inversely proportional to some power of the flux density and ion energy above a temperature of 1400 K, but almost independent of flux density and ion energy below this temperature. This dependence on flux density and ion energy is in qualitative agreement with the topographic instability model [41,124], but a more focused study is needed for a quantitative assessment. Also, any ion-induced relaxation of the surface [117], which would alter the resulting fit with the ES barriers at lower temperatures, where the thermally activated relaxation is weak, were not taken into account. Since the linear topographic instability model does well to describe the corrugations, additional considerations for the nonlinear terms of this model that might incorporate the effects 3 dimensional growth could serve as an analytical starting point to describe nano-tendril growth and is the subject of further study.

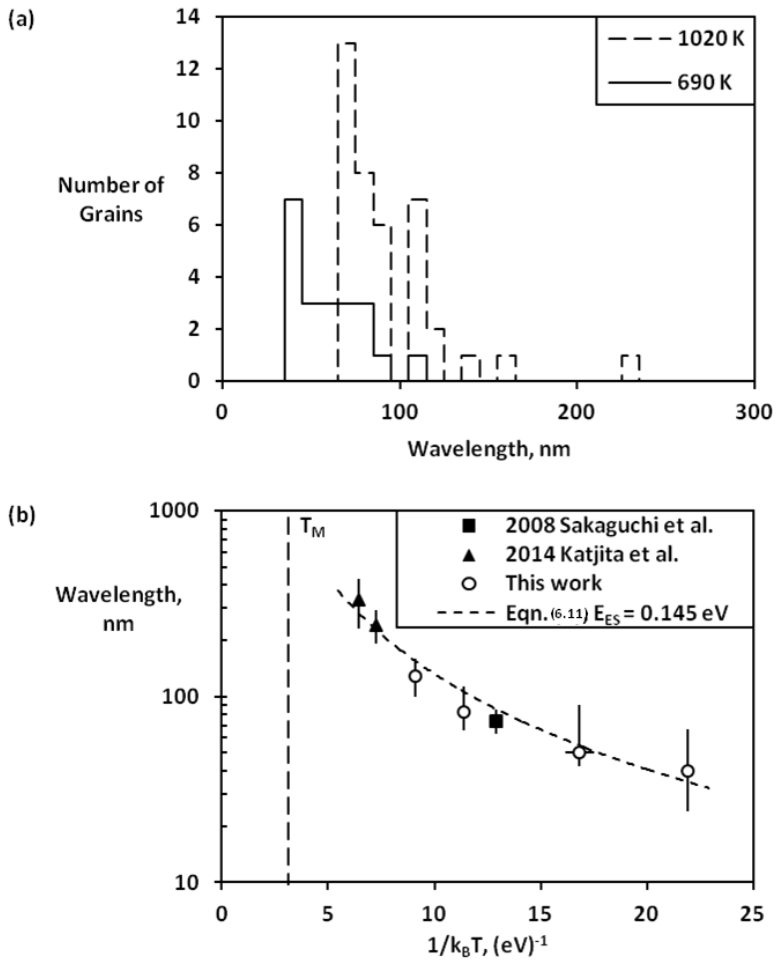

Figure 6-14 | Characteristic wavelength of corrugations that develop during helium ion bombardment of tungsten surfaces.
(a) Wavelength distributions of corrugations imaged on two samples subjected to the same He plasma with ion energy modulation as in Fig. 6-9 and 6-10, but at two different temperatures. (b) Plot of the corrugation wavelengths measured from images of samples exposed at four different temperatures in this work along with measured corrugation wavelengths from two other published works with He ion flux densities and average He ion energies listed in Table 6-2. Also plotted are corrugation wavelengths calculated from linear instability theory of adatoms diffusing on surfaces with ES barriers of E_{ES} = 0.145 eV for adatom diffusion (dashed line) for a He flux density of 5 x 10^{21} $m^{-2}{\cdot}s^{-1}$ with ion energy of 55 eV.

Table 6-2 | Growth conditions of corrugated surfaces found in this and other works

Surf. Temp., K	Average He Ion Energy, eV	He Flux Density, 10^{21} $m^{-2}{\cdot}s^{-1}$	Corrugation Wavelength, nm	Calculated Wavelength[a], nm	Calculated time constant[a], s	Reference
530	60	8.2	24-67	32	26	This work
690	60	9.7	42-90	50	16	This work
900	50	10	63-85	93	28	2008 Sakaguchi, *et al.*
1020	60	9.7	66-113	131	38	This work
1270	50	1.8	100-160	157	72	This work
1600	55	5	200-300	215	123	2014 Kajita, *et al.*
1800	55	5	250-450	254	158	2014 Kajita, *et al.*

[a]Calculated with E_{ES} = 0.145 eV

6.7 Summary

By manipulating the surface kinetics through temporal modulation of the incident He ion energy, tenets of the nature of W nano-tendril growth are unveiled. The suppression of uniform nano-tendril (fuzz) growth by ion energy modulation indicates the nucleation mechanism of nano-tendril growth is sensitive to the surface kinetics, with minimum fuzz coverage when the magnitude of the amplitude modulation is 42 eV at a frequency of 13.56 MHz about the average ion energy of 60 eV. In regions adjacent to nano-tendril growth, a linear topographic instability model was applied to ion-induced corrugations with reasonable quantitative agreement, when the Ehrlich-Schwoebel diffusion barrier is 0.145 eV for adatom diffusion, for He flux densities near 5×10^{21} $m^{-2} \cdot s^{-1}$ and average ion energies in the range of 50-60 eV. In addition to fuzz and ion-induced corrugations, a newly discovered nano-tendril morphology develops while the ion energy is modulated, which features isolated nano-tendril bundles and single nano-tendrils that nucleate at distances many orders of magnitude greater than the characteristic wavelength of the corrugations. The tendency to produce uniform fuzz versus bundles is highly influenced by the surface grain orientation, further verification on the role of surface kinetics in developing nano-tendils. This shows the collective range of surface diffusion in nano-tendril growth. Further development of the ability to tune the surface response with ion bombardment will lead to advancements in surface treatments more widely applicable than for the mitigation of undesired fuzz growth in fusion energy devices. Extension of this technique to other metals is straight forward and could be considered for semiconductors, as well.

7 Impact of helium ion energy modulation on tungsten surface morphology and nano-tendril growth

As shown in Chapter 6, time-modulated helium (He) ion energy (e.g. V_{Bias} = -50 + 25·sin($2\pi f_{RF}$·t), f_{RF} = 13.56 MHz) is demonstrated to strongly affect the development of tungsten (W) surface morphology that results from He plasma irradiation in the DIONISOS linear plasma experiment. Nano-tendril bundles (NTBs), which appear as isolated "islands" of nano-tendrils, can rapidly grow on an otherwise smooth W surface. This is in contrast to previously seen full-surface coverage of nano-tendril growth known as "fuzz". When tall NTBs form, less than 15% of the surface contains, or is covered by, nano-tendrils. The NTB surface coverage changes with growth conditions and the total volume of nano-tendrils in the NTBs is observed to be up to a factor of 16 larger when fuzz is grown. All these observations indicate that long-range W surface transport underlies nano-tendril formation.

In this chapter, the parameter space in which these new isolated structures are observed is explored. Surface temperature 870–1220 K, the DC bias potential -30 to -70 V, and the ion flux density 4.4 x 10^{21}–1.1 x 10^{22} He·m^{-2}·s^{-1} were varied in the experiments. NTBs form at similar conditions as fuzz with the critical difference being the RF modulation of the ion energy bombarding the W, another indication of the importance of W surface transport. Mass loss measurements indicate an effective net erosion with a yield of 1–8 x 10^{-4} W/He ion when NTBs form; erosion that is not attributable to chemical or physical sputtering by He or impurities in the plasma. The erosion is correlated to the NTB growth, based on post-exposure inspection by electron microscopy indicating that NTBs are prone to loss from the surface. NTB growth is compared to the empirical growth-erosion model of fuzz, showing NTBs grow up to a factor of 100 times taller than the expected fuzz layer depth under DC bias conditions. Insights into nano-tendril growth provided by this new growth regime are discussed. Strategies to mitigate W fuzz growth may inadvertently result in rapid localized nano-tendril bundle growth with a higher probability of dust and particulate release.

The assessment of NTB growth shown in this chapter was presented at the 26th IAEA Fusion Energy Conference and will be published in the journal Nuclear Fusion [125].

7.1 Measuring mass loss in W samples

The samples were weighed before and after He plasma exposure with a Sartorius ME36S microbalance that has a precision of 1 μg. The mass loss data are converted into net erosion yields using the full surface area and the total collected charge of the sample. To check if there is systematic mass loss in the experiment other than from plasma exposure, the mass change was measured on two samples, one freshly polished and one with a 1 μm thick layer

of W fuzz, which were mounted on the sample holder and annealed at 1220 K for 1 hour in vacuum. The smooth and W fuzz samples had a mass loss of 2 and 44 μg, respectively. The smallest mass loss measured after a W sample was exposed to He plasma with a DC bias of -50 V to a fluence of 5.78 x 10^{25} He·m^{-2}, was 833 μg. An uncertainty floor of 5% in the net erosion yields is taken as the mass loss measured from the annealed W fuzz sample over the plasma exposed sample. It should be noted that in previous PISCES studies [28] that grew uniform fuzz, no net erosion observed on samples. Therefore, besides their role in illuminating the underlying mechanisms for nano-tendril growth, the NTBs may play an important practical role in enhancing W mass loss in applications like fusion.

The growth-erosion model of Petty et al. [22] was used to calculate expected W fuzz layer thicknesses under DC bias conditions given the sample temperature, exposure fluence, and measured net erosion yield. From their model, the expression for the thickness of the W fuzz layer, *z*, as a function of the He fluence, Φ, is derived as,

$$z(\Phi) = \frac{C}{2\epsilon}\left(\mathrm{W}\left[-\exp\left(-\frac{2\epsilon^2}{C}(\Phi - \Phi_0) - 1\right)\right] + 1\right) \tag{7.1}$$

where C is the temperature-dependent growth parameter in units of m^4, ϵ is the erosion parameter in units of m^3 determined from the measured net erosion yield with equation (2), Φ_0 is the incubation fluence in units of m^{-2}, and W[$\cdots$] is the principal branch of the Lambert W function. The growth parameter is assumed to follow an Arrhenius relation and is determined from Baldwin and Doerner [26] by converting their data from *z (height)* versus *t* to *z* versus Φ using the flux density stated in their experiment. It is assumed there was no net erosion in their experiments from which the Arrhenius relation is derived by considering the later experiments on W fuzz growth they conducted with similar exposure conditions [28], for which they conclude there is not mass loss under He irradiation below the sputtering threshold within their experimental uncertainties. The pre-exponential factor and activation energy for the growth parameter were calculated with data for surface temperature, T_S, at 1120 K and 1320 K. At a higher temperature of 1400 K in W fuzz growth experiments by Kajita *et al.* [60], which are also stated to be free from particle loss, the W fuzz growth rate was lower than at the lower temperature experiments of Baldwin and Doerner, counter to the Arrhenius relation assumption. This may be due to the increased annealing rate as the temperature increases. The temperature range of this study is 870-1220 K, so the competition of growth and disintegration of nano-tendrils is assumed to be in the same ratio as for the Baldwin and Doerner measurements. The erosion constant is given by the expression,

$$\epsilon = \frac{m_{\mathrm{W}}}{\rho_{\mathrm{W}}(1-p)}Y \tag{7.2}$$

where m_{W} and ρ_{W} are the atomic mass and mass density of W, respectively, p is the porosity of the W fuzz layer, and Y is the net erosion yield measured in the experiment. The incubation fluence has been reported to be in the range of 1.5–4 x 10^{24} He·m^{-2} for surface temperatures and flux densities similar to the ones used in this work [22]. All of the exposures in this study have been carried out to a He fluence of at least 2x10^{25} He·m^{-2}, so the

exact incubation fluence and its dependence on temperature or ion energy is not important. The porosity is approximated as 0.85, based on micrograph analysis of NTB and W fuzz growth.

Tungsten fuzz and NTBs were imaged using a Helios NanoFab 600 scanning electron microscope (SEM) equipped with a focused-ion beam (FIB) mill. Fuzz layer thicknesses were measured after milling with the FIB and the heights and widths of the NTBs were measured from the micrographs using image processing software. An example of a NTB from a sample grown with the surface temperature of 1020 K, a DC bias of -50 V resulting in an average ion energy of 64 eV, and ion flux density of 1.1 x 10^{22} $He \cdot m^{-2} \cdot s^{-1}$ to a He fluence of 5.8 x 10^{25} $He \cdot m^{-2}$ is shown in Fig. 7-1a at a viewing angle of 52° from the surface normal. The NTBs were counted and sized on low magnification micrographs to gather information on a large population at the center of each sample. The low magnification surface area was typically 1-2 mm^2. The NTB base area is approximated as a circle with a diameter equal to the width measured in the micrograph. The height is the distance measured perpendicular from the widest portion of the base to the top of the NTB, taking into account the viewing angle is 52° from the normal direction of the sample. The scatter plot of NTB height versus width for all exposure conditions in this work that resulted in NTB growth is displayed in Fig. 7-1b. The trend in height is very close to linear with width, with the height approximately equal to the width across the tested exposure conditions. Therefore relative surface coverage of the NTBs can be used to calculate the total volume/mass of nano-tendrils present in the NTBs. The average NTB height for each exposure was compared to calculated W fuzz layer depths using the empirical relationship in Eqn. (7.1). The surface coverage of NTB growth normal to the surface is calculated as the sum of all individual NTB base areas divided by the total surface area depicted in the micrograph.

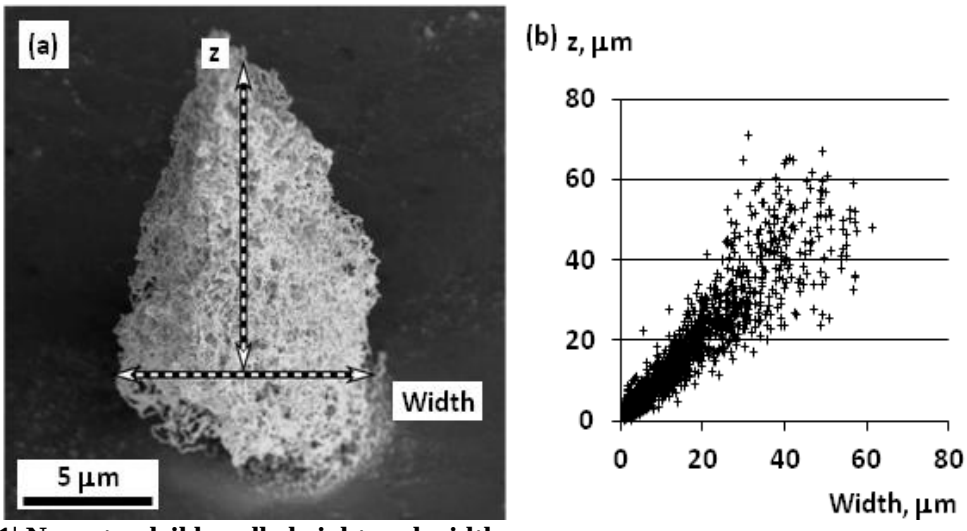

Figure 7-1| Nano-tendril bundle height and width.
(a) SEM image of W nano-tendril bundle after exposure to He plasma with a flux density of 1.1 x10^{22} $He \cdot m^{-2} \cdot s^{-1}$ to a fluence of 5.78 x 10^{25} $He \cdot m^{-2}$. The surface temperature was 1020 K The DC bias was -50 V with a RF component of the bias set to +/- 25 V at 13.56 MHz. The viewing angle is 52° from normal. (c) Height, z, versus width for all NTBs measured for the various exposure conditions of this work. NTBs smaller than 1 µm were not resolved.

7.2 Nano-tendril bundle size and coverage change with temperature

The changes in surface morphology as the result of changing the surface temperature while keeping the same exposure conditions of Fig. 7-1a can be seen in Fig. 7-2a, 7-2b, and 7-2c, for which the surface temperatures were 870 K, 1020 K, and 1220 K, respectively, with an uncertainty of +/- 50 K. In all these exposures the ion energy was modulated at 13.56 MHz +/- 25 V. The average size of the NTBs and the number density of NTBs increase when the temperature increases from 870 K to 1020 K. This follows the trend that the W fuzz growth rate increases with increasing temperature in this temperature range [26]. The surface-averaged areal density of NTBs increased with temperature, from 60 mm^{-2} at 870 K to 240 mm^{-2} to 1020 K, for NTBs larger than 1 μm in width. This increase in the number density could indicate that the nucleation mechanism is temperature dependent, with an increase in the nucleation rate with temperature. However, since the micrographs are of low magnification, NTBs smaller than 1 μm and single nano-tendrils are not represented by these data. Another possibility for the increase in number density is an increased growth rate leading to a higher number of NTBs that grow larger than 1 μm for this He fluence.

When the surface temperature increases from 1020 K to 1220 K, the surface is fully covered with nano-tendrils, which, from our earlier definition, would constitute W "fuzz" growth. However, the W fuzz growth of Fig. 7-2c is not uniform, but undulating, with peaks and valleys, even though the initial surface was smooth. The 1220 K sample surface morphology is shown in higher magnification in Fig. 7-3a, and a cross section of the undulating W fuzz is shown in Fig. 7-3b. The thin portions of fuzz measure near 1 μm in thickness while the peaks reach heights up to 5 μm normal to the surface. Therefore it appears as though isolated NTB growth was initiated in the 1220 K case which then reached ~100% coverage, where a high number density of NTBs on the surface resulted in restricted growth, i.e. the bundles blended into each other. This observation confirms that the fuzz and NTBs are really just different topological manifestations of the same growth mechanisms and that the main difference that separates W fuzz from NTB growth is the nucleation. During the incubation period prior to W fuzz and NTB growth, corrugation patterns form with the characteristic distance between corrugation ridges on the order of 10 to 1000 nm [59,70,71], depending on grain crystal orientation and surface temperature. Nano-tendrils that nucleate at the beginning of W fuzz growth are thought to follow directly from the corrugation pattern since the characteristic distance between nano-tendrils is approximately the same as the corrugation wavelength. The nucleation density of nano-tendrils in W fuzz growth is high due to the short corrugation wavelengths, resulting in a short lifetime for W adatoms migrating on the surface. This ultimately leads to slower growth of each nano-tendril in W fuzz growth. Under ion energy modulation, some form of mitigation of nano-tendril nucleation has occurred, leading to a situation where there is saturation of He bubbles or W adatoms at the surface. A nano-tendril that nucleates in this environment could grow faster than in the case of a higher nucleation rate, up to the point of growth being diffusion-limited. Therefore, the NTBs that were observed might be a form of Brownian trees. The high temperature case here and W fuzz growth in general, may be reaction-limited aggregation.

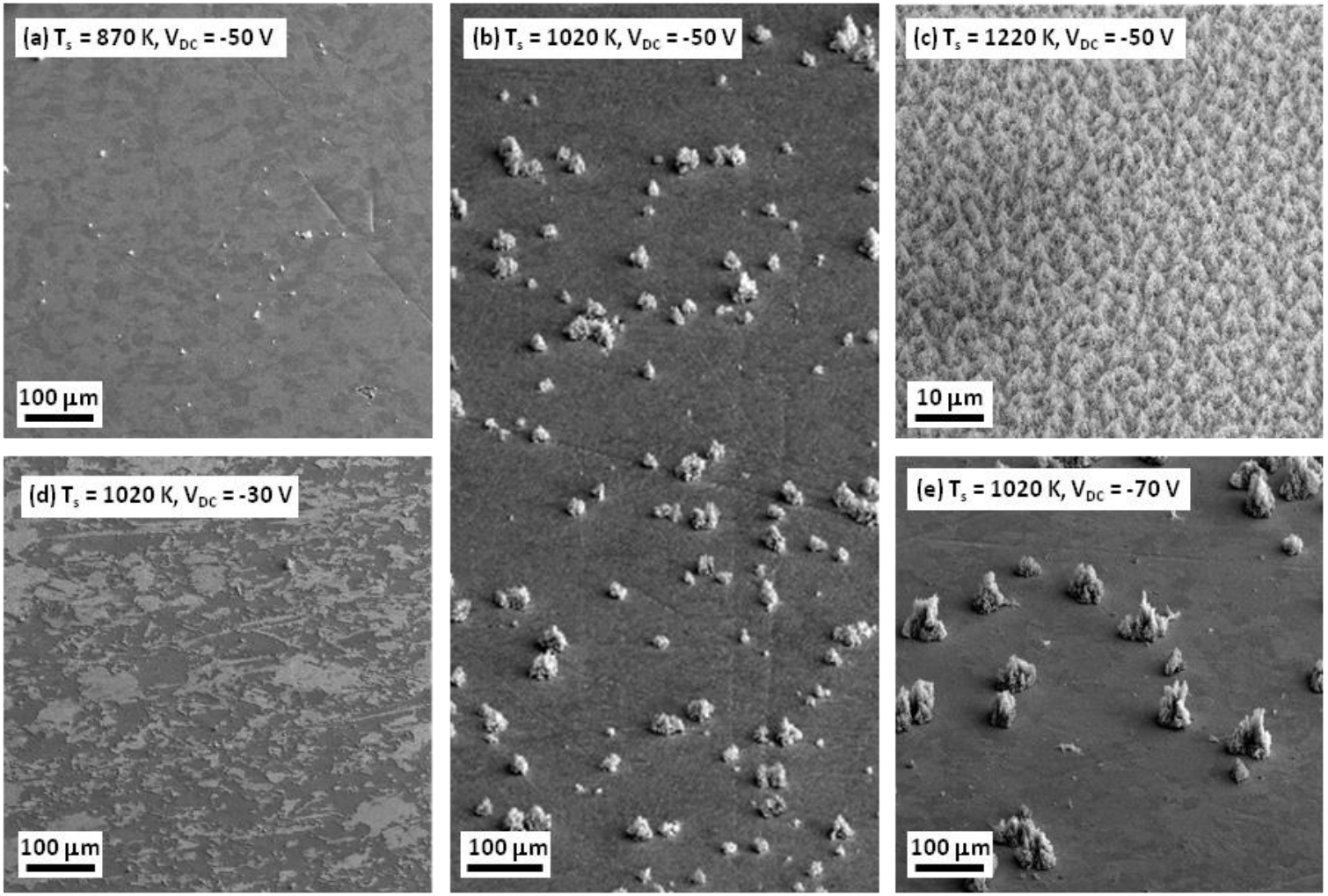

Figure 7-2 | Nano-tendril bundle growth under different conditions.
SEM images of W after exposure to He plasma with modulated ion energy with a He flux density of 1.1 x 10^{22} He·m^{-2}·s^{-1} to a fluence of 5.78 x 10^{25} He·m^{-2}. The RF component of the bias was set to +/- 25 V at 13.56 MHz. The surface temperature and DC bias were (a) T_S=870 K, V_{DC}=-50 V, (b) T_S=1020 K, V_{DC}=-50 V, (c) T_S=1220 K, V_{DC}=-50 V, (d) T_S=1020 K, V_{DC}=-30 V, and (e) T_S=1020 K, V_{DC}=-70 V. The viewing angle is 52° from normal.

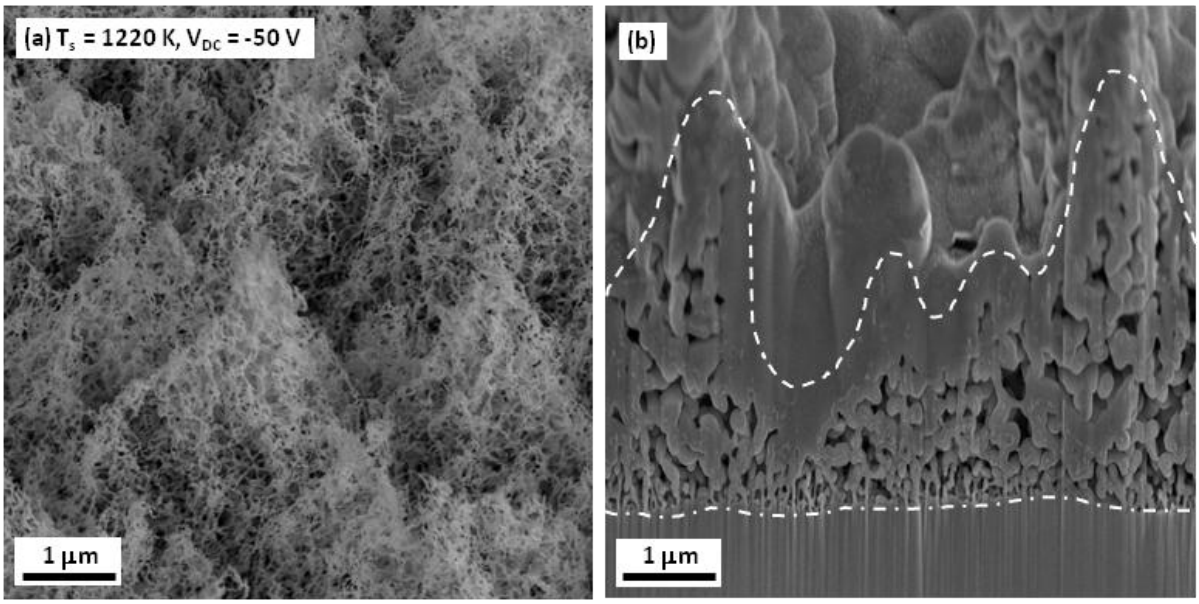

Figure 7-3 | Undulating tungsten fuzz growth.
(a) Higher magnification SEM images of the sample in Fig. 7-2c. The viewing angle is 52° from normal. (b) Cross section milled by FIB of the surface shown in (a). The dashed line depicts the approximate height of the nano-tendril layer measured from the surface, which is depicted with the dashed-dotted line.

7.3 Mass loss measurements

The surface morphology shown in Fig. 7-3a looks similar to that shown by Noiri *et al.* [20] for similar surface temperature, in which they conducted W fuzz growth experiments under erosive conditions, that is, for incident He ion energies of 200-500 eV. The threshold energy for physical sputtering of W by He is approximately 125 eV [15]. The upper energy edge of the IEDF of the He exposure resulting in the sample shown in Fig. 7-3a was near 100 eV, while the time-averaged ion energy was 64 eV, so physical sputtering by He is not likely, yet mass loss is still measured. The change in mass with respect to exposure fluence of W samples with an applied RF bias modulation is shown in Fig. 7-4a for plasma discharges with different flux densities and keeping the sample temperature fixed at 1020 K. The mass loss is near linear with exposure fluence for both fluence scans, and the net erosion yield is lower for the lower flux density exposures. At a fixed flux density and exposure fluence, the mass loss measured after varying the sample temperature is shown in Fig. 7-4b. Also shown in Fig. 7-4b are the mass loss measurements from samples exposed with no applied RF bias modulation, which resulted in uniform W fuzz growth. The mass loss decreased with increases in temperature for both the RF modulated and DC-only biases. If the mass loss mechanism were atomistic due to physical sputtering by impurities in the plasma, then the mass loss would not be expected to be a strong function of the surface temperature in this temperature range for W [17]. The chemical sputtering from a large oxygen (O) impurity in the plasma, which would be most probable, would expected to have a strong temperature dependence [126,127], but the erosion yield would increase with temperature, not decrease as is observed. Also, the impurity fraction would have to be quite high to account for the amount of measured mass loss. The residual gas analyzer situated downstream of the plasma

exposure chamber shows a typical amount of residual water vapor with the ratio of the partial pressure of the A=18 to the A=4 peaks in the mass spectrum being 0.001 when the plasma is discharged. For physical sputtering, the lowest oxygen impurity fraction that is needed to account for the lowest net erosion yield of 9.4 x 10^{-5} W/He that was measured is 0.006-0.016, assuming the O IEDF to be similar to the He IEDF. There is the possibility for sub-threshold physical sputtering by He for increased temperatures [16,17], but this possibility has not been studied in depth in the literature of W fuzz research.

The reason why the net erosion yield decreased with increasing temperature may be due to surface roughening. For rough surfaces with W fuzz growth, the sputtering yield has been found elsewhere to be lower than what is expected from a smooth surface [22,128]. As the temperature increases, the growth rate of W fuzz increases, thus for either physical or chemical erosion, the increasing surface roughness with temperature could result in lower net erosion yields. However, atomistic sputtering was ruled out as a source of the mass loss. Since mass loss was measured in all cases and the erosion mechanism was not pinned down, NTB growth relative to W fuzz growth was considered.

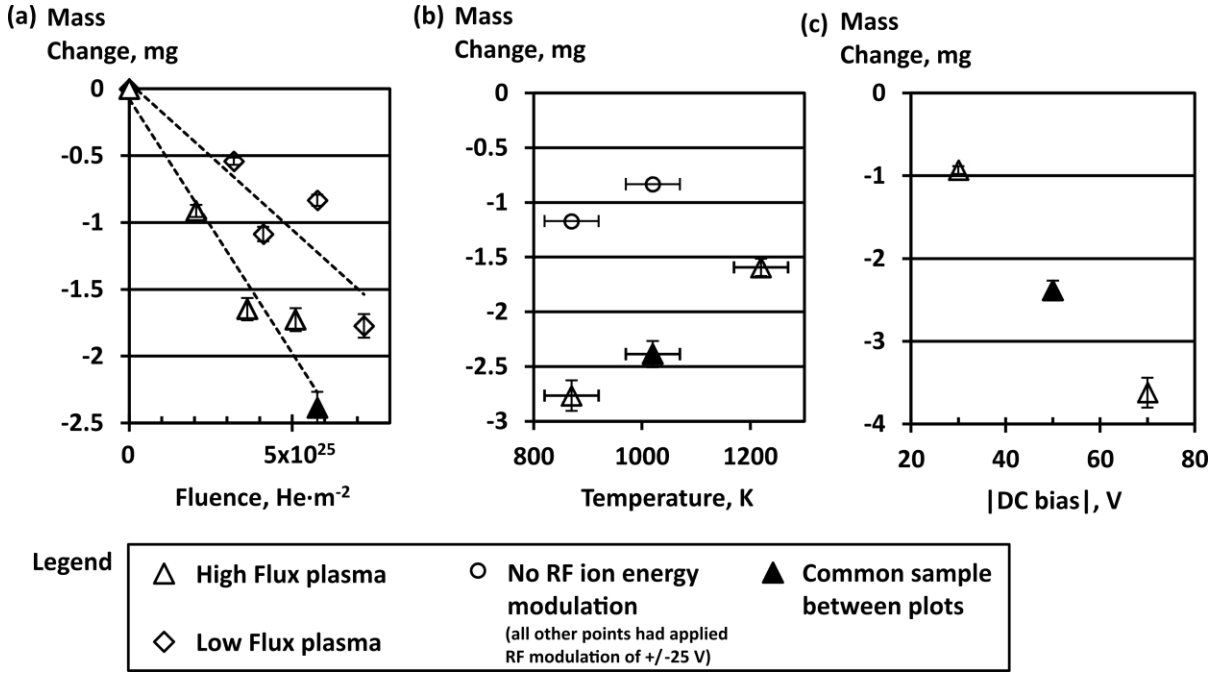

Figure 7-4 | Mass loss measurements.
Change in mass measured of W samples after exposure to He plasma plotted with respect to a) ion fluence for two ion flux densities, b) surface temperature, and c) DC bias. The low flux and high flux plasma had ion flux densities of 4.4 x 10^{21} He·m^{-2}·s^{-1} and 1.1 x 10^{22} He·m^{-2}·s^{-1}, respectively. A common sample is used in each plot. Its value indicates the fixed exposure values in the different plots. For example, in (c) where DC bias is varied, the fluence is 5.78x10^{25} m^{-2} from (a) and the temperature is 1020 K from (b).

The mass loss findings can be summed up in the following:

1. The presence of NTBs appears to increase mass loss compared to more uniform fuzz, where erosion is in fact often minimal or zero.

2. The loss mechanism is unlikely to be physical sputtering because the average and modulated He ion energies are below the threshold, yet substantial effective yield of 10^{-4} are measured.

3. Thermal/chemical removal is unlikely because the mass loss decreases with increase in temperature and the oxygen impurity content is too low to explain the loss rate.

These observations motivate an examination of how the NTBs grow since an obviously large difference between NTB and W fuzz growth is the much greater heights from the surface that are reached by the NTBs.

7.4 Comparison of tungsten fuzz layer thickness and NTB height versus temperature

When full coverage of nano-tendril growth is obtained, Eqn. (7.1) reproduces our W fuzz layer thickness after exposures, even if ion energy modulation effects vary. In Fig. 7-5, the W fuzz layer thicknesses measured from samples exposed at different surface temperatures and different ion energy modulation conditions are compared to the results of using Eqn. (7.1) to calculate the W fuzz layer thickness from only the surface temperature and net erosion yield taken as inputs. The calculation agrees within the errors of the measurement. The two lower temperature samples were exposed with low ion energy modulation, with peak-to-peak variations less than 20 eV due solely to fluctuations in the plasma potential. However, the high temperature sample is that of Fig. 7-2c and 7-3, which had an applied RF bias modulation of +/- 25 V. The thicknesses plotted in Fig. 7-5 are the average thicknesses. The error bars on the high temperature point are much larger than the lower temperature points because of the undulating thickness shown in Fig. 7-3b. Nonetheless the average tendril height agrees with the trends for uniform fuzz growth. This indicates that even for the sample of Fig. 7-3b, which appears to be in a stage of transitioning from isolated NTB to more uniform growth, the underlying mechanisms of NTB and fuzz are essentially the same.

The average heights of the NTB populations from the samples with varying conditions are plotted in Fig. 7-6. The different panels of Fig. 7-6 represent slices of a 5-dimensional parameter space with the average NTB heights varying versus surface temperature, DC bias, He ion flux density, and He ion fluence. The average NTB heights are shown as triangles. The sample shown in Fig. 7-2b is taken as the reference point, from which each dimension is varied. This reference point is shown as the solid triangle on each subplot. The net erosion yield from Fig. 7-4 and surface temperatures from these exposures were used in Eqn. (7.1) to produce the points connected by the dashed lines in each subplot to be compared to the NTB height measurements.

The results in Fig. 7-6a are for the samples shown in Fig. 7-2a, 7-2b, and 7-2c with differences only in temperature. The average NTB heights are a factor of 20-50 larger than the calculated W fuzz thickness, except for the surface temperature of 1220 K, which had full coverage of nano-tendril growth and, as shown in Fig. 7-6a, matches Eqn. (7.1). So while fuzz and NTBs have common underlying growth mechanisms, their vastly different topology can result in very different structures, and thus have different consequences for their behavior and robustness in the harsh environment of the plasma bombardment.

7.5 Nano-tendril bundle size and coverage change with DC bias

The changes in surface morphology as the result of changing the DC bias while keeping the same exposure conditions and RF modulation of Fig. 7-1a can be seen in Fig. 7-2c, 7-2b, and 7-2d, for which the DC biases were -30 K, -50 K, and -70 K, respectively. For the DC bias of -30 V, there is a mixture of NTB and W fuzz growth. The change in surface morphology varies for different grains and is presumably due to the different crystal orientations of the polycrystalline sample. Others have shown that the surface restructuring that occurs during the incubation period for W fuzz growth is also dependent on the grain crystal orientation [70,71]. Even with the W fuzz growth on more than half of the surface, NTB growth that occurred on the other areas within the micrograph was included to compare to the more negatively biased samples.

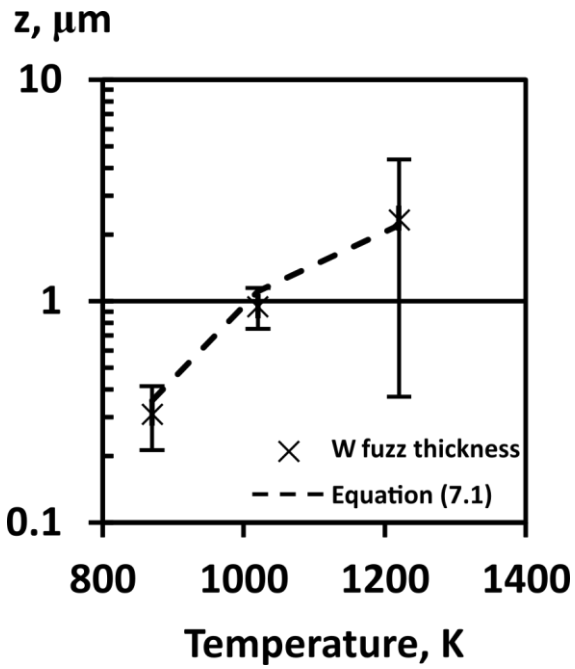

Figure 7-5 | Tungsten fuzz thickness versus temperature.
Measured W fuzz thickness (symbols) versus surface temperature after polished W samples are exposed to He plasma with a He flux density of 1.1 x 10^{22} He·m^{-2}·s^{-1} to a fluence of 5.78 x 10^{25} He·m^{-2}. The DC bias was V_{DC}=-50 V. The two lower temperature samples had no applied RF modulation of the ion energy while the high temperature sample had an applied RF modulation of +/- 25 eV at 13.56 MHz. The expected W fuzz thickness calculated using Eqn. (7.1) with the surface temperature and measured net erosion yield as inputs is shown as the dashed line.

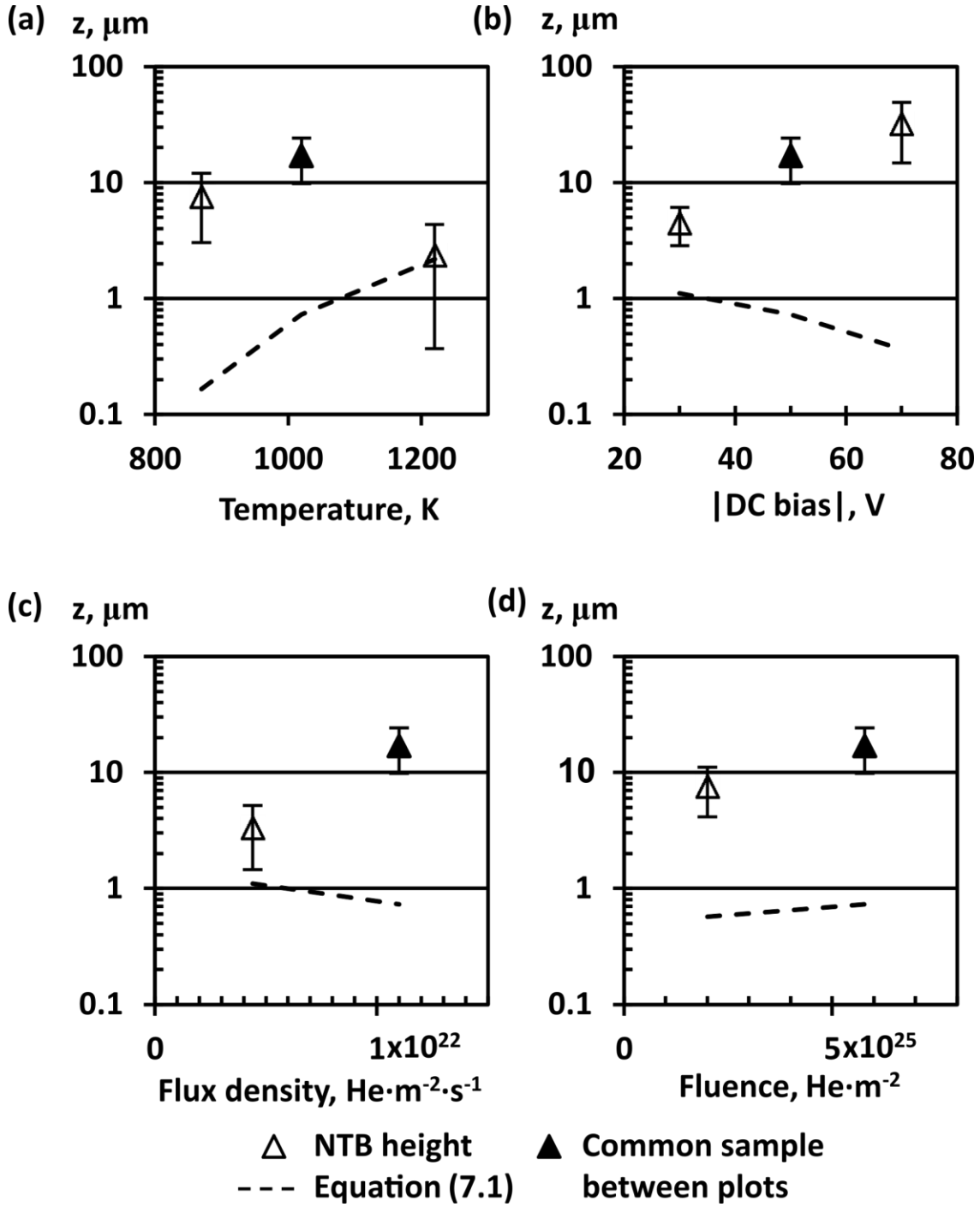

Figure 7-6 | Average nano-tendril bundle height.

Average NTB height (triangles) versus (a) surface temperature, (b) DC bias, (c) ion flux density, and (d) ion fluence. Also plotted is the empirical W fuzz layer depth (dashed line) calculated from Eqn. (7.1). A common sample is used in each plot. Its value indicates the fixed exposure values in the different plots. For example, in (b) where DC bias is varied, the fluence is 5.78 x 10^{25} He·m^{-2} from (d), the temperature is 1020 K from (a), and the flux density is 1.1 x 10^{22} He·m^{-2}·s^{-1} from (c).

The average (or DC) ion energy dependence of the NTB height is shown in Fig. 7-6b along with the calculated values for corresponding hypothetical W fuzz layers from Eqn. (7.1). The average NTB height increases strongly with the DC bias, or, equivalently, the average ion energy. The NTB size for this particular fluence, and presumably the NTB growth rate, has a clearer dependence on the average ion energy than has been shown for W fuzz growth. The calculated W fuzz layer thickness decreases in Fig. 7-6b because the measured mass loss increased with increasing DC bias, as shown in Fig. 7-6c. Atomistic sputtering cannot be a significant player when NTBs are formed because the growth trend versus DC bias is contrary to the equilibrium fuzz-sputtering model. However, there are two other important aspects of the exposure that increase with DC bias that may lead to the increase in NTB height. One of these is that He ion range increases: in the span of ion energy from 10 to 100 eV, the variation in range of the He ion into smooth W is 0.1-0.7 nm, according to SRIM [54], or 1-2.7 nm, according to Eckstein [15]. The increase in range could affect He bubble formation and the resulting nucleation sites from surface roughening. However, it must be pointed out that the large majority of the surface is essentially unaltered in topology by the He plasma exposure when NTB formation is dominant. Alternatively, and a more likely cause, is that the adatom yield will increase strongly with DC bias in this energy span [129] because the adatom yield energy dependence is expected to be similar to that of the sputtering yield just above the sputter threshold [19]. This trend is self-consistent with the increase in NTB height since a larger population of adatoms migrating across the smooth surface to NTBs will increase their growth if everything else remains constant. Clearly more investigations into these effects are needed to unravel the specific interactions here. What is clear is that the size of the NTBs increase with DC bias energy.

7.6 Nano-tendril bundle size and coverage change with flux density and fluence

The average NTB height versus ion flux density is shown in Fig. 7-6c. Others have shown there to be a flux dependence in W fuzz growth [23,130,131] which is non-linear, exhibiting a threshold effect that may be linked to an incubation fluence [22,59]. Similarly, the NTB growth rate may be proportional to the flux density in the flux density range depicted in Fig. 7-6c. However, the model behind Eqn. (7.1) is independent of flux density [22], specifically to bring the experimental results from experiments with differing flux density together. The calculated W fuzz thickness shows a decrease with ion flux density due to differences in the net erosion yield between the two flux density cases, seen in Fig. 7-6a. Again, there is a clear increase in the size of the NTBs that occurs with an increase in the net erosion yield. However, a sample exposed under the same conditions, but without ion energy modulation, resulted in W fuzz and similar mass loss. This result confirms that there is baseline net erosion during He plasma exposure in DIONISOS that is independent of NTB growth even when the He ion energy is below the threshold for physical sputtering, as was discussed in section 7.3.2. Though this inherent erosion mechanism cannot be addressed in this work, it is still clear that there is an increase in net erosion yield that is correlated with NTB growth. While admittedly qualitative, this trend also ties the magnitude of adatom migration to the formation of NTBs. At higher flux density, the time-averaged population of surface-collision induced adatoms should increase, increasing the NTB height growth rate, making more NTBs prone to full removal from the surface.

The NTB average height for the high flux density case, when exposed to only 2 x 10^{25} He·m^{-2}, is shown in Fig. 7-6d. The NTB size increases with increasing fluence. Also, the areal density of NTBs increases from 130 mm^{-2} to 193 mm^{-2}. Although there are only two fluence cases for these specific He plasma conditions, a growth parameter can be derived using the average NTB height, net erosion yield, and fluence. For a first order approximation, the erosion yield can be neglected, since it has even less influence on the low surface coverage of the NTBs. Fitting these two points to the equation $z(\Phi)=[C(\Phi-\Phi_0)]^{1/2}$ [22] yields a growth parameter, C = 6.09x10^{-36} m^{-4}, and an incubation fluence, Φ_0 = 1.04x10^{25} He·m^{-2}. As discussed in section 7.3.1, the NTB growth may be an example of diffusion-limited growth. If the growth parameter is translated into a diffusion coefficient, D, using the expression $C = 2D/\Gamma$ where Γ is the flux density, then the diffusion coefficient is D = 2.74x10^{-14} $m^2 \cdot s^{-1}$. If the NTB growth is truly diffusion-limited in these exposures, then the derived value of D represents an upper limit to the growth of nano-tendrils in general at 1020 K.

7.7 Comparison of mass relocated for NTB and tungsten fuzz growth

The ratio of the total mass of the NTBs and the total mass of the expected W fuzz layer gives a comparison of the mass that has been relocated on the surface in both growth regimes, assuming the porosity of W fuzz and NTBs are the same given their highly similar local structures. The mass contained in a hypothetical W fuzz layer is given as the W fuzz layer thickness calculated from Eqn. (7.1) multiplied by the area of the micrograph and the mass density of W.

In some cases, the amount of mass contained in the NTBs, even at lower surface coverage, is equal to the amount of mass of a hypothetical W fuzz layer, as shown as the solid triangle in Fig. 7-7, for the same common sample referred to in Fig. 7-1a, 7-2b, 7-6, and 7-6. This is possible if long range diffusion underlies NTB growth given the large separation of the NTBs seen in Fig. 7-2b. For lower flux density, temperature, or fluence, the ratio of mass in NTBs to fuzz decreases by an order of magnitude or more, shown in Fig. 7-7a, exhibiting the strong role of surface kinetics in NTB growth. Additionally, the amount of mass available for NTB growth can be substantially more, as is apparent from Fig. 7-7b, in which the ratio of mass in NTBs versus that in W fuzz reaches up to 16 when the DC bias increases. This remains highly consistent with the idea that in NTB formation the presence of He-ion induced adatoms is dominating the migration of W. If the NTBs remain isolated from each other, then the total volume of W atoms that can migrate and relocate on very large (tall) NTBs can increase dramatically. Conversely the volume can be decreased significantly if ion energy modulation is minimized…these all provide possible strategies to control the volume of nano-tendrils.

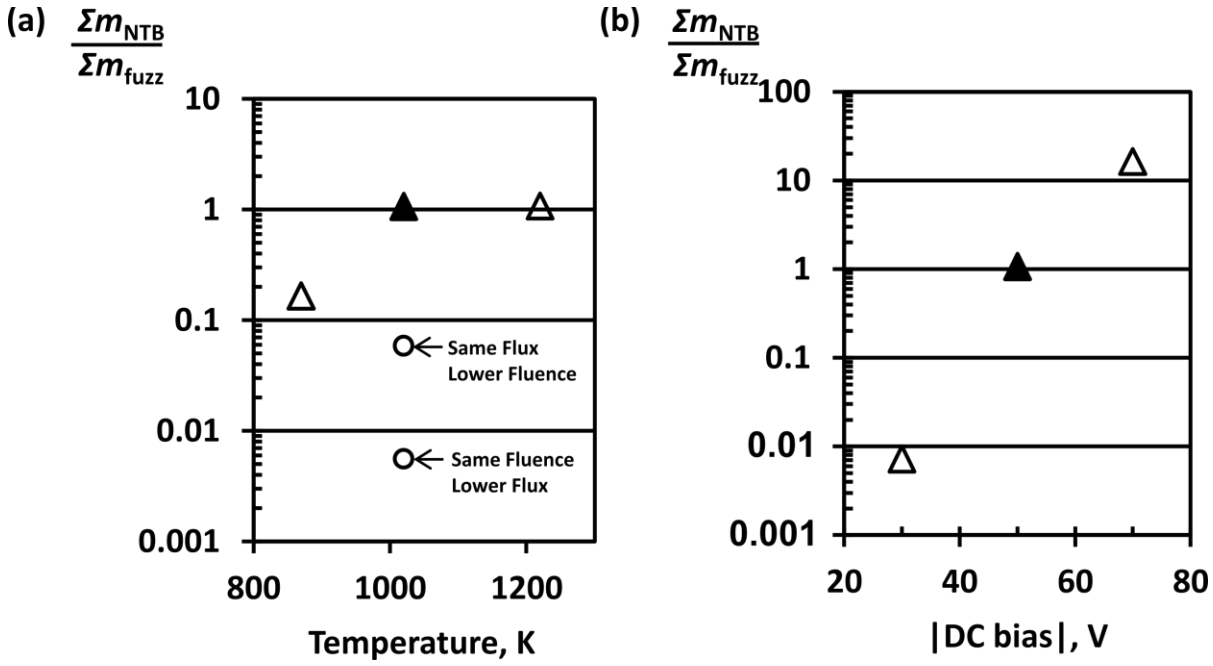

Figure 7-7 | Comparison of relocated mass.

Ratio of the amount of mass contained in the NTBs on the surface of W after exposure to He plasma to the amount of mass contained in the corresponding hypothetical W fuzz layer calculated from Eqn. (7.1) for varying (a) temperature and (b) DC bias. Also shown in (a) are lower fluence and flux density samples plotted as open circles and annotated accordingly. The solid triangle represents the common sample between the two plots with a He flux density of 1.1 x 10^{22} He·m^{-2}·s^{-1} to a fluence of 5.78 x 10^{25} He·m^{-2}. The RF component of the bias was set to +/- 25 V at 13.56 MHz.

7.8 Limits to NTB growth and RF ion energy modulation

It is appropriate to consider the possible links between mass loss and NTB size. If there is increase in net gross erosion, then this increases the atomistic release of W from the surface, providing, in principle, a larger supply of W vapor available to redeposit locally on NTBs. However, as stated before, the W ionization mean-free-path from either electron impact or charge exchange is large. The electron impact ionization cross section at 4 eV and the He electron capture cross section in the energy range of 10-100 eV are both approximately 10^{-19} m^2 [99,132]. This makes the shortest ionization mean-free-path for W on the order of 1 cm, while the Debye length is 15 μm, so the W that is released from the surface is effectively lost from the sheath and there would be no reason to expect preferential redeposition on NTBs. However, the NTBs themselves could be a source of mass loss if they become unstable and detach from the surface. The height of the NTBs can become comparable to the sheath thickness. The large, metallic protrusion that is minimally attached to the surface may be susceptible to repulsive electrostatic forces. It is possible that the NTBs are unstable at these large heights/sizes and break from the surface. The surface-averaged areal density of NTBs decreased with DC bias, from 193 mm^{-2} at -50 V to 137 mm^{-2} at -70 V, for NTBs larger than 1 μm in width. The decrease in number density supports the idea of entire NTBs being lost from the surface once they become too large. Post-exposure microscopic inspection of the surface reveals what appear to be clusters of nano-tendrils on the surface that are not clearly

attached to the surface. Shown in Fig. 7-8 is an example of one of these fragments. This is clear evidence that the entire NTB structures can be removed from the surface.

Since net erosion yields on the order of 10^{-4} W/He do not have a large impact on the average NTB height, the upper limit to NTB height may be determined by the sheath thickness. The Debye length in the high flux density plasma was ~15 μm, which is on the order of the larger average NTB heights shown in Fig. 7-6. Additionally, the grain size for these samples is on the order of 10 μm. The NTBs originate along grain boundaries and also within grains. For large NTB sizes, as in Fig. 7-2b and 7-2e, the lateral size of the NTB becomes comparable to the grain size. The polycrystalline nature of the material and the anisotropic properties of the surface migration may also contribute to limiting the NTB growth.

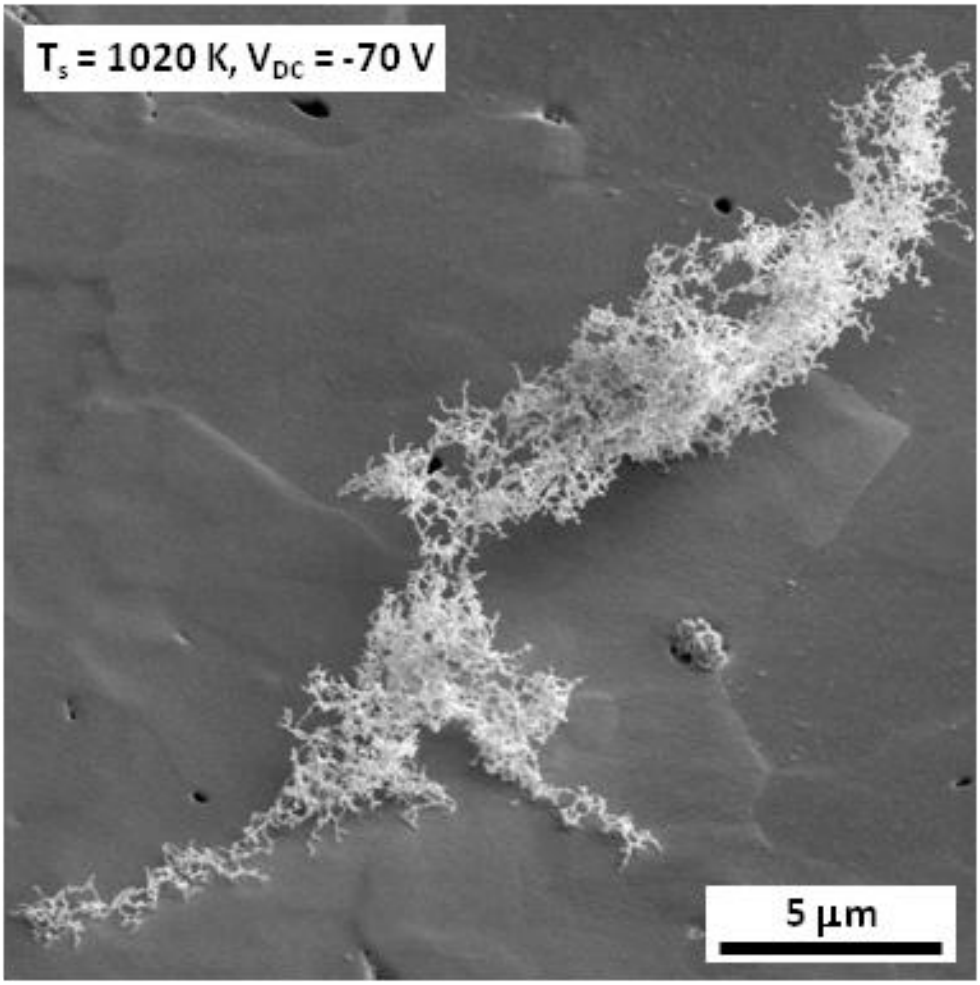

Figure 7-8 | Nano-tendril bundle fragment.
SEM image of a fragment of a NTB lying on the surface of W after exposure to He plasma with a He flux density of 1.1 x 10^{22} He·m^{-2}·s^{-1} to a fluence of 5.78 x 10^{25} He·m^{-2}. The RF component of the bias was set to +/- 25 V at 13.56 MHz. The surface temperature and DC bias were T_S=1020 K and V_{DC}=-70 V. The viewing angle is 52° from normal.

The RF time scale for these exposures is $1/f_{RF}$=1/13.56 MHz = 73.75 ns. In order for the surface to respond on this time scale, the mobile units that underlie the reformation of the

surface must be affected by ion energy modulation within this time period. The diffusivity of He in W at a temperature of 1000 K is on the order of 2 x 10^{-8} $m^2 \cdot s^{-1}$ [133,134]. Since the diffusivity represents the displacement squared per unit time, taking the elapsed time as one RF period, then the characteristic displacement that the He "wanders" through is 38.4 nm. The He bubble density in He implanted W at a temperature of 1000 K is on the order of 10^{23} bubbles$\cdot m^{-3}$ [135], making the inter-bubble distance approximately 21.5 nm, which is very close to the average displacement the diffusing He would experience on the RF time scale. Thus, it is conceivable that the ion energy modulation could affect He diffusion between bubbles. However, as mentioned earlier, it is not clear how the magnitude of the He ion energy would affect the implantation of the He or distribution of He bubbles upon implantation in the energy range of this experiment. Similarly, the diffusivity of W adatoms on bulk W at a temperature of 1000 K is on the order of 8.5 x 10^{-12} $m^2 \cdot s^{-1}$ [109], giving the characteristic distance travelled by W adatoms on the RF time scale as 0.79 nm. This distance is comparable to 2 jump distances for W adatoms on a W lattice, making it also possible that W adatom diffusion can be affected on RF time scales. As conjectured before, if the adatom yield is strongly dependent on the He ion energy in this range, possibly substantiated by the energy dependence of the NTB growth rate in Fig. 7-4b, then an ion energy swing of +/- 25 eV could have a substantial impact on the W adatom yield and subsequent surface kinetics.

More information about the growth kinetics might be attained if different frequencies are investigated. There has to be a transition in NTB versus W fuzz growth at some lower frequency. Variations in the incident ion energy have not shown a strong difference in W fuzz growth, except as a threshold. At a low enough frequency, the variation in incident ion energy would present a quasi-steady state irradiation of W, resulting in W fuzz. As the frequency is increased, NTB growth would start to dominate. If the frequency is increased even further, then the inertia of the diffusing species or the irradiating ions would be too great to follow the modulation, and the resulting surface morphology would be more like W fuzz grown with the average ion energy or average plasma potential.

7.9 Summary

Uniform W fuzz growth can be suppressed with ion energy modulation at 13.56 MHz. However, the nano-tendril growth that eventually occurs under ion energy modulation is in the form of nano-tendril bundles. Nano-tendril bundles can grow much higher from the surface for a given He fluence than W fuzz. The nano-tendril bundle growth rate increases for increasing average ion energy, surface temperature, and ion flux density. For a flux density of 1.1 x 10^{22} He$\cdot m^{-2} \cdot s^{-1}$, nano-tendril bundle growth is observed for temperatures between 870-1220 K. The lower temperature is similar to the lower threshold for the observance of W fuzz. At the upper temperature, W fuzz growth resumes, presumably due to saturation of the NTB growth surface coverage. The large average size and distances between the NTB structures suggest long range transport of mass to form the NTB structure. The NTB structure and growth dependences provide evidence of surface migration by adatoms produced by He ion impact that is mediated on the RF time scale.

8 Conclusion

8.1 Key learnings

Elastic Recoil Detection (ERD) was used for the first time to measure the helium (He) concentration in tungsten (W) that has developed the characteristic nano-tendril morphology called W fuzz. In particular, the He concentrations of various samples from PILOT-PSI and PISCES were measured to be in the range of 1-4 at. % despite a surface temperature variation of ΔT_s = 2000 K among the samples and various He fluences across three orders of magnitude. This is a high value when compared to solubility of He in W, but does not represent the necessary concentration to support void creation and fuzz development by dislocation loop-punching and bursting bubbles. The individual He concentration depth profiles of fully developed W fuzz show the He concentration to be uniform through the measurable depth, which varies with the porosity of the W fuzz layer. By monitoring He depth profiles, ERD is an indirect method to follow W fuzz development.

In situ ERD analysis was developed to investigate for the first time the role of the dynamic He concentration in the development of the nanostructuring of W surfaces that may be present in future fusion experiments. The adverse conditions of the DIONISOS plasma exposure chamber were mitigated by proper shielding of the solid state charged particle detector and through data analysis practices.

The He concentration was found to saturate at levels of 1 – 7 at. %, which depends on the specific exposure conditions. There is also an incubation period before the He reaches saturation that is dependent on the flux density. The dynamic measurement provides a basis for models on how much the average He concentration can be in evaluating the mechanisms involved in the nanostructuring of the W surface.

Helium agglomeration and elevated surface temperature are the critical ingredients in the process that results in W fuzz from He irradiation. Current theories and modeling suggest that the nucleation of high pressure, high density He bubbles at trapping sites progress into clusters, deforming the W surface and providing the initial deformation that leads to tendril growth. The results in this thesis introduce a constraint on modeling this process, namely, that the overall He concentration of evolving layers both during and after He irradiation remains on the order of a few atomic percent. The *in situ* results also clearly eliminate the He bubble pressure model for explaining nano-tendril growth.

A new variation of the typical W fuzz, that is observed in many international laboratories, was discovered in the DIONISOS exposure chamber. The new variation contains typical W fuzz nano-tendrils, but the nano-tendrils are concentrated in discrete bundles that are smaller

than the grain size. The new W fuzz structures, single nano-tendrils and nano-tendril bundles (NTBs), and why they appear in place of the uniform W fuzz growth provide a unique way to study nano-tendril growth in general.

Due to the resemblance of single nano-tendrils to metal whiskers in other fields of research and the omnipresent sheath electric field in almost all W fuzz growth experiments, the theories of electric field-induced nucleation and electromigration were investigated. By implementing an appropriate grid between the W sample and the He plasma, the electric field at the surface of the sample was decreased to 3 % of the electric field that would be present at the sample from the plasma sheath.

The resulting W fuzz layers grown different electric fields, namely, with direct exposure to the plasma, with a much lower electric field, and even with a low retarding electric field, are all similar in terms of their nano-tendril size and layer depth, when normalized to an empirical layer depth calculation. It is concluded that the sheath electric field does not impact the nucleation process nor the growth rate of the nano-tendrils that form when He plasma irradiates W at elevated surface temperatures.

The NTB growth was discovered while using the high power helicon wave-coupled discharge mode of DIONISOS. The grid-sample setup of the sheath electric field test was used as a grid-collector retarding field energy analyzer in the helicon mode, revealing that the ion energy distribution function (IEDF) incident on the area of the sample where the NTB and single nano-tendril growth was observed was not singular, but bimodal, suggesting the ion energy was modulated by radiofrequency sheath potential oscillations. The plasma potential oscillations vary radially in the plasma, with larger oscillation amplitudes on axis, where the NTB growth and W fuzz suppression were observed. The bimodal IEDF transitions to a monoenergetic IEDF at a radius $r = 8$ mm, where normal W fuzz growth was observed.

RF broadened IEDF and/or ion energy modulation was shown to affect the resulting surface morphology when He plasma is incident on W. By manipulating the surface kinetics through temporal modulation of the incident He ion energy, tenets of the nature of W nano-tendril growth were unveiled. The suppression of uniform fuzz growth by ion energy modulation indicates the nucleation mechanism of nano-tendril growth is sensitive to the surface kinetics. In regions adjacent to nano-tendril growth, a linear topographic instability model was applied to ion-induced corrugations with reasonable quantitative agreement. In addition to fuzz and ion-induced corrugations, isolated NTBs and single nano-tendrils that nucleate at distances many orders of magnitude greater than the characteristic wavelength of the corrugations show the collective range of surface diffusion in nano-tendril growth. Further development of the ability to tune the surface response with ion bombardment could lead to advancements in surface treatments more widely applicable than for the mitigation of undesired fuzz growth in fusion energy devices. Extension of this technique to other metals is straight forward and could be considered for semiconductors as well.

It was shown that W fuzz growth can be affected with ion energy modulation at RF frequencies. However, the nano-tendril growth that eventually occurs under ion energy modulation, NTB growth, grows much higher from the surface for a given He fluence than W fuzz, with potential of becoming a source of dust production and erosion if the NTB size becomes comparable to the sheath thickness. This is a cautionary tale of the ramifications of W fuzz mitigation without understanding the growth mechanisms. Other methods to mitigate W fuzz growth could inadvertently reroute W fuzz growth into rapid growth concentrated in widespread locations like NTBs.

8.2 Future directions

The results from this thesis followed a logical path of discovery, but each juncture could be fleshed out and are ripe with possibilities. The parameter space for W fuzz growth was somewhat limited by the capabilities of DIONISOS, but improvements to expand the parameter space would allow for further mapping of the changes in He concentration with exposure conditions. The He concentration was measured to be low enough to rule out oversaturated bubbles bursting to form W fuzz, but the dynamic measurement can be used to measure other aspects of W fuzz growth. For example, if the final W fuzz layer thickness and porosity are measured after exposure, the layer thickness evolution with time can be interpolated using the dynamic ERD spectra, since the energy axis could serve as a proxy for thickness of W. The thickness at other facilities is currently measured by growing different W fuzz samples under identical conditions, but to different exposure fluences typically spanning orders of magnitude. By using *in situ* ERD, the thickness could be measured on a much finer time scale to further constrain W fuzz growth models.

Also, *in situ* ERD has the capability to measure the concentration of deuterium (D), as well. The concentrations of hydrogen (H), D, and He could be measured simultaneous for plasmas incident on the target that contain various mixtures of these constituents. Helium in the surface has been shown to be a diffusion barrier for hydrogenic species. Details of this effect could be investigated using *in situ* ERD. The dynamic D retention has been studied before in DIONISOS, but with a different ion beam analysis technique that has higher probing depth than ERD, but with poor depth resolution. Fuel retention and isotopic exchange in the very near surface (<15 nm) could be studied with using *in situ* ERD.

Tungsten fuzz was shown to be independent of the naturally occurring sheath electric field, but higher electric fields than those that occur naturally from the sheath could be introduced that might enhance W fuzz growth. This could offer a pathway for manufacturing porous layers with much greater thickness for a given He fluence, increasing efficiency.

The parameter space of NTB growth and fuzz suppression by ion energy modulation could be investigated further. The frequency chosen in this thesis was due to the frequency of the power supply for the DIONISOS plasma antenna. One would expect there to be a lower limit to the frequency, since under DC conditions, W fuzz is shown to growth at the various ion energies studied in this thesis. There would have to be a transition from fuzz growth under DC conditions to fuzz suppression at RF conditions. How the surface morphology changes at

different frequencies would also provide more information on the role of surface diffusion in nano-tendril growth.

The topological instability model that was applied to the corrugation wavelengths that form alongside nano-tendrils can be expanded to include other effects pertinent to nano-tendril growth. These could include vacancy diffusion into the bulk for He bubble growth and nano-tendril nucleation.

REFERENCES

[1] G. Federici, C.. Skinner, J.. Brooks, J.. Coad, C. Grisolia, A.. Haasz, A. Hassanein, V. Philipps, C.. Pitcher, J. Roth, W.. Wampler, D.. Whyte, Plasma-material interactions in current tokamaks and their implications for next step fusion reactors, Nucl. Fusion. 41 (2001) 1967–2137. doi:10.1088/0029-5515/41/12/218.

[2] R.A. Pitts, S. Carpentier, F. Escourbiac, T. Hirai, V. Komarov, S. Lisgo, A.S. Kukushkin, A. Loarte, M. Merola, A. Sashala Naik, R. Mitteau, M. Sugihara, B. Bazylev, P.C. Stangeby, A full tungsten divertor for ITER: Physics issues and design status, J. Nucl. Mater. 438 (2013) S48–S56. doi:10.1016/j.jnucmat.2013.01.008.

[3] J.N. Brooks, L. El-Guebaly, A. Hassanein, T. Sizyuk, Plasma-facing material alternatives to tungsten, Nucl. Fusion. 55 (2015) 43002. doi:10.1088/0029-5515/55/4/043002.

[4] S. Takamura, N. Ohno, D. Nishijima, S. Kajita, Formation of Nanostructured Tungsten with Arborescent Shape due to Helium Plasma Irradiation, Plasma Fusion Res. 1 (2006) 051–051. doi:10.1585/pfr.1.051.

[5] G.M. Wright, D. Brunner, M.J. Baldwin, R.P. Doerner, B. Labombard, B. Lipschultz, J.L. Terry, D.G. Whyte, Tungsten nano-tendril growth in the Alcator C-Mod divertor, Nucl. Fusion. 52 (2012) 42003. doi:10.1088/0029-5515/52/4/042003.

[6] S. Kajita, S. Takamura, N. Ohno, D. Nishijima, H. Iwakiri, N. Yoshida, Sub-ms laser pulse irradiation on tungsten target damaged by exposure to helium plasma, Nucl. Fusion. 47 (2007) 1358–1366. doi:10.1088/0029-5515/47/9/038.

[7] M. de Respinis, G. De Temmerman, I. Tanyeli, M.C.M. van de Sanden, R.P. Doerner, M.J. Baldwin, R. van de Krol, Efficient Plasma Route to Nanostructure Materials: Case Study on the Use of m-WO 3 for Solar Water Splitting, ACS Appl. Mater. Interfaces. 5 (2013) 7621–7625. doi:10.1021/am401936q.

[8] S. Kajita, T. Yoshida, D. Kitaoka, R. Etoh, M. Yajima, N. Ohno, H. Yoshida, N. Yoshida, Y. Terao, Helium plasma implantation on metals: Nanostructure formation and visible-light photocatalytic response, J. Appl. Phys. 113 (2013). doi:10.1063/1.4798597.

[9] İ. Tanyeli, L. Marot, D. Mathys, M.C.M. van de Sanden, G. De Temmerman, Surface modifications induced by high fluxes of low energy helium ions., Sci. Rep. 5 (2015) 9779. doi:10.1038/srep09779.

[10] S. Kajita, T. Ishida, N. Ohno, D. Hwangbo, T. Yoshida, Fuzzy nanostructure growth on Ta/Fe by He plasma irradiation, Sci. Rep. 6 (2016) 30380. doi:10.1038/srep30380.

[11] D. Nishijima, M.. Ye, N. Ohno, S. Takamura, Formation mechanism of bubbles and holes on tungsten surface with low-energy and high-flux helium plasma irradiation in NAGDIS-II, J. Nucl. Mater. 329–333 (2004) 1029–1033. doi:10.1016/j.jnucmat.2004.04.129.

[12] S. Kajita, W. Sakaguchi, N. Ohno, N. Yoshida, T. Saeki, Formation process of tungsten nanostructure by the exposure to helium plasma under fusion relevant plasma conditions, Nucl. Fusion. 49 (2009) 95005. doi:10.1088/0029-5515/49/9/095005.

[13] M.J. Baldwin, T.C. Lynch, R.P. Doerner, J.H. Yu, Nanostructure formation on tungsten exposed to low-pressure rf helium plasmas: A study of ion energy threshold and early stage growth, J. Nucl. Mater. 415 (2011) S104–S107. doi:10.1016/j.jnucmat.2010.10.050.

[14] G. De Temmerman, K. Bystrov, J.J. Zielinski, M. Balden, G. Matern, C. Arnas, L. Marot, Nanostructuring of molybdenum and tungsten surfaces by low-energy helium ions, J. Vac. Sci. Technol. A Vacuum, Surfaces, Film. 30 (2012) 41306. doi:10.1116/1.4731196.

[15] W. Eckstein, Calculated Sputtering, Reflection and Range Values, Garching, Germany, 2002.

[16] M.I. Guseva, V.M. Gureev, B.N. Kolbasov, S.N. Korshunov, Y. V. Martynenko, V.B. Petrov, B.I. Khripunov, Subthreshold sputtering at high temperatures, J. Exp. Theor. Phys. Lett. 77 (2003) 362–365. doi:10.1134/1.1581961.

[17] R.P. Doerner, S.I. Krasheninnikov, K. Schmid, Particle-induced erosion of materials at elevated temperature, J. Appl. Phys. 95 (2004) 4471–4475. doi:10.1063/1.1687038.

[18] H. Gades, H.M. Urbassek, Molecular-dynamics simulation of adatom formation under keV-ion bombardment of Pt(111), Phys. Rev. B. 50 (1994) 11167–11174. doi:10.1103/PhysRevB.50.11167.

[19] Y. V. Martynenko, M.Y. Nagel, Model of fuzz formation on a tungsten surface, Plasma-Surface Interact. 38 (2012) 996–999. doi:10.1134/S1063780X12110074.

[20] Y. Noiri, S. Kajita, N. Ohno, Nanostructure growth by helium plasma irradiation to tungsten in sputtering regime, J. Nucl. Mater. 463 (2015) 285–288. doi:10.1016/j.jnucmat.2015.01.036.

[21] R.P. Doerner, M.J. Baldwin, P.C. Stangeby, An equilibrium model for tungsten fuzz in an eroding plasma environment, Nucl. Fusion. 51 (2011) 43001. doi:10.1088/0029-5515/51/4/043001.

[22] T.J. Petty, M.J. Baldwin, M.I. Hasan, R.P. Doerner, J.W. Bradley, Tungsten "fuzz" growth re-examined: the dependence on ion fluence in non-erosive and erosive helium plasma, Nucl. Fusion. 55 (2015) 93033. doi:10.1088/0029-5515/55/9/093033.

[23] M.J. Baldwin, R.P. Doerner, D. Nishijima, K. Tokunaga, Y. Ueda, The effects of high fluence mixed-species (deuterium, helium, beryllium) plasma interactions with tungsten, J. Nucl. Mater. 390–391 (2009) 886–890. doi:10.1016/j.jnucmat.2009.01.247.

[24] S. Kajita, T. Yokochi, N. Ohno, T. Kumano, Near Infrared Radiation from Heated Nanostructured Tungsten, Jpn. J. Appl. Phys. 51 (2012) 01AJ03. doi:10.1143/JJAP.51.01AJ03.

[25] G.M. Wright, H.S. Barnard, L.A. Kesler, E.E. Peterson, P.W. Stahle, R.M. Sullivan, D.G. Whyte, K.B. Woller, An experiment on the dynamics of ion implantation and sputtering of surfaces, Rev. Sci. Instrum. 85 (2014) 23503. doi:10.1063/1.4861917.

[26] M.J. Baldwin, R.P. Doerner, Helium induced nanoscopic morphology on tungsten under fusion relevant plasma conditions, Nucl. Fusion. 48 (2008) 35001. doi:10.1088/0029-5515/48/3/035001.

[27] D.M. Goebel, G. Campbell, R.W. Conn, Plasma surface interaction experimental facility (PISCES) for materials and edge physics studies, J. Nucl. Mater. 121 (1984) 277–282. doi:10.1016/0022-3115(84)90135-1.

[28] M.J. Baldwin, R.P. Doerner, Formation of helium induced nanostructure "fuzz" on various tungsten grades, J. Nucl. Mater. 404 (2010) 165–173. doi:10.1016/j.jnucmat.2010.06.034.

[29] J. Laakmann, P. Jung, W. Uelhoff, Solubility of helium in gold, Acta Metall. 35 (1987) 2063–2069. doi:10.1016/0001-6160(87)90034-4.

[30] H. Trinkaus, Energetics and formation kinetics of helium bubbles in metals, Radiat. Eff. 78 (1983) 189–211. doi:10.1080/00337578308207371.

[31] H. Trinkaus, B.. Singh, Helium accumulation in metals during irradiation – where do we stand?, J. Nucl. Mater. 323 (2003) 229–242. doi:10.1016/j.jnucmat.2003.09.001.

[32] E. V. Kornelsen, A.A. Van Gorkum, Study of Bubble Nucleation in Tungsten Using Thermal Desorption Spectrometry: Clusters of 2 To 100 Helium Atoms., J. Nucl. Mater. 92 (1980) 79–88. doi:10.1016/0022-3115(80)90144-0.

[33] S. Takamura, Y. Uesugi, Experimental identification for physical mechanism of fiber-form nanostructure growth on metal surfaces with helium plasma irradiation, Appl. Surf. Sci. 356 (2015) 888–897. doi:10.1016/j.apsusc.2015.08.112.

[34] S. Kajita, N. Yoshida, N. Ohno, Y. Tsuji, Growth of multifractal tungsten nanostructure by He bubble induced directional swelling, New J. Phys. 17 (2015) 1–14. doi:10.1088/1367-2630/17/4/043038.

[35] A. Lasa, S.K. Tähtinen, K. Nordlund, Loop punching and bubble rupture causing surface roughening — A model for W fuzz growth, EPL (Europhysics Lett. 105 (2014) 25002. doi:10.1209/0295-5075/105/25002.

[36] A.M. Ito, A. Takayama, Y. Oda, T. Tamura, R. Kobayashi, T. Hattori, S. Ogata, N. Ohno, S. Kajita, M. Yajima, Y. Noiri, Y. Yoshimoto, S. Saito, S. Takamura, H. Nakamura, Molecular dynamics research on formation mechanism of tungsten nanostructure induced by helium plasma irradiation, 440 (2014) 134301.

[37] S.I. Krasheninnikov, Viscoelastic model of tungsten “fuzz” growth, Phys. Scr. T145 (2011) 14040. doi:10.1088/0031-8949/2011/T145/014040.

[38] D. Trufanov, E. Marenkov, S. Krasheninnikov, The Role of the Adatom Diffusion in the Tungsten Fuzz Growth, Phys. Procedia. 71 (2015) 20–24. doi:10.1016/j.phpro.2015.08.377.

[39] S. Kajita, W. Sakaguchi, N. Ohno, N. Yoshida, T. Saeki, Formation process of tungsten nanostructure by the exposure to helium plasma under fusion relevant plasma conditions, Nucl. Fusion. 49 (2009) 95005. doi:10.1088/0029-5515/49/9/095005.

[40] K.B. Woller, D.G. Whyte, G.M. Wright, R.P. Doerner, G. De Temmerman, Helium concentration in tungsten nano-tendril surface morphology using Elastic Recoil Detection, J. Nucl. Mater. 438 (2013) S913–S916. doi:10.1016/j.jnucmat.2013.01.198.

[41] W.L. Chan, E. Chason, Making waves: Kinetic processes controlling surface evolution during low energy ion sputtering, J. Appl. Phys. 101 (2007). doi:10.1063/1.2749198.

[42] R. Ochoukov, D.G. Whyte, D. Brunner, I. Cziegler, B. LaBombard, B. Lipschultz, J. Myra, J. Terry, S. Wukitch, Investigation of RF-enhanced plasma potentials on Alcator C-Mod, J. Nucl. Mater. 438 (2013) S875–S878. doi:10.1016/j.jnucmat.2013.01.189.

[43] C. Charles, A.W. Degeling, T.E. Sheridan, J.H. Harris, M.A. Lieberman, R.W. Boswell, Absolute measurements and modeling of radio frequency electric fields using a retarding field energy analyzer, Phys. Plasmas. 7 (2000) 5232. doi:10.1063/1.1322557.

[44] T. Panagopoulos, D.J. Economou, Plasma sheath model and ion energy distribution for all radio frequencies, J. Appl. Phys. 85 (1999) 3435. doi:10.1063/1.369701.

[45] K.B. Woller, D.G. Whyte, Depth profiles of Helium and Deuterium in tungsten "fuzz’’ using Elastic Recoil Detection, in: 52nd Annu. Meet. APS Div. Plasma Phys., Chicago, Illinois, 2010. http://meetings.aps.org/link/BAPS.2010.DPP.UP9.18.

[46] J.R. Tesmer, M. Nastasi, Handbook of Modern Ion Beam Materials Analysis, Materials Research Society, Pittsburgh, Pennsylvania, 1995.

[47] M. Mayer, SIMNRA User’s Guide, Report IPP 9/113, Max-Planck-Instiut für Plasmaphysik, Garching, Germany, 1997.

[48] G.M. Wright, H.S. Barnard, Z.S. Hartwig, P.W. Stahle, R.M. Sullivan, K.B. Woller, D.G. Whyte, Plasma-surface interaction research at the Cambridge Laboratory of Accelerator Studies of Surfaces, in: AIP Conf. Proc., 2011. doi:10.1063/1.3586178.

[49] I.M. Yesil, W. Assmann, H. Huber, K.E.G. Löbner, Simulation of surface roughness effects in ERDA, Nucl. Instruments Methods Phys. Res. Sect. B Beam Interact. with Mater. Atoms. 136–138 (1998) 623–627. doi:10.1016/S0168-583X(97)00860-4.

[50] R. Behrisch, S. Grigull, U. Kreissig, R. Grötzschel, Influence of surface roughness on measuring depth profiles and the total amount of implanted ions by RBS and ERDA, Nucl. Instruments Methods Phys. Res. Sect. B Beam Interact. with Mater. Atoms. 136–138 (1998) 628–632. doi:10.1016/S0168-583X(97)00798-2.

[51] J.P. Stoquert, T. Szörényi, Determination of the number and size of inhomogeneities in thin films by ion beam analysis, Phys. Rev. B. 66 (2002) 144108. doi:10.1103/PhysRevB.66.144108.

[52] S. Kajita, N. Yoshida, R. Yoshihara, N. Ohno, T. Yokochi, M. Tokitani, S. Takamura, TEM analysis of high temperature annealed W nanostructure surfaces, J. Nucl. Mater. 421 (2012) 22–27. doi:10.1016/j.jnucmat.2011.11.044.

[53] G.J. van Rooij, V.P. Veremiyenko, W.J. Goedheer, B. de Groot, A.W. Kleyn, P.H.M. Smeets, T.W. Versloot, D.G. Whyte, R. Engeln, D.C. Schram, N.J.L. Cardozo, Extreme hydrogen plasma densities achieved in a linear plasma generator, Appl. Phys. Lett. 90 (2007) 121501. doi:10.1063/1.2716208.

[54] J.F. Ziegler, M.D. Ziegler, J.P. Biersack, SRIM – The stopping and range of ions in matter (2010), Nucl. Instruments Methods Phys. Res. Sect. B Beam Interact. with Mater. Atoms. 268 (2010) 1818–1823. doi:10.1016/j.nimb.2010.02.091.

[55] G.M. Wright, D. Brunner, M.J. Baldwin, K. Bystrov, R.P. Doerner, B. Labombard, B. Lipschultz, G. De Temmerman, J.L. Terry, D.G. Whyte, K.B. Woller, Comparison of tungsten nano-tendrils grown in Alcator C-Mod and linear plasma devices, J. Nucl. Mater. 438 (2013) S84–S89. doi:10.1016/j.jnucmat.2013.01.013.

[56] K.B. Woller, D.G. Whyte, G.M. Wright, In situ elastic recoil detection analysis of tungsten surfaces during ITER-like helium irradiation, in: 2015 IEEE 26th Symp. Fusion Eng., IEEE, 2015: pp. 1–6. doi:10.1109/SOFE.2015.7482349.

[57] K.B. Woller, D.G. Whyte, G.M. Wright, Dynamic measurement of the helium concentration of evolving tungsten nanostructures using Elastic Recoil Detection during plasma exposure, J. Nucl. Mater. 463 (2015) 289–293. doi:10.1016/j.jnucmat.2014.11.126.

[58] M. Miyamoto, D. Nishijima, M.J. Baldwin, R.P. Doerner, Y. Ueda, K. Yasunaga, N. Yoshida, K. Ono, Microscopic damage of tungsten exposed to deuterium-helium mixture plasma in PISCES and its impacts on retention property, J. Nucl. Mater. 415 (2011) S657–S660. doi:10.1016/j.jnucmat.2011.01.008.

[59] S. Kajita, N. Yoshida, N. Ohno, Y. Hirahata, R. Yoshihara, Helium plasma irradiation on single crystal tungsten and undersized atom doped tungsten alloys, Phys. Scr. 89 (2014) 25602. doi:10.1088/0031-8949/89/02/025602.

[60] S. Kajita, N. Yoshida, R. Yoshihara, N. Ohno, M. Yamagiwa, TEM observation of the growth process of helium nanobubbles on tungsten: Nanostructure formation mechanism, J. Nucl. Mater. 418 (2011) 152–158. doi:10.1016/j.jnucmat.2011.06.026.

[61] F. Sefta, K.D. Hammond, N. Juslin, B.D. Wirth, Tungsten surface evolution by helium bubble nucleation, growth and rupture, Nucl. Fusion. 53 (2013) 73015. doi:10.1088/0029-5515/53/7/073015.

[62] V.G. Karpov, Electrostatic theory of metal whiskers, Phys. Rev. Appl. 1 (2014) 1–13. doi:10.1103/PhysRevApplied.1.044001.

[63] K.B. Woller, D.G. Whyte, G.M. Wright, D. Brunner, Experimental investigation on the effect of surface electric field in the growth of tungsten nano-tendril morphology due to low energy helium irradiation, J. Nucl. Mater. 481 (2016) 111–116. doi:10.1016/j.jnucmat.2016.09.018.

[64] W. Ahmed, E.S. Kooij, A. van Silfhout, B. Poelsema, Quantitative Analysis of Gold Nanorod Alignment after Electric Field-Assisted Deposition, Nano Lett. 9 (2009) 3786–3794. doi:10.1021/nl901968e.

[65] M. Nardone, V.G. Karpov, Nucleation of metals by strong electric fields, Appl. Phys. Lett. 100 (2012). doi:10.1063/1.3703611.

[66] J.P. Barbour, F.M. Charbonnier, W.W. Dolan, W.P. Dyke, E.E. Martin, J.K. Trolan, Determination of the surface tension and surface migration constants for tungsten, Phys. Rev. 117 (1960) 1452–1459. doi:10.1103/PhysRev.117.1452.

[67] P.C. Bettler, F.M. Charbonnier, Activation energy for the surface migration of tungsten in the presence of a high-electric field, Phys. Rev. 119 (1960) 85–93. doi:10.1103/PhysRev.119.85.

[68] P.R. Schwoebel, The epitaxial growth of microprotrusions on field emitter tips, J. Appl. Phys. 64 (1988) 2359. doi:10.1063/1.341666.

[69] Z. Fu, N. Yoshida, H. Iwakiri, Z. Xu, Thermal desorption and surface modification of He+ implanted

into tungsten, J. Nucl. Mater. 329–333 (2004) 692–696. doi:10.1016/j.jnucmat.2004.04.190.

[70] N. Ohno, Y. Hirahata, M. Yamagiwa, S. Kajita, M. Takagi, N. Yoshida, R. Yoshihara, T. Tokunaga, M. Tokitani, Influence of crystal orientation on damages of tungsten exposed to helium plasma, J. Nucl. Mater. 438 (2013) S879–S882. doi:10.1016/j.jnucmat.2013.01.190.

[71] C.M. Parish, H. Hijazi, H.M. Meyer, F.W. Meyer, Effect of tungsten crystallographic orientation on He-ion-induced surface morphology changes, Acta Mater. 62 (2014) 173–181. doi:10.1016/j.actamat.2013.09.045.

[72] S.S. Brenner, Growth and Properties of "Whiskers": Further research is needed to show why crystal filaments are many times as strong as large crystals, Science (80-.). 128 (1958) 569–575. doi:10.1126/science.128.3324.569.

[73] J.A. Brusse, G.J. Ewell, J.P. Siplon, Tin Whiskers : Attributes and Mitigation, 2002.

[74] G.T. Galyon, Annotated tin whisker bibliography and anthology, IEEE Trans. Electron. Packag. Manuf. 28 (2005) 94–122. doi:10.1109/TEPM.2005.847440.

[75] J.B. Camp, T.W. Darling, R.E. Brown, Macroscopic variations of surface potentials of conductors, J. Appl. Phys. 69 (1991) 7126. doi:10.1063/1.347601.

[76] M.A. Lieberman, A.J. Lichtenberg, Principles of Plasma Discharges and Materials Processing, 2nd ed., John Wiley & Sons, 2005.

[77] R.A. Pitts, Retarding Field Energy Analysis for Ion Temperature Measurement in the Tokamak Edge, Contrib. to Plasma Phys. 36 (1996) 87–93. doi:10.1002/ctpp.19960360114.

[78] G. Jaffé, On the Currents Carried by Electrons of Uniform Initial Velocity, Phys. Rev. 65 (1944) 91–98. doi:10.1103/PhysRev.65.91.

[79] W. Sakaguchi, S. Kajita, N. Ohno, M. Takagi, H. Kurishita, Formation Condition of Fiberform Nanostructured Tungsten by Helium Plasma Exposure, Plasma Fusion Res. 5 (2010) S1023–S1023. doi:10.1585/pfr.5.S1023.

[80] K.B. Woller, D.G. Whyte, G.M. Wright, In situ elastic recoil detection analysis of tungsten surfaces during ITER-like helium irradiation, in: 2015 IEEE 26th Symp. Fusion Eng., IEEE, Austin, Texas, 2015: pp. 1–6. doi:10.1109/SOFE.2015.7482349.

[81] K.B. Woller, D.G. Whyte, G.M. Wright, Bimodal ion energy distributions in helicon wave-coupled helium plasma, Submitt. Publ. (2017).

[82] F.F. Chen, Helicon discharges and sources: a review, Plasma Sources Sci. Technol. 24 (2015) 14001. doi:10.1088/0963-0252/24/1/014001.

[83] J.-H. Kim, H.-Y. Chang, A study on ion energy distribution functions and plasma potentials in helicon wave plasmas, Phys. Plasmas. 3 (1996) 1462. doi:10.1063/1.871737.

[84] A. Perry, G. Conway, R. Boswell, H. Persing, Modulated plasma potentials and cross field diffusion in a Helicon plasma, Phys. Plasmas. 9 (2002) 3171. doi:10.1063/1.1483845.

[85] M. Wiebold, Y.T. Sung, J.E. Scharer, Ion acceleration in a helicon source due to the self-bias effect, Phys. Plasmas. 19 (2012) 1–11. doi:10.1063/1.4714605.

[86] V. Kaeppelin, M. Carrère, J.B. Faure, Different operational regimes in a helicon plasma source, Rev. Sci. Instrum. 72 (2001) 4377–4382. doi:10.1063/1.1419228.

[87] K.B. Woller, D.G. Whyte, G.M. Wright, Isolated nano-tendril bundles on tungsten surfaces exposed to radiofrequency helium plasma, Submitt. to Nucl. Mater. Energy. (2016).

[88] J.F. Caneses, B. Blackwell, RF compensation of double Langmuir probes: modelling and experiment, Plasma Sources Sci. Technol. 24 (2015) 35024. doi:10.1088/0963-0252/24/3/035024.

[89] E.O. Johnson, L. Malter, A floating double probe method for measurements in gas discharges, Phys.

Rev. 80 (1950) 58–68. doi:10.1103/PhysRev.80.58.

[90] J.-S. Chang, J.G. Laframboise, Double-probe theory for a continuum low-density plasma, J. Phys. D. Appl. Phys. 9 (1976) 1699–1703. doi:10.1088/0022-3727/9/12/008.

[91] E.V. Heubel, L.F. Velasquez-Garcia, Microfabricated Retarding Potential Analyzers With Enforced Aperture Alignment for Improved Ion Energy Measurements in Plasmas, J. Microelectromechanical Syst. 24 (2015) 1355–1369. doi:10.1109/JMEMS.2015.2399373.

[92] C. Böhm, J. Perrin, Retarding-field analyzer for measurements of ion energy distributions and secondary electron emission coefficients in low-pressure radio frequency discharges, Rev. Sci. Instrum. 64 (1993) 31–44. doi:10.1063/1.1144398.

[93] E.Y. Wang, N. Hershkowitz, T. Intrator, C. Forest, Techniques for using emitting probes for potential measurement in rf plasmas, Rev. Sci. Instrum. 57 (1986) 2425–2431. doi:10.1063/1.1139088.

[94] C.M. Franck, O. Grulke, A. Stark, T. Klinger, E.E. Scime, G. Bonhomme, Measurements of spatial structures of different discharge modes in a helicon source, Plasma Sources Sci. Technol. 14 (2005) 226–235. doi:10.1088/0963-0252/14/2/003.

[95] B.N. Breizman, A. V. Arefiev, Radially Localized Helicon Modes in Nonuniform Plasma, Phys. Rev. Lett. 84 (2000) 3863–3866. doi:10.1103/PhysRevLett.84.3863.

[96] A. V. Arefiev, B.N. Breizman, Theoretical components of the VASIMR plasma propulsion concept, Phys. Plasmas. 11 (2004) 2942–2949. doi:10.1063/1.1666328.

[97] G. Chen, A. V. Arefiev, R.D. Bengtson, B.N. Breizman, C.A. Lee, L.L. Raja, Resonant power absorption in helicon plasma sources, Phys. Plasmas. 13 (2006) 123507. doi:10.1063/1.2402913.

[98] C.A. Lee, G. Chen, A. V. Arefiev, R.D. Bengtson, B.N. Breizman, Measurements and modeling of radio frequency field structures in a helicon plasma, Phys. Plasmas. 18 (2011) 13501. doi:10.1063/1.3533273.

[99] M.A. Lieberman, A.J. Lichtenberg, Principles of Plasma Discharges and Materials Processing, John Wiley & Sons, Inc., Hoboken, NJ, USA, 2005. doi:10.1002/0471724254.

[100] J.D. Huba, NRL Plasma Formulary, Washington, DC, 2004.

[101] F.F. Chen, I.D. Sudit, M. Light, Downstream physics of the helicon discharge, Plasma Sources Sci. Technol. 6 (1996) 173–180.

[102] J.F. Caneses, B.D. Blackwell, Collisional damping of helicon waves in a high density hydrogen linear plasma device, Plasma Sources Sci. Technol. 25 (2016) 55027. doi:10.1088/0963-0252/25/5/055027.

[103] P. Fiflis, D. Curreli, D.N. Ruzic, Direct time-resolved observation of tungsten nanostructured growth due to helium plasma exposure, Nucl. Fusion. 55 (2015) 33020–7. doi:10.1088/0029-5515/55/3/033020.

[104] A. Khan, G. De Temmerman, T.W. Morgan, M.B. Ward, Effect of rhenium addition on tungsten fuzz formation in helium plasmas, J. Nucl. Mater. 474 (2016) 99–104. doi:10.1016/j.jnucmat.2016.03.016.

[105] M.H.J. 't Hoen, M. Balden, A. Manhard, M. Mayer, S. Elgeti, A.W. Kleyn, P. a. Zeijlmans van Emmichoven, Surface morphology and deuterium retention of tungsten after low- and high-flux deuterium plasma exposure, Nucl. Fusion. 54 (2014) 83014. doi:10.1088/0029-5515/54/8/083014.

[106] G.M. Wright, G.G. Van Eden, L.A. Kesler, G. De Temmerman, D.G. Whyte, K.B. Woller, Characterizing the recovery of a solid surface after tungsten nano-tendril formation, J. Nucl. Mater. 463 (2015). doi:10.1016/j.jnucmat.2014.11.083.

[107] R.P. Doerner, S.I. Krasheninnikov, K. Schmid, Particle-induced erosion of materials at elevated temperature, J. Appl. Phys. 95 (2004) 4471–4475. doi:10.1063/1.1687038.

[108] P. Wynblatt, N.A. Gjostein, A calculation of migration energies and binding energies for tungsten adatoms on tungsten surfaces, Surf. Sci. 22 (1970) 125–136. doi:10.1016/0039-6028(70)90028-2.

[109] W.R. Graham, G. Ehrlich, Surface self-diffusion of single atoms, Thin Solid Films. 25 (1975) 85–96. doi:10.1016/0040-6090(75)90249-7.

[110] G.L. Kellogg, Field ion microscope studies of single-atom surface diffusion and cluster nucleation on metal surfaces, Surf. Sci. Rep. 21 (1994) 1–88. doi:10.1016/0167-5729(94)90007-8.

[111] R.M. Bradley, J.M.E. Harper, Theory of ripple topography induced by ion bombardment, J. Vac. Sci. Technol. A Vacuum, Surfaces, Film. 6 (1988) 2390–2395. doi:10.1116/1.575561.

[112] W.W. Mullins, Flattening of a Nearly Plane Solid Surface due to Capillarity, J. Appl. Phys. 30 (1959) 77–83. doi:10.1063/1.1734979.

[113] U. Valbusa, C. Boragno, F.B. De Mongeot, Nanostructuring surfaces by ion sputtering, J. Phys. Condens. Matter. 14 (2002) 8153–8175. doi:10.1088/0953-8984/14/35/301.

[114] H.-C. Jeong, E.D. Williams, Steps on surfaces: experiment and theory, Surf. Sci. Rep. 34 (1999) 171–294. doi:10.1016/S0167-5729(98)00010-7.

[115] M. Miyamoto, T. Watanabe, H. Nagashima, D. Nishijima, R.P. Doerner, S.I. Krasheninnikov, A. Sagara, N. Yoshida, In situ transmission electron microscope observation of the formation of fuzzy structures on tungsten, Phys. Scr. T159 (2014) 14028. doi:10.1088/0031-8949/2014/T159/014028.

[116] C.M. Parish, K. Wang, R.P. Doerner, M.J. Baldwin, Grain orientations and grain boundaries in tungsten nonotendril fuzz grown under divertor-like conditions, Scr. Mater. 127 (2017) 132–135. doi:10.1016/j.scriptamat.2016.09.018.

[117] M.A. Makeev, R. Cuerno, A.-L. Barabási, Morphology of ion-sputtered surfaces, Nucl. Instruments Methods Phys. Res. Sect. B Beam Interact. with Mater. Atoms. 197 (2002) 185–227. doi:10.1016/S0168-583X(02)01436-2.

[118] G. Costantini, S. Rusponi, F.B. De Mongeot, C. Boragno, U. Valbusa, Periodic structures induced by normal-incidence sputtering on Ag (110) and Ag (001): flux and temperature dependence, J. Phys. Condens. Matter. 13 (2001) 5875. doi:10.1088/0953-8984/13/26/303.

[119] P. Politi, G. Grenet, A. Marty, A. Ponchet, J. Villain, Instabilities in crystal growth by atomic or molecular beams, Phys. Rep. 324 (2000) 271–404. doi:10.1016/S0370-1573(99)00046-0.

[120] C.S. Madi, E. Anzenberg, K.F. Ludwig, M.J. Aziz, Mass redistribution causes the structural richness of ion-irradiated surfaces, Phys. Rev. Lett. 106 (2011) 1–4. doi:10.1103/PhysRevLett.106.066101.

[121] Z. Di, X.M. Bai, Q. Wei, J. Won, R.G. Hoagland, Y. Wang, A. Misra, B.P. Uberuaga, M. Nastasi, Tunable helium bubble superlattice ordered by screw dislocation network, Phys. Rev. B - Condens. Matter Mater. Phys. 84 (2011) 1–5. doi:10.1103/PhysRevB.84.052101.

[122] K.D. Hammond, B.D. Wirth, Crystal orientation effects on helium ion depth distributions and adatom formation processes in plasma-facing tungsten, J. Appl. Phys. 116 (2014) 143301. doi:10.1063/1.4897419.

[123] G. Ehrlich, F.G. Hudda, Atomic View of Surface Self-Diffusion: Tungsten on Tungsten, J. Chem. Phys. 44 (1966) 1039–1049. doi:10.1063/1.1726787.

[124] R. Ditchfield, E.G. Seebauer, Semiconductor surface diffusion: Effects of low-energy ion bombardment, Phys. Rev. B - Condens. Matter Mater. Phys. 63 (2001) 1253171–1253179. doi:10.1103/PhysRevB.63.125317.

[125] K.B. Woller, D.G. Whyte, G.M. Wright, Impact of Helium Ion Energy Modulation on Tungsten Surface Morphology and Nano-Tendril Growth, Submitt. to Nucl. Fusion. (2016).

[126] C.H. Wu, Chemical sputtering of graphite and tungsten by oxygen, J. Nucl. Mater. 145–147 (1987) 448–452. doi:10.1016/0022-3115(87)90379-5.

[127] E. Hechtl, W. Eckstein, J. Roth, J. Laszlo, Sputtering of tungsten by oxygen at temperatures up to 1900 K, J. Nucl. Mater. 179–181 (1991) 290–293. doi:10.1016/0022-3115(91)90083-J.

[128] D. Nishijima, M.J. Baldwin, R.P. Doerner, J.H. Yu, Sputtering properties of tungsten "fuzzy" surfaces, J. Nucl. Mater. 415 (2011) S96–S99. doi:10.1016/j.jnucmat.2010.12.017.

[129] T. Michely, C. Teichert, Adatom yields, sputtering yields, and damage patterns of single-ion impacts on Pt(111), Phys. Rev. B. 50 (1994) 11156–11166. doi:10.1103/PhysRevB.50.11156.

[130] F.W. Meyer, H. Hijazi, M.E. Bannister, K.A. Unocic, L.M. Garrison, C.M. Parish, Flux threshold measurements of He-ion beam induced nanofuzz formation on hot tungsten surfaces, Phys. Scr. T167 (2016) 14019. doi:10.1088/0031-8949/T167/1/014019.

[131] T.J. Petty, A. Khan, T. Heil, J.W. Bradley, Fuzzy tungsten in a magnetron sputtering device, J. Nucl. Mater. 480 (2016) 374–385. doi:10.1016/j.jnucmat.2016.08.019.

[132] R.K. Janev, W.D. Langer, D.E. Post, Jr., K. Evans, Jr., Elementary processes in hydrogen-helium plasmas: cross sections and reaction rate coefficients, Springer-Verlag, Berlin, Germany, 1987.

[133] J. Amano, D.N. Seidman, Diffusivity of 3He atoms in perfect tungsten crystals, J. Appl. Phys. 56 (1984) 983. doi:10.1063/1.334039.

[134] Y.L. Zhou, J. Wang, Q. Hou, A.H. Deng, Molecular dynamics simulations of the diffusion and coalescence of helium in tungsten, J. Nucl. Mater. 446 (2014) 49–55. doi:10.1016/j.jnucmat.2013.11.034.

[135] S. Sharafat, A. Takahashi, K. Nagasawa, N. Ghoniem, A description of stress driven bubble growth of helium implanted tungsten, J. Nucl. Mater. 389 (2009) 203–212. doi:10.1016/j.jnucmat.2009.02.027.